

**Non-equilibrium dynamics of di-platinum complexes and molecular dyes in solution:
Insights from transient absorption and two-dimensional Fourier transform spectroscopy**

Thèse N° 9506

Présentée le 21 mai 2019

à la Faculté des sciences de base
Laboratoire de spectroscopie ultrarapide
Programme doctoral en physique

pour l'obtention du grade de Docteur ès Sciences

par

Lars-Hendrik MEWES

Acceptée sur proposition du jury

Prof. F. Courbin, président du jury
Prof. M. Chergui, directeur de thèse
Prof. J. Hauer, rapporteur
Prof. D. Zigmantas, rapporteur
Prof. C. Bostedt, rapporteur

2019

Abstract

Unraveling the interplay between electronic- and vibrational degrees of freedom on the earliest time scales of physical, chemical and biological processes is crucial to gaining insight into the mechanisms that govern the world around us, since it is during these primary steps that the fate of the excitation energy – be it solar, chemical or physical – is decided. A tiny structural change during the first 10s of femtoseconds can for example predetermine the dynamics of a system over microseconds, and newly developed techniques in time-domain spectroscopy have proved to successfully capture exactly these pivotal mechanisms.

In this thesis I use ultrafast spectroscopy to investigate the non-equilibrium dynamics of a prototypical di-platinum complex. Transient absorption spectroscopy is complemented with transient absorption anisotropy and fluorescence up-conversion to identify the spectral features of the intermediate excited states. The results show that the intersystem crossing from the singlet- to the triplet manifold of states happens on a 0.6 to 0.9 picosecond time scale, slower than previously assumed. As a consequence, the observable coherence is associated with a singlet excited state, rather than a triplet, and dephases prior to the intersystem crossing. The study further illustrates the importance of having a good understanding of the transient spectral signatures and yields insight into the structural dynamics of di-platinum complexes.

In addition, I have built and commissioned a two-dimensional photon echo experiment that is capable of acquiring broadband excitation- and detection frequency resolved transient spectra in the visible with a temporal resolution of approx. 10 femtoseconds. All relevant steps of the development are outlined in this thesis and 2D spectra of four different dye solutions highlight the capabilities of the experiment. The temporal evolution of the 2D spectra of Nile blue is analyzed as an example and shows the information content that is contained within the data.

Keywords: coherent ultrafast spectroscopy, multi-dimensional spectroscopy, transient absorption, transient absorption anisotropy, fluorescence up-conversion, structural dynamics, vibrational coherence, non-equilibrium dynamics

Zusammenfassung

Das Entschlüsseln des Zusammenspiels von elektronischen- und vibrationellen Freiheitsgraden auf den frühesten Zeitskalen von physikalischen, chemischen und biologischen Prozessen ist entscheidend, um Einblick in die Mechanismen zu bekommen, die die Welt um uns herum bestimmen, da sich während dieser primären Schritte das Schicksal der Anregungsenergie – sei sie solar, chemisch oder physikalisch – entscheidet.

In dieser These verwende ich ultraschnelle Spektroskopie, um die Nicht-Gleichgewichtsdynamik eines prototypischen di-Platin Komplexes zu untersuchen. Transiente Absorptionsspektroskopie wird komplementiert durch transiente Absorptionsanisotropie und Fluoreszenz Aufwärtskonversion, um die spektralen Merkmale der intermediären, angeregten Zustände zu identifizieren. Die Ergebnisse zeigen, dass die Interkombination aus den Singlet- in die Triplet-Zustände auf einer 0.6 bis 0.9 Pikosekunden Zeitskala stattfindet, langsamer als bisher angenommen. Als Konsequenz sind die zu beobachtenden Kohärenzen nicht mit einem Singlet-, sondern mit einem Triplet-Zustand zu assoziieren, und dephasieren vor der Interkombination. Die Studie illustriert außerdem die Wichtigkeit eines guten Verständnisses der transienten, spektralen Signaturen und gibt Einblick in die strukturellen Dynamiken von di-Platin Komplexen.

Darüber hinaus habe ich ein zweidimensionales Photon Echo experiment gebaut und in Betrieb genommen, welches es ermöglicht Anregungs- und Abfragefrequenz aufgelöste transiente Spektren im sichtbaren mit einer Zeitaufösungen von ca. 10 Femtosekunden aufzunehmen. Alle relevanten Schritte der Entwicklung sind in dieser These beschrieben und 2D Spektren vier verschiedener Farbstofflösungen betonen das Potenzial des Experiments. Die zeitliche Entwicklung der 2D Spektren von Nilblau wird beispielhaft analysiert und zeigt den Informationsgehalt, der in den Daten enthalten ist.

Schlagwörter: kohärente ultraschnelle Spektroskopie, Multidimensionale Spektroskopie, Transiente Absorption, Transiente Absorptionsanisotropie, Fluoreszenz Aufwärtskonversion, Strukturelle Dynamiken, Vibrationelle Kohärenzen, Nicht-Gleichgewichtsdynamik

Contents

Abstract (English/Deutsch)	iii
Table of contents	vii
List of figures	xi
List of tables	xix
List of abbrev.	xxi
1 Introduction to time-resolved spectroscopy	1
2 Concepts in ultrafast spectroscopy	5
2.1 Mathematical description of a propagating laser pulse	5
2.2 Measurement of femtosecond laser pulses	8
2.3 Theory of light-matter interaction	11
2.3.1 A quick quantum mechanics primer	12
2.3.2 Time-dependence of a quantum mechanical superposition	14
2.3.3 The density matrix of an ensemble and its expectation value	16
2.3.4 Time evolution of the ensemble density matrix	19
2.3.5 Response functions and their representation using vertical Feynman diagrams	23
2.3.6 Time-ordering and the rotating wave approximation	25
2.3.7 Rephasing and non-rephasing response functions	26
2.3.8 The Liouville representation	28
2.3.9 Treatment of dephasing: Kubo's theory and the Brownian oscillator	29
2.3.10 Examples: Absorption and fluorescence	31
2.4 Transient absorption spectroscopy	33
2.4.1 Observable transient signals in the visible	33
2.4.2 Relaxation channels	34
2.4.3 Anisotropy and molecular structure	35
2.5 Coherent multidimensional spectroscopy	36

vii

Contents

2.5.1	Microscopic picture of two-dimensional photon echo spectroscopy . . .	37
2.5.2	The projection-slice theorem	39
2.5.3	Wavepackets and their description using response functions	39
2.5.4	Signals and information in 2D spectroscopy	41
2.5.5	Kinetics and relaxation pathways	41
2.5.6	Coherences and wavepackets	44
3	Methods in transient absorption spectroscopy	47
3.1	Overview of the transient absorption setup	47
3.1.1	Excitation pulse generation	48
3.1.2	Prism compressor	50
3.1.3	White light generation via self-phase modulation in CaF ₂	51
3.1.4	Pump-probe measurements and data acquisition	52
3.1.5	Magic angle and anisotropy measurements	52
4	Development and characterization of the 2D photon echo setup	55
4.1	Overview of the 2D photon echo setup	55
4.2	White light generation using hollow-core fibers	56
4.3	Chirped mirror compressor	57
4.4	The noncollinear photon echo interferometer	59
4.5	Measuring in a rotating reference frame	62
4.6	Data acquisition – Experimental procedure	62
4.6.1	Acquisition of raw data	62
4.6.2	Background subtraction	63
4.6.3	Coherence time scan	63
4.7	Spectral and temporal calibration	64
4.8	Data treatment	67
4.8.1	From raw data to 2D spectra	67
4.8.2	Phasing	69
4.8.3	Analysis of dynamics and coherences	70
4.9	Exemplary 2D spectra of dye molecules in solution	70
4.10	Experimental outlook	72
5	Transient spectroscopy of [Pt(ppy)(μ-tBu₂pz)]₂	75
5.1	Background	75
5.2	Short excursion: Coherences in time-domain spectroscopy	77
5.3	Sample preparation and characterization	79
5.4	Experimental details	80
5.4.1	Transient absorption	80
5.4.2	Fluorescence up-conversion	81

5.5	Results	82
5.5.1	Magic angle transient absorption	82
5.5.2	Transient absorption anisotropy	87
5.5.3	Transient fluorescence up-conversion	90
5.6	Discussion	92
5.7	Summary and outlook	94
5.8	Supplementary information	95
6	Multidimensional electronic spectroscopy of Nile blue	101
6.1	Background	101
6.2	Coherences in the ground- and excited state measured in the time-domain . . .	103
6.3	Sample characterization and photophysics	104
6.4	Experimental methods	106
6.5	Results	107
6.6	Phasing, benchmarking and comparison to the literature	111
6.7	Preliminary discussion	113
6.8	Outlook	114
7	Conclusion and outlook	115
A	Software	117
	Bibliography	119
	Curriculum Vitae	135

List of Figures

1.1	(left) Stills from the <i>falling cat</i> short film produced by Étienne-Jules Marey and his assistant Georges Demenÿ in 1894. (right) Overlay of the 1969 model of Kane and Scher onto the photograph of a falling cat (Ralph Crane – <i>Life</i> magazine). Reprinted from ref. [1], copyright 1969, with permission from Elsevier.	2
1.2	The development of ultrashort laser pulses can be summarized by the evolution of the shortest laser pulse. Reprinted from ref. [7], copyright 1969, with permission from Springer Nature.	3
1.3	Fundamental processes within and between molecules occur over a wide range of time-scales, from femtosecond to microseconds. Reprinted from ref. [11]. . .	4
2.1	Effects of group delay, group delay dispersion, and third order dispersion on a femtosecond laser pulse. After ref. [12].	6
2.2	Example FROG spectrograms: e) up-chirped pulse with GDD $\phi'' = 200\text{fs}^2$ and TOD of $\phi''' = 1000\text{fs}^3$. j) Sine modulated pulse at central frequency ω_0 with $\phi(\omega) = 1 \sin[30\text{fs}(\omega - \omega_0)]$. Insets show the envelope of the time-dependent electric field. Reprinted from ref. [15], copyright 2007, with permission from Springer Nature.	10
2.3	Pictorial explanation of the density matrix for a pure state (left) in which all systems are in a superposition state and a maximally mixed state (right) in which half of the sub-systems are in the ground- and half in the excited state. N_i are the number of systems in state i	18
2.4	Rules for writing and reading double-sided vertical Feynman diagrams. The notation $\mu(t_n + t_{n-1} + \dots + t_1)$ has been abbreviated as μ_n	24
2.5	(left) An alternative way to describe the excited state absorption Liouville-space pathway is the ladder diagram. Interactions with the bra (ket) of the density matrix are drawn as dashed (solid) arrows and the final emission as a wiggly arrow. Time runs from left to right. (right) The corresponding vertical Feynman diagram.	25

List of Figures

- 2.6 Vertical Feynman diagrams illustrating the rotating wave approximation. The expressions below each diagram show that for the right Liouville-space pathway, the argument of the integral oscillates with 2ω 26
- 2.7 Example of (left) a rephasing and (right) a non-rephasing Liouville-space pathway. 27
- 2.8 Comparison between the (left) rephasing, (middle) non-rephasing, and (right) absorptive 2D spectrum, which is the addition of the R and NR spectra. Improper weighing off either R or NR component leads to 'phase twists' in the absorptive 2D spectrum. 27
- 2.9 (left) Ladder diagram and (middle) double sided Feynman diagram describing the response function of light absorption in a two-level system. (right) The macroscopic polarization generates a signal field that is phase shifted w.r.t. the exciting field and their destructive interference, as seen by an observer behind the sample, is interpreted as the absorption of light. 32
- 2.10 Feynman diagram for fluorescence. 33
- 2.11 (left) Jablonski diagram showing the different signal- (colors) and relaxation (gray) channels in a pump-probe experiment. Straight arrows indicate radiative-, wiggly arrows non-radiative processes. (right) Exemplary transient spectrum illustrating the signals. 33
- 2.12 (black) Pulse scheme of a photon echo experiment with (red) the projection of the Bloch vector onto the real axis as visualization of the density matrix. The 2×2 matrices indicate which element of the density matrix is relevant for the evolution of the density matrix during the time intervals τ , T, and t. 37
- 2.13 (left) The displaced oscillator model. (middle) Ladder- and (right) Feynman diagram description of a vibrational coherence on the excited electronic state during the population time. In this example, the detection frequency is greater than the excitation frequency by one quantum of the vibrational mode, leading to an off-diagonal signal in the 2D spectrum. 40
- 2.14 (top) Spectral diffusion, described here by the effect of the solvent dipole orientation on the frequency of the solute dipole, leads to the loss of correlation between excitation- and detection frequency, resulting in a (bottom) broadening of the 2D lineshape along the anti-diagonal direction with increasing population time. 42
- 2.15 Chemical exchange, structural transformations, or population transfer between chromophores is observed via the formation of cross-peaks in 2D spectra. . . . 43

2.16 (top) Illustrative 2D spectrum of a displaced oscillator showing a characteristic pattern of GSB and SE features. ESA to a higher lying electronic state appears as a negative signal at $\omega_t > 16750 \text{ cm}^{-1}$. (bottom) Double sided Feynman diagrams for a 3-level system. In a TA experiment the first two (\mathbf{k}_1 and \mathbf{k}_2) light-matter interactions occur within the same laser pulse and the observed signal corresponds to the integration of the 2D spectrum over the frequency range $\Delta\omega_\tau$, which corresponds to the spectral width of the excitation pulse. The dependence of the photon echo on the temporal delay between \mathbf{k}_1 and \mathbf{k}_2 is exploited in 2D spectroscopy to resolve the excitation dependence of the transient signal.	44
2.17 Overview of the R and NR 2D beating patterns observed for (top row) a displaced oscillator and (bottom row) an electronic dimer. Reprinted from ref. [63], copyright 2012, with permission from Elsevier. Grey boxes have been added for the purpose of this thesis to illustrate the different model systems.	45
3.1 Overview of the 1 kHz setup.	48
3.2 Schematic overview of the NOPA and folded prism compressor.	49
3.3 (a) The (projected) group velocities of the idler and signal are matched in the noncollinear geometry. After refs. [77] and [79]. (b) Internal angles between signal, idler, and pump for noncollinear phase matching. o.a. is the optic axis of the nonlinear crystal.	49
3.4 Working principle of a prism compressor. The up-chirped input pulse experiences negative GVD, due to angular dispersion. Passing through four prisms in a folded geometry removes additional spatio-temporal distortions that have been introduced by the first prism.	50
3.5 White light spectrum generated via self-phase modulation inside CaF_2	51
3.6 Comparison between the measured and calculated transient MA spectrum of $[\text{Pt}(\text{ppy})(\mu\text{-tBu}_2\text{pz})_2]_2$. The calculated spectrum is rescaled to account for the difference in pulse energy between the measurements, but its spectral shape agrees well with the measured transient MA spectrum. The pump wavelength region is excluded due to scatter.	53
4.1 Schematic overview of the 2D experiment.	56
4.2 White light spectra from SPM inside an argon-filled HCF and Fourier transforms of the spectra (insets) on different days and under different experimental conditions.	57

List of Figures

- 4.3 (a) A dielectric quarter-wave Bragg mirror can be used as a highly reflective element. (b) If the Bragg wavelength is increased with each layer, longer wavelength penetrate deeper into the substrate, leading negative GDD. (c) Oscillations of the GDD can be reduced by impedance-matching and anti-reflection coating of the mirror. Reprinted, with permission, from ref. [95], copyright 1998 IEEE. 58
- 4.4 Spectrogram of the broadband laser pulse measured by transient grating FROG. The top and left panels show the integration onto the wavelength and time axis, respectively. 59
- 4.5 (a) Drawing of the BOXCARS geometry showing the propagation direction of $\mathbf{k}_1 - \mathbf{k}_{LO}$. The vector diagrams show the projections of the \mathbf{k} -vectors on (b) a horizontal plane along z and (c) onto the x - y plane, where z is the direction normal to the square of the four beams. t_{LO} is introduced by passing $\mathbf{k}_1 - \mathbf{k}_3$ through 1 mm of fused silica (not shown). 60
- 4.6 Design of the interferometer. (a) The beam is split into $\mathbf{k}_1 / \mathbf{k}_2$ and $\mathbf{k}_3 / \mathbf{k}_{LO}$. DS1: delay stage 1, BS: beam splitter, CP: compensation plate. (b) The beams from (a) are split analogously into $\mathbf{k}_1 - \mathbf{k}_{LO}$. DS2: delay stage 2. 61
- 4.7 Four shot background subtraction scheme. 63
- 4.8 Simplified illustration of the coherence time scan routine. Red arrows describe to temporal delay of DS2, blue arrows the temporal delay of DS1. Open- and closed arrowheads indicate the shift to positive- and negative time, respectively, and the convention is identical to Figure 4.6. Note that in the bottom diagram the red and blue arrows of \mathbf{k}_2 cancel each other, leading to a constant population time delay. 64
- 4.9 (top) Reference neon spectrum (red) superimposed on the measured neon spectrum (blue). The region around 550 nm is amplified to observe the weak spectral features. The FWHM of the fitted peaks is shown above to assess the spectral resolution. The data point marked with an asterisk is too large, due to the small amplitude of the emission peak. (bottom) Quadratic and cubic fit of the peak positions and residuals (top panel). 66
- 4.10 Overview of the data treatment for terylene diimide. (top left) Fourier filtered data set showing the interference between the signal and the LO for varying coherence times. (top right) Inverse Fourier transform ($\omega_t \rightarrow t$) of the raw data. (bottom left) $I(\tau, T, \omega_t)$ after subtraction of a linear phase term that is due to the LO delay. The line plots show the TA spectrum (black, solid) and LO spectrum (blue, dashed) for comparison. (bottom right) Absolute value 2D spectrum after the final Fourier transform $\tau \rightarrow \omega_\tau$. Note the different axes and the fact that the 2D spectrum is rotated w.r.t. the rest of the spectra in this thesis. Contour lines of the 2D spectrum are at 1,5, 10, 20, . . . , 90 % of the signal maximum. 68

4.11 Exemplary coherences analysis of Nile blue. (top) Time traces at every point of the 2D spectrum are fitted by a Gaussian IRF and exponential decays. The residual of the fit is Fourier transformed to reveal the (middle) coherence frequency spectrum. (bottom) The excitation / detection dependence of each coherence can provide insight into their microscopic origin.	71
4.12 Comparison of the 2D spectra of test dyes. Rows: nb, rh800, tdi, and pin. Columns: absolute- and real (absorptive) 2D spectra. Contour lines are at 1, 4, 8, 12, 16, 20, 30, 40, . . . 100 % of the data set, which is normalized to a global maximum, excluding the data around $T = 0$. The absorption spectrum (red line) and transient absorption spectrum (black line) for each dye is shown for comparison on the x-axis and y-axis, respectively.	73
5.1 (left) Molecular structure of Ptpy showing the cis-isomer and (right) molecular orbital diagram. Electronic interaction between the two halves of the molecule lifts the degeneracy between the orbitals leading to the appearance of the MMLCT transition.	76
5.2 Absorption (red) and emission (blue) spectrum of $[\text{Pt}(\text{ppy})(\mu\text{-tBu}_2\text{pz})_2]$ in toluene and the emission spectrum (light gray) at low solute concentration. The blue dashed line is the emission spectrum measured on a different fluorometer. The shoulder and peaks marked by asterisks are due to Raman scattering of the 500 nm excitation.	80
5.3 Chirp-corrected TA measurement of Ptpy in toluene. (top) The time-wavelength representation reveals oscillations of the signal during the first picosecond. Red and green vertical lines indicate the two distinct frequencies with periods of 245 fs (130 cm^{-1}) at 540 nm and 340 fs (103 cm^{-1}) at 640 nm, respectively. (bottom) The transient spectra suggest the presence of an isosbestic point between 550 nm and 560 nm.	83
5.4 (top) A global fit of the magic angle data (400 to 680 nm, excluding the pump wavelength region) and delay times < 0.15 ps, reveals three decay associated spectra. (bottom) The fit agrees reasonably well with the time traces, as seen by the residuals, however some deviations during the first picosecond and between 10 and 100 ps below 500 nm are observed. The residual at 410 nm has a larger spread around 0 and has been omitted for clarity.	85
5.5 Transient spectra under parallel (top) and perpendicular (bottom) relative polarization of pump and probe pulses at selected time delays. The pump wavelength region has been omitted for clarity and the narrow, positive-going peaks below 450 nm are due to the coherent artifact.	88

List of Figures

- 5.6 (top) Broadband transient anisotropy of Ptpy excited at 500 nm. The pump wavelength region is omitted for clarity. (bottom) Temporal evolution of the anisotropy at selected wavelengths. See text for details. 89
- 5.7 Fluorescence up-conversion signal monochromatically detected between 550 nm and 650 nm in steps of 10 nm under perpendicular polarization conditions. The time constants for the sub-ps decay increase with increasing detection wavelength (Standard error: 20 - 50 fs). A second exponential decay with time constants of a few tens of ps is required for fitting the data, but its amplitude is low. See text for details. 91
- 5.8 Hypothetical microscopic picture of the energy relaxation in Ptpy. 94
- 5.9 (top) Time traces of the transient signal fitted by a sum of three exponential decays and two damped oscillations. The upper panel shows the residuals of the fit. (bottom) Subtracting the > 10 ps kinetic component highlights the oscillations during the first ps. The vertical lines indicate the periods of the two oscillatory functions that are used to fit the data. For details see text. 95
- 5.10 (top) Species associated spectra and (bottom) SVD components of the MA transient of Ptpy in the 500 to 700 nm region. 96
- 5.11 (top) Fluorescence up-conversion data and (bottom) fits of the data with detection wavelength varying from 590 nm to 650 nm in 10 nm steps. The increase in the decay time constant for increasing wavelength is not accompanied by an additional rise of the signal, but by a shift of the respective TA feature. 97
- 5.12 TA response of toluene with parallel, perpendicular, and magic angle relative pump-probe polarization, showing a coherent oscillations with 215 cm^{-1} (Raman mode at 217 cm^{-1} [149]). 99
- 5.13 Linear interpolations in internal coordinates (LIIC) between the S_0/S_1 minimum energy geometries for the cis (left) and trans (right) isomers of Ptpy. The geometries shown represent the initial and final points of each LIIC. The filled circles denote singlet states and the open squares denote triplets. Excited-state energies were calculated at each point on the LIIC at the TDDFT/PBE0 level of theory within the Tamm-Dancoff approximation. For the light elements, a 6-31G(d) basis set was used and a LAN2DZ ECP and basis set on the platinum atoms. 100
- 6.1 Comparison between (a) the displaced oscillator- and (b) the electronic dimer model. The first two bands of the linear absorption spectrum are identical, making it difficult to differentiate between these very different microscopic situations. Reprinted from ref. [63], copyright 2012, with permission from Elsevier.104

6.2	(left) Visible absorption spectrum of nb. The main peak at 626 nm is vibrationally broadened by coupling of the electronic transition to a large number of Raman active modes, which are dominated by modes at 593 cm^{-1} and 1640 cm^{-1} , according to ref. [101]. (right) Resonance structure of nb, showing the delocalization of the positive charge. Depending on the solvent properties, the ground state character will be predominantly one of the two resonance structures [169].	105
6.3	Evolution of the 2D spectrum during the first 200 fs. The absorption- (red line) and TA spectrum (black line) are shown for comparison and the maximum of the signal along ω_τ is shown as yellow dots.	108
6.4	Time traces of $15000\text{ cm}^{-1} / 15850\text{ cm}^{-1}$ spot (blue) and of the integrated signal (red). Oscillations around $T = 0$ are due to pulse overlap and time ordering effects.	109
6.5	(left, blue) Evolution of the maximum of the 2D spectrum in the ω_t dimension and (right, red) of the maximum amplitude.	109
6.6	Beating maps at $\Omega_T = 18\text{ cm}^{-1}$, 575 cm^{-1} , and 594 cm^{-1} . Population time before 20 fs were neglected to avoid artifacts from improper fitting of the IRE. The similarity between the 575 cm^{-1} and 594 cm^{-1} spectra are due to the fact that the 575 cm^{-1} spectrum is in the edge of the 594 cm^{-1} coherence. See Figure 6.7 and text for more details.	110
6.7	(left) Survey beating spectrum from summing $I(\Omega_T)$ over ω_τ and ω_t and (right) coherence frequency spectrum at $15850\text{ cm}^{-1} / 15000\text{ cm}^{-1} (\omega_\tau / \omega_t)$. The beating frequencies of the most prominent coherences are 18 cm^{-1} , 572 cm^{-1} and 596 cm^{-1} , but additional frequencies can be discerned (insets).	111
6.8	Phasing of the complex 2D data shows a tolerable agreement between the integrated 2D spectrum (black line) and the transient spectrum (red, dotted line) at the same population time delay. The LO spectrum (blue, dashed line) is shown for reference.	112
6.9	Comparison of (left) our experimental data with (right) Son et al. [47].	112
6.10	(left) Beating map of the 594 cm^{-1} coherence, derived from an absorptive (R + NR pathway) 2D measurement, with lines (gray, dashed) indicating the 0,1, and 2 vibrational band of the electronic transition. (right) Different regions of the 2D spectrum can be assigned to specific Liouville pathways, and thus transient components, of a displaced oscillator (DO). k_I : rephasing and k_{II} : non-rephasing contribution to the 2D signal. \square : SE, \diamond : GSB; filled symbols: non-oscillating, open symbols: oscillating contribution.	114

List of Tables

2.1	Summary of typical time scales associated with energy relaxation channels. Many of the current problems in physical chemistry deal with relaxation channels that do not obey these time scales.	35
5.1	Summary of extracted time constants.	86
5.2	Results of fitting the single wavelength FIUPS data. The IRF is described by its standard deviation σ and time zero position t_0 . Exponential functions 1 to 3 with amplitude A_n and decay constants τ_n describe the impulse, sub-ps, and few picosecond signal decay, respectively.	98

List of abbrev.

μ -**tBu**₂**pz** 3,5-di-*tert*-butylpyrazolate

abbrev. Abbreviation(s)

2D Two-dimensional

2DPE Two-dimensional photon echo

BOXCARS A background-free experimental geometry for 2DPE

BS Beam splitter

CaF₂ Calcium fluoride

CCD Charge-coupled device (detector)

CLS Center line slope

CM Chirped mirror

CMOS Complementary metal-oxide-semiconductor (detector)

CP Compensation plate

DAS Decay associated spectrum

DO Displaced oscillator

DOF Degree of freedom

DS Delay stage

ED Electronic dimer

ESA Excited state absorption

FC Franck-Condon (point)

FFCF Frequency-frequency correlation function

List of Tables

- FIUPS** Fluorescence up-conversion spectroscopy
- FPGA** field-programmable gate array (integrated circuit)
- FROG** Frequency-resolved optical gating
- fs** Femtoseconds
- FT** Fourier transform
- FWHM** Full width half maximum
- GDD** Group delay dispersion
- GSB** Ground state bleach
- GVD** Group velocity dispersion
- HCF** Hollow core fiber
- IC** Internal conversion
- IRF** Instrument response function
- ISC** Intersystem crossing
- kHz** Kilohertz
- LIIC** Linear interpolation in internal coordinates
- LO** Local oscillator
- MA** Magic angle
- MMLCT** Metal-metal-to-ligand-charge transfer
- nb** Nile blue
- ND** Neutral density
- NOPA** Noncollinear optical parametric amplifier
- nm** Nanometer
- NR** Non-rephasing
- OD** Optical density
- PCM** Polarizable continuum model

PE	Photon echo
PES	Potential energy surface
pin	Pinocyanol iodide
ppy	2-Phenylpyridine
ps	Picoseconds
Pt	Platinum
Ptppy	$[\text{Pt}(\text{ppy})(\mu\text{-tBu}_2\text{pz})]_2$
QM	Quantum mechanics
R	Rephasing
rh800	Rhodamine 800
RWA	Rotating wave approximation
SAS	Species associated spectrum
SE	Stimulated emission
SFG	Sum-frequency generation
SPM	Self-phase modulation
SVD	Singular value decomposition
TA	Transient absorption
TAA	Transient absorption anisotropy
TDDFT	Time-dependent density functional theory
tdi	Terylene diimide
TEM	Transverse electromagnetic (laser mode)
T/R	Transmission-to-reflection ratio
TG	Transient grating
Ti:Sa	Titanium doped sapphire
TOD	Third order dispersion
VR	Vibrational relaxation
w.r.t.	With respect to

1 Introduction to time-resolved spectroscopy

The field of time-resolved spectroscopy has been developed to study non-equilibrium dynamics of a wide range of molecules and solids. In its most general sense, it is the measurement of the change of a system's properties upon some sort of 'excitation event'. This excitation can be any physical or chemical process that changes the properties of the system, such as pH-jumps, temperature-jumps, mixing of educts of a chemical reaction, or light induced reactions. An illustrative example from the macroscopic world is the falling cat movie (Figure 1.1, left) from 1894 by Étienne-Jules Marey, capturing the rotation of a falling cat that has been dropped back first, but still lands on its feet. The problem has attracted considerable attention throughout history, including that of James Clerk Maxwell and George Gabriel Stokes, since cats seem to violate the conservation of angular momentum when falling. Kane and Scher solved the mystery in 1969 [1] by describing the problem as a compound motion of two rigid bodies connected by a common point with zero net angular momentum (Figure 1.1, right).

In time-resolved spectroscopy the frames from Marey's camera – which had the shape of a gun and hence the expression 'to shoot a movie' – is replaced by a spectroscopic observable that yields insight into the microscopic world of atoms, molecules, and solids. These can range from changes in the absorption and refraction of electromagnetic radiation (from terahertz to hard X-rays) to the emission of photoelectrons or molecular fragments as products of an ionization process. A large variety of experimental techniques, based on the principles outlined above, has led to a tremendous understanding of the processes governing the world around us, such as the principles of vision, photosynthesis, and respiration and in addition, it

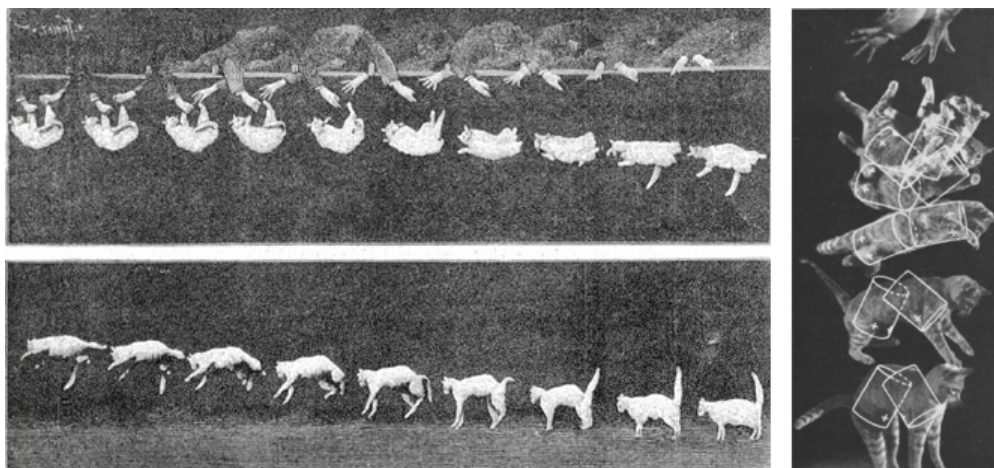


Figure 1.1 – (left) Stills from the *falling cat* short film produced by Étienne-Jules Marey and his assistant Georges Demeny in 1894. (right) Overlay of the 1969 model of Kane and Scher onto the photograph of a falling cat (Ralph Crane – *Life* magazine). Reprinted from ref. [1], copyright 1969, with permission from Elsevier.

has helped in the development of more efficient ways of energy conversion, the treatment of diseases, and the catalysis of chemical reactions, to name only a few. Of utmost importance for all of these achievements was the event of the laser – which had initially been referred to as “a solution looking for a problem” [2] – and the ensuing and ongoing development of pulsed laser sources and nonlinear optical techniques.

A brief history of pulsed lasers and (ultrafast) spectroscopy

The development of ultrafast spectroscopy goes hand in hand with the development of the laser. As a matter of fact, the very first laser was already pulsed, since in 1960 Theodore Maiman used a pulsed light source to pump the gain medium of his Ruby laser [2]. While this cannot be considered the first real pulsed laser source, shortly after, scientist and engineers have started to build pulsed laser sources to exploit their high pulse energies and peak powers. Initially this has been achieved actively by Q-switching, later passively via mode-locking. Figure 1.2 shows the evolution of the shortest pulse duration before 2003. Until 1998 the shortest laser pulses have been generated from dye-lasers, which are still widely used in nanosecond experiments, since most dyes have a large gain bandwidth and their lasing emission can be tuned to different parts of the infrared, visible, or ultraviolet visible spectrum. Since the 1990s titanium doped

sapphire (Ti:Sa) laser have replaced dye lasers when it comes to the generation of ultrashort laser pulses. The achievable pulse duration was shorter than that of the best dye lasers and the gain medium was easier to handle and did not have any associated health risk. Chirped pulse amplification has allowed researchers to generate very high pulse energies and peak powers, which has led to an increase in nonlinear optical techniques to convert between frequencies, generate broadband spectra, and created extreme states of light or matter and has thus been rewarded the 2018 Nobel Prize [3]. It has also driven laser experiments towards the highest frequency- or highest temporal resolution – but the two are inherently connected. Optical frequency comb spectroscopy uses the properties of femtosecond lasers to perform high-precision spectroscopy [4, Nobel Prize] and in turn, the technical advances made in optical frequency comb spectroscopy lead to the generation of attosecond laser pulses [5, 6], which are currently the shortest pulses possible.

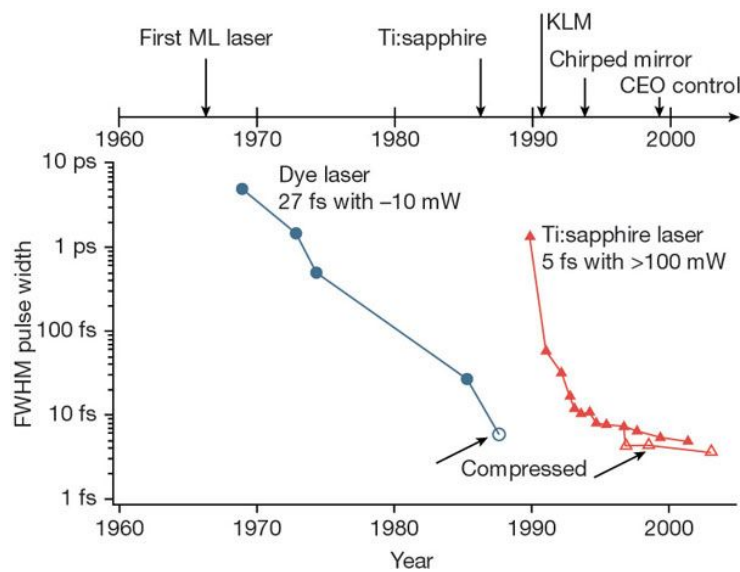


Figure 1.2 – The development of ultrashort laser pulses can be summarized by the evolution of the shortest laser pulse. Reprinted from ref. [7], copyright 1969, with permission from Springer Nature.

The outcome of all technical developments can be found in the current scientific world of spectroscopy, which comprises a large variety of experiments that are based on- and derived from the laser. These vary from high energy laser sources to initiate nuclear reactions, over X-ray free-electron laser, to high resolution spectroscopy and the study of vacuum fluctuations in high stability fiber lasers. This leaves us with one question.

Why do physical chemists need femtosecond laser pulses?

To measure the kinetics of a chemical reaction we need a ‘camera’ with a shutter speed fast enough to capture ‘events’ in the molecular systems in real time. The fastest of these events are intramolecular vibrations, happening on timescales of a few 10s of femtoseconds, while ensuing kinetics range from 100s of femtoseconds to microseconds. Figure 1.3 gives an overview of fundamental processes in molecules (in solution) and their respective time scale. Since electronics can at best achieve nano- and microsecond temporal resolution, femtosecond laser pulses are used to follow kinetics on a sub-ns timescale. The importance of femtosecond spectroscopy in physical chemistry was recognized when Ahmed Zewail was awarded the 1999 Nobel Prize "for his studies of the transition states of chemical reactions using femtosecond spectroscopy" [8]. Some interesting insight into the pre-Nobel Prize ‘Femtoworld’ can be gained from the editorials to the 1998 special issue of “The Third Femtochemistry Conference Symposium” by Castleman [9] and Sundström [10]. In wake of its initial success, time-resolved laser spectroscopy has been applied to answer scientific questions from atoms to proteins assemblies using a large range of the electromagnetic spectrum from terahertz to hard X-rays. In the process, it has led to the development of a large variety of devices and applications – from nanometer-sized optomechanics to kilometer long light sources – to create, manipulate, and detect “pulsed light”.

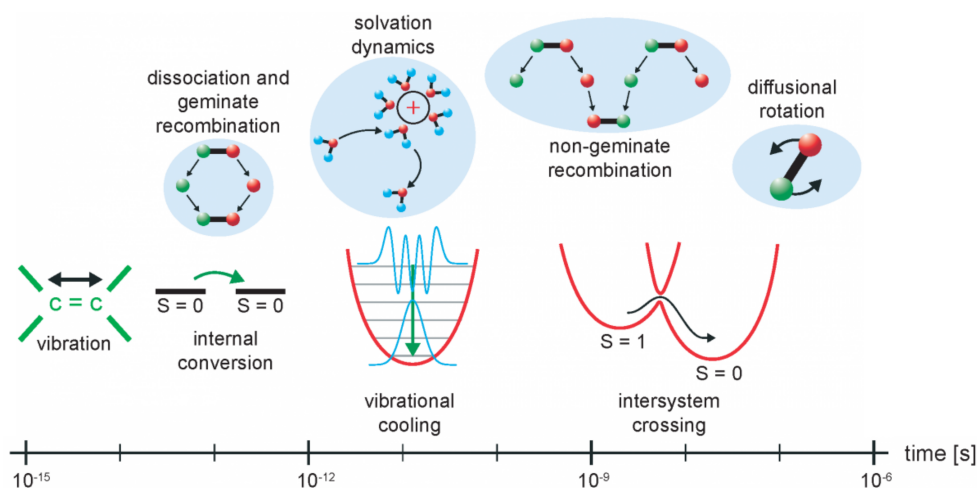


Figure 1.3 – Fundamental processes within and between molecules occur over a wide range of time-scales, from femtosecond to microseconds. Reprinted from ref. [11].

2 Concepts in ultrafast spectroscopy

This chapter will briefly discuss the main aspects of femtosecond laser pulses, as relevant for this thesis, before introducing the response function formalism used to describe light-matter interactions. Thereafter I will outline the theory behind transient absorption and multidimensional spectroscopy, discuss the concept of energy relaxation dynamics and wavepackets in molecular systems, and show how these processes manifest as transient signals.

2.1 Mathematical description of a propagating laser pulse

A laser pulse $E(t)$ can be described in time t as the product of an oscillating electric field with a time-dependent envelope function $A(t)$

$$E(t) = A(t) \cos(\mathbf{k}\mathbf{r} + \omega t + \phi). \quad (2.1)$$

The electric field is described by a wavevector \mathbf{k} , a carrier angular frequency $\omega = 2\pi\nu$ and a phase ϕ . The wavevector is not important for the present description and will be ignored at this point. Fourier transformation links the time-dependent to the frequency-dependent electric field

$$\tilde{E}(\omega) = \mathcal{F}[E(t)] = \int_{-\infty}^{\infty} E(t) e^{-i\omega t} dt \quad (2.2)$$

Chapter 2. Concepts in ultrafast spectroscopy

and vice versa

$$E(t) = \mathcal{F}^{-1}[\tilde{E}(\omega)] = \frac{1}{2\pi} \int_{-\infty}^{\infty} \tilde{E}(\omega) e^{i\omega t} d\omega. \quad (2.3)$$

To describe **propagation and dispersion** effects of laser pulses, the frequency spectrum is commonly decomposed into amplitude and phase spectra

$$\tilde{E}(\omega) = |\tilde{E}(\omega)| e^{-i\phi(\omega)} \quad (2.4)$$

and the phase is expanded in a Taylor-series

$$\phi(\omega) = \phi(\omega_0) + \phi'(\omega_0)(\omega - \omega_0) + \frac{1}{2}\phi''(\omega_0)(\omega - \omega_0)^2 + \frac{1}{6}\phi'''(\omega_0)(\omega - \omega_0)^3 + \dots \quad (2.5)$$

with $\phi' = \left. \frac{d\phi(\omega)}{d\omega} \right|_{\omega_0}$, $\phi'' = \left. \frac{d^2\phi(\omega)}{d\omega^2} \right|_{\omega_0}$ and $\phi''' = \left. \frac{d^3\phi(\omega)}{d\omega^3} \right|_{\omega_0}$. These terms are the group delay, the group delay dispersion (GDD) and the third order dispersion (TOD), respectively. The group delay describes the delay of the peak of the pulse envelope and is defined as the path length over the group velocity L/v_g . Notably, in vacuum the group velocity is identical to the phase velocity $v_g = v_p = c/n$. The GDD is the derivative of the group delay w.r.t. ω and describes the dependence of the group delay on angular frequency. It is associated with an optical

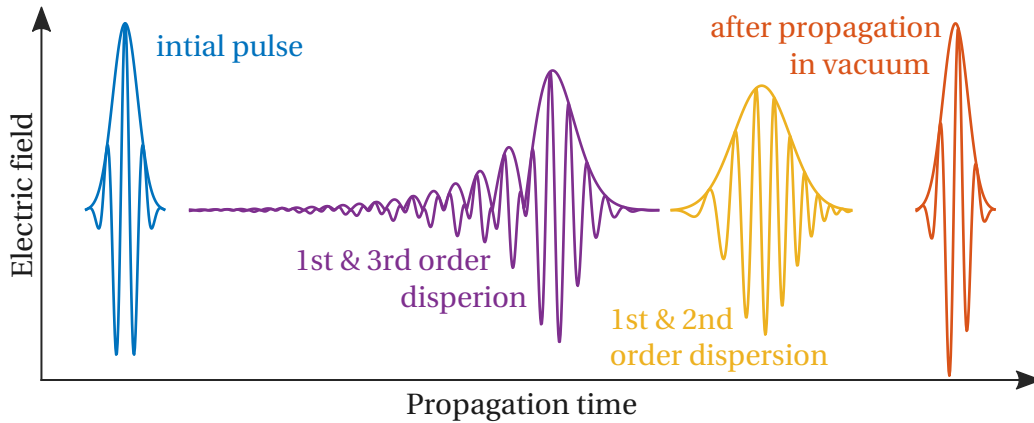


Figure 2.1 – Effects of group delay, group delay dispersion, and third order dispersion on a femtosecond laser pulse. After ref. [12].

element of a specific thickness and its value per unit length is called group velocity dispersion (GVD). The effect of GDD is that different wavelengths inside a material or gas travel at different

2.1. Mathematical description of a propagating laser pulse

speeds, which leads to the spread (compression) of a laser pulse assuming normal (anomalous) dispersion (*vide infra*). TOD refers to the 2nd derivative of the group delay w.r.t. ω and its effect on a laser pulse results in a cubic spectral phase and a complex temporal waveform with one or several post-pulses, due to interference between the high- and low-frequency edges of the pulse, when they are time-coincident. Figure 2.1 exemplifies these effects in the time-domain.

The spectral phase accumulated by a laser pulse when it travels through a material with a frequency-dependent index of refraction $n(\omega)$ is described by the spectral transfer function

$$\phi_m = k(\omega)L = \frac{\omega}{c}n(\omega)L. \quad (2.6)$$

Here, $k(\omega)$ is the frequency-dependent wavevector, L is the distance traveled inside the material and c is the speed of light. With this expression for the phase, the group delay inside the material becomes

$$\phi'_m = \frac{d\phi_m}{d\omega} = \frac{L}{c} \left(n + \omega \frac{dn}{d\omega} \right) = \frac{L}{c} \left(n - \lambda \frac{dn}{d\lambda} \right), \quad (2.7)$$

where, in the last step, we simply changed from radial frequency ω to wavelength λ . The corresponding equation for the GDD reads

$$\phi''_m = \frac{L}{c} \left(2 \frac{dn}{d\omega} + \omega \frac{d^2n}{d\omega^2} \right) = \frac{\lambda^3 L}{2\pi c^2} \frac{d^2n}{d\lambda^2}. \quad (2.8)$$

The latter (and especially its sign) will be important when discussing the prism compressor. The TOD can be derived analogously and $n(\lambda)$ can be calculated from the Sellmeier equation. For normal dispersion, i.e. when $n(\lambda)$ is **upwards** concave, red colors travel faster than blue and a pulse in which red colors arrive before the blue is dubbed **up**-chirped. Anomalous dispersion signifies that $n(\lambda)$ is **downwards** concave and blue colors travel faster than red. Analogously, if the blue colors precede the red, the pulse is called **down**-chirped. Differently speaking, the frequencies within the pulse are increasing or decreasing with time, respectively.

Laser pulses can be conveniently compressed or even shaped (not discussed) by acting on them in the frequency domain, since the temporal evolution of the laser pulse directly depends on the spectral phase, which is typically done using prism- and grating compressors.

Recently, dielectric chirped mirrors (CMs) have been developed that act on the spectral phase via control of the GDD during a reflection of a laser pulse, which circumvents the need to spectrally disperse the light. In addition, CMs can be specially designed to compensate higher order chirp, making them an easy alternative to pulse shaper-based compression methods, which would otherwise be required. The prism- and CM compressor will be discussed in Sections 3.1.2 and 4.3, respectively.

As a result of the Fourier transform relation (Equations (2.2) and (2.3)) between temporal waveform and frequency spectrum, any laser pulse fulfills the **time-bandwidth uncertainty** relation $\Delta t \Delta \omega \geq 4 \ln 2$ and if $\Delta t \Delta \omega = 4 \ln 2$ a pulse is said to be *Fourier transform-*, or *bandwidth-limited*. A consequence for femtosecond spectroscopy is the trade-off between temporal resolution and resolution of the excitation energy, i.e. a higher temporal resolution results in uncertainty of the excitation energy. In transient absorption spectroscopy, excitation of several electronic transitions of a system with a single broadband laser pulse leads to a time-resolved signal that is a combination of relaxation channels from several initial states, a fact which complicates the analysis of transient signals and thus often prevents the study of kinetics on a sub-100 fs time-scale. Fourier transform techniques, such as coherent multidimensional spectroscopy, provide a route to obtaining high temporal resolution, while maintaining excitation energy resolution, by dispersing the measured transient spectrum in the excitation energy dimension, in addition to the detection energy dimension.

2.2 Measurement of femtosecond laser pulses

One of the most popular techniques to measure femtosecond laser pulses is frequency optical gating (FROG), as perfected by Rick Trebino and co-workers. This section will introduce the two FROG implementations commonly used in our laboratory, namely second-harmonic generation- and transient grating FROG, and is mainly based on refs. [13, 14]. The example spectrograms are taken from ref. [15], since the book shows a few 'exotic' cases, which are not commonly found in the literature but proved to be helpful throughout this work.

Since it is very difficult to measure femtosecond laser pulses with an even shorter event (such as an attosecond pulse) they are typically used to measure themselves in an autocorrelation

measurement, which has the mathematical form

$$A(\tau) = \int_{-\infty}^{\infty} I(t)I(t-\tau)dt. \quad (2.9)$$

Here, I is the time dependent intensity and τ is the time delay between the two pulses. A simple intensity autocorrelation measurement however hides eventual temporal structure of a laser pulse, as it yields a smooth response even for a complex laser pulse or for an unstable pulse train [16, 17]. Measuring instead a *spectrogram* of the laser pulse in the time-frequency domain completely determines its electric field. To achieve this the frequency resolve optical gating (FROG) technique uses the laser pulse to gate itself inside a nonlinear optical material and detects the spectrum of the gated signal. It can thus be understood as a spectrally resolved autocorrelation measurement. Using sum-frequency generation (SFG) gating, the spectrogram is expressed as

$$I_{FROG}^{SHG}(\omega, \tau) = \left| \int_{-\infty}^{\infty} E(t)E(t-\tau)e^{-i\omega t} dt \right|^2, \quad (2.10)$$

where $E(t)$ is the time-dependent electric field, ω the radial frequency, and τ the delay between the two pulse replicas. The square-magnitude is simply the result of the square-law detection. Experimentally, two noncollinear replica of the laser pulse are overlapped spatially inside a SFG crystal and one of the two replica pulses is delayed in time by an amount τ . The background-free sum-frequency signal is then spectrally resolved and recorded for a range of delay times around the temporal overlap at $\tau = 0$.

Another experimental realization discussed at this point is transient grating (TG) FROG, in which two time-coincident, noncollinear laser pulses (1 and 2) interfere inside a transparent material and a third pulse (3), with variable delay τ , is scattered off this transient refractive index grating, which is a non-resonant effect and thus only present during the pulse overlap. Mathematically, TG FROG is equivalent to a polarization gating or a self-diffraction gating FROG, depending on which of the three pulses is delayed. Here, I will use the formalism for polarization gating, which is correct if pulse 1 or 3 are delayed. The spectrogram can be

expressed as

$$I_{FROG}^{TG}(\omega, \tau) = \left| \int_{-\infty}^{\infty} E(t) |E(t - \tau)|^2 e^{-i\omega t} dt \right|^2. \quad (2.11)$$

Since the gate function $|E(t - \tau)|^2$ of the TG FROG is a real quantity, it adds no phase information to the gated and then measured temporal slice of $E(t)$. As a consequence, TG FROG is intuitive to interpret as there are no known ambiguities, such as the time-reversal symmetry in SFG FROG.

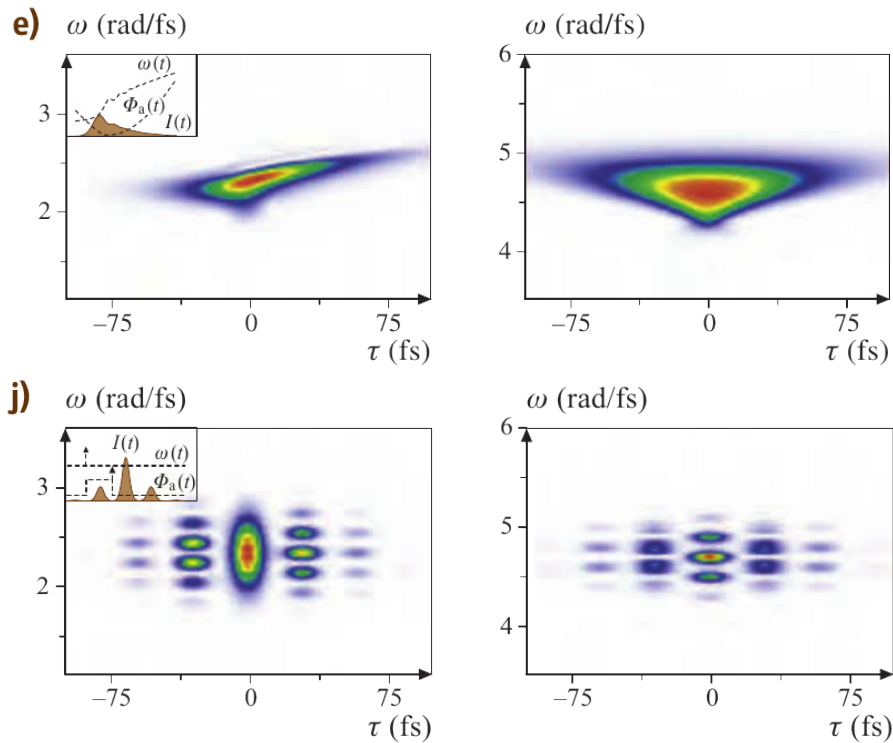


Figure 2.2 – Example FROG spectrograms: e) up-chirped pulse with GDD $\phi'' = 200\text{fs}^2$ and TOD of $\phi''' = 1000\text{fs}^3$. j) Sine modulated pulse at central frequency ω_0 with $\phi(\omega) = 1 \sin[30\text{fs}(\omega - \omega_0)]$. Insets show the envelope of the time-dependent electric field. Reprinted from ref. [15], copyright 2007, with permission from Springer Nature.

A good overview of spectrograms ranging from simple to complex electric fields is given in ref. [14] and [15], and two examples are shown in Figure 2.2. The top row shows the TG (left) and SHG (right) FROG spectrogram for an up-chirped pulse, while the bottom example illustrates the effect of a sine modulated phase function, for which a Taylor-expansion is a bad

approximation, but analytical solutions exist. It becomes clear from the comparison of the up-chirped spectrograms in Figure 2.2 (top row) that the TG FROG often has an easier visual interpretation than the SHG FROG, since it is not symmetric w.r.t. the pulse delay τ .

The most reliable method used to iteratively find the signal field that reproduces the experimental data is the generalized-projections algorithm, which is commonly used in many other phase-retrieval problems. Briefly, the signal field $E(t, \tau)$ has to reproduce (i) the measured FROG trace

$$I_{FROG}(\omega, \tau) = \left| \int_{-\infty}^{\infty} E_{sig}(t, \tau) e^{-i\omega t} dt \right|^2 \quad (2.12)$$

and (ii) meet the mathematical form of the signal field depending on the non-linear optical process used in the measurement

$$E_{sig}(t, \tau) = \begin{cases} E(t)E(t - \tau) & \text{for SHG FROG} \\ E(t)|E(t - \tau)|^2 & \text{for TG FROG.} \end{cases} \quad (2.13)$$

A complete description of the generalized projection algorithm can be found in ref. [14].

2.3 Theory of light-matter interaction

This section will give an introduction to the description of light-matter interaction, to the extent that is required for the understanding of multidimensional spectroscopy, and is largely based on the popular textbooks by Mukamel [18], Cho [19], Valkunas, Abramavicius and Mančal [20], and Hamm and Zanni [21], as well as the well-known manuscript by Hamm [22]. It is intended to guide the reader through the necessary steps to understand the concept of quantum mechanical superpositions, the ensemble density matrix, perturbation theory, Liouville-space pathways, as well as dephasing and relaxation mechanisms, but cannot replace the thorough treatment found in textbooks. Examples of light absorption and emission, as well as time-resolved spectroscopy will show how to apply the formalism and establish the theoretical understanding to analyze and interpret multidimensional spectra.

2.3.1 A quick quantum mechanics primer

To introduce the notions of quantum mechanics (QM) without going into detail we can consider its basic concepts as described by Richard Feynman [23], where

$$\begin{aligned} P &= \text{probability,} \\ \phi &= \text{probability amplitude, and} \\ P &= |\phi|^2. \end{aligned} \tag{2.14}$$

if two quantum pathways from one state of a system to another exist, we need to consider the sum of their probability amplitudes

$$\begin{aligned} \phi &= \phi_1 + \phi_2, \\ P &= |\phi_1 + \phi_2|^2, \end{aligned} \tag{2.15}$$

however, if it is possible to determine which path was taken the interference is lost and the probability becomes

$$P = P_1 + P_2. \tag{2.16}$$

Again without going into any detail, solving the Schrödinger

$$\frac{d}{dt}|\psi\rangle = -\frac{i}{\hbar}H|\psi\rangle \tag{2.17}$$

for a state with definite energy E_0 yields an expression for the time evolution of the wavefunction

$$|\psi\rangle = c_0 e^{-i\frac{E_0}{\hbar}t} |0\rangle. \tag{2.18}$$

The $|\rangle$ denotes a state vector in Dirac notation, such that the wavefunction $\psi(x)$ is represented as $\langle x|\psi\rangle$, and the factor $c_0 e^{-i\frac{E_0}{\hbar}t}$ is the time-dependent probability amplitude

$$\phi_0 = c_0 e^{-i\frac{E_0}{\hbar}t}, \tag{2.19}$$

which states simply that the probability amplitude of finding the the system in state $|0\rangle$ varies periodically in time with frequency $\omega = \frac{E_0}{\hbar}$. However, any measurable quantity such as the probability density $|\langle\psi|\psi\rangle|^2 \equiv |\psi(x, t)|^2$ or the expectation value $\langle A \rangle = \langle\psi|A|\psi\rangle \equiv \int \psi(x, t)^* A \psi(x, t)$ is constant in time, since the amplitude varies as an imaginary exponential [23]. The common understanding is that a system in a state with definite energy is *stationary*.

Allowing two states with different energies E_n and E_m to interfere, is saying that the total system is in a superposition of states $|n\rangle$ and $|m\rangle$ and therefore its state can be written as a linear combination

$$|\psi\rangle = \phi_n|n\rangle + \phi_m|m\rangle. \quad (2.20)$$

Of course, this means that the exact energy of the system cannot be known, but it means as well that the probability of finding the system in either state depends on time, due to the interference term

$$P \propto \text{Re} \{e^{-i(\omega_m - \omega_n)t}\}, \quad (2.21)$$

which would be lost, if either state was measured precisely.

Let us consider the case where this *superposition* of states is created by the interaction of a two-level system with an electric field, since the system has to be treated with QM, while the electric field can be classical. The relevant quantity to consider is the dipole moment, whose QM analog is the dipole operator

$$\langle\boldsymbol{\mu}\rangle = e\langle\mathbf{r}\rangle \quad (2.22)$$

with the elementary charge e and the distance vector between the charges of the dipole \mathbf{r} . As before, the $\langle \rangle$ denote that we are looking at the expectation value of $\boldsymbol{\mu}$ and analogously we see that the interference term oscillates with $\omega_{nm} = \frac{(E_m - E_n)}{\hbar}$

$$\langle\psi_n|\boldsymbol{\mu}|\psi_m\rangle \propto \text{Re} \{e^{-i\omega_{nm}t}\}. \quad (2.23)$$

Chapter 2. Concepts in ultrafast spectroscopy

For the general case that $|n\rangle$ and $|m\rangle$ are associated with spatially varying charge densities the superposition describes a state with an oscillating distribution of charge density, i.e. a dipole Antenna (also called a Hertz dipole) that radiates a field with ω_{nm} .

The last, fundamental concept from QM that is important for the description of light-matter interactions is the notion of a statistical *ensemble*. An ensemble consists of similarly prepared, non-interacting systems with the same internal basis states, which are each either in one of the basis states, or in a superposition. The signals we often measure experimentally are averages of an ensemble, be it by performing many measurements on similarly prepared systems or one measurement on many copies of identical systems, and typically optical experiments fall in the second category. Moreover, the systems of the ensemble can interact with the environment, also called the bath, which results in the loss of coherent properties.

2.3.2 Time-dependence of a quantum mechanical superposition

To describe the interaction between light and matter in more detail let us consider again the solution of the time-dependent Schrödinger equation for a set of basis states $|n\rangle$ which is

$$|\psi\rangle = \sum_n c_n e^{-i\frac{E_n}{\hbar}t} |n\rangle. \quad (2.24)$$

The interaction of a classical electric field with two of the system's eigenstates, $|0\rangle$ and $|1\rangle$, creates a superposition of these eigenstates with the total wavefunction

$$|\psi\rangle = c_0 e^{-i\frac{E_0}{\hbar}t} |0\rangle + i c_1 e^{-i\frac{E_1}{\hbar}t} |1\rangle. \quad (2.25)$$

The factor $c_n e^{-iE_n/\hbar}t$ is the time-dependent probability amplitude ϕ_n of state $|n\rangle$, where c_n is a real, positive number that includes the transition dipole moment, amongst other factors, and the i in Equation (2.25) determines the phase of the rotating wavefunction [21, p. 21]. In the previous section we have already seen that, while classically an oscillating charge leads to the emission of an electric field, in QM it is the time-dependent superposition of states (quasi a non-equilibrium charge distribution) that is responsible for the emission of an electric field. The material property associated with the emitted field via Maxwell's equations is the

time-dependent *macroscopic polarization* $P(t)$, which can be calculated explicitly by taking the expectation value of the dipole operator

$$P(t) = \langle \mu \rangle = \langle \psi(t) | \mu | \psi(t) \rangle. \quad (2.26)$$

Inserting the wavefunction for the superposition between states $|0\rangle$ and $|1\rangle$ (Equation (2.25)) into the expression for the macroscopic polarization (Equation (2.26)) yields [21, p. 21 f]

$$P(t) = c_0^2 \langle 0 | \mu | 0 \rangle + c_1^2 \langle 1 | \mu | 1 \rangle + c_0 c_1 \langle 0 | \mu | 1 \rangle \sin(\omega_{01} t), \quad (2.27)$$

where the energy gap frequency ω_{01} is calculated as $\omega_{01} = \frac{E_1 - E_0}{\hbar}$ and the time-independent terms $c_n \langle n | \hat{\mu} | n \rangle$ correspond to the static dipoles of ground and excited state, which do not contribute to the time evolution of the macroscopic polarization and can thus be neglected.

Looking at an ensemble of two systems with energy gap frequencies $\omega_{01}^{(1)}$ and $\omega_{01}^{(2)}$, the macroscopic polarization becomes the sum

$$P(t) = c_0^{(1)} c_1^{(1)} \mu_{01} \sin(\omega_{01}^{(1)} t) + c_0^{(2)} c_1^{(2)} \mu_{01} \sin(\omega_{01}^{(2)} t). \quad (2.28)$$

This equation describes the following: Immediately after a coherent excitation, which creates a superposition of states in each system, the fields radiated from the individual systems interfere constructively. If $\omega_{01}^{(1)}$ were equal to $\omega_{01}^{(2)}$ for all time and the superpositions in the individual system were not destroyed, the radiated fields would interfere constructively forever. However if $\omega_{01}^{(1)} \neq \omega_{01}^{(2)}$, or if the phases of the systems experience random jumps due to elastic collisions, the macroscopic polarization will disappear after a certain time, since the fields from the systems will eventually interfere destructively. This loss of coherence is due to the interference between systems, i.e. it is an effect of the ensemble, and is called dephasing. The important concept in this example is that in order to describe the macroscopic polarization of an ensemble it suffices to take the statistical average of all systems. It is important to realize that under these circumstances the measurement cannot be described by a single wavefunction anymore, which motivates us to introduce the density matrix of the ensemble.

2.3.3 The density matrix of an ensemble and its expectation value

The *density operator* of an ensemble is defined as

$$\rho(t) = \sum_s p_s |\psi_s(t)\rangle \langle \psi_s(t)|, \quad (2.29)$$

where p_s is the probability of the ensemble occupying the quantum state ψ_s . p_s is non-negative and normalized, and for $p_s = 1$, for any quantum state $|\psi_s\rangle$, the system is in a *pure state*, which could in principle be described by a wavefunction. Otherwise it is said to be in a *mixed state*. In a basis representation with $|\psi_s\rangle = \sum_n c_n^s |n\rangle$ and $\langle \psi_s| = \sum_n c_n^s \langle n|$, Equation (2.29) becomes

$$\rho = \sum_s \sum_{nm} p_s c_n^s c_m^{s*} |n\rangle \langle m| = \sum_{nm} \rho_{nm} |n\rangle \langle m| \quad (2.30)$$

with the *density matrix*

$$\rho_{nm} = \sum_s p_s c_n^s c_m^{s*} = \overline{c_n c_m^*}, \quad (2.31)$$

where the sum over all ensemble states is equivalent to taking the statistical average (denoted as \bar{x}) of the systems composing the ensemble. This expression demonstrates that in an ensemble of systems, which are described by the internal basis states $|n\rangle$, the probability p_s of occupying a quantum state $|\psi_s\rangle$ may vary between the molecules, and the density matrix elements corresponding to the eigenstate coefficients are simply the average over the ensemble [24]. Diagonal ($n = m$) elements $\rho_{nn} = \overline{c_n c_n^*} = p_s \geq 0$ of the density matrix then represent the probability of occupying a quantum state $|n\rangle$ and are referred to as *populations*. Off-diagonal ($n \neq m$) elements $\rho_{nm} = \overline{c_n c_m^*} e^{-i\omega_{nm}t}$ describe the evolution of coherent superpositions of states and are called *coherences*.

Properties of the density matrix:

- $\rho(t)$ is hermitian: $\rho_{nm}^*(t) = \rho_{mn}(t)$
- The diagonal elements ρ_{nn} are non-negative and can be seen as the probability of finding the ensemble in state $|n\rangle$
- Normalization, $\text{Tr}[\rho(t)] = 1$. (Trace operator: $\text{Tr}(K) = \sum_n \langle n|K|n\rangle$)

- $\text{Tr } \rho^2(t) = 1$ for a pure state and $\text{Tr } \rho^2(t) < 1$ for a mixed state and no wavefunction exists that describes a system in which $\text{Tr } \rho^2(t) < 1$.
- Schwartz inequality: $\rho_{nn}\rho_{mm} \geq |\rho_{nm}|^2$.

The difference between a mixed and a pure state is explained graphically in Figure 2.3 and by the following, simple example: The density matrix

$$\rho = \begin{pmatrix} \frac{1}{2} & 0 \\ 0 & \frac{1}{2} \end{pmatrix} \quad (2.32)$$

describes an ensemble in which 50% of the systems are in the ground state $|0\rangle$ and 50% are in the excited state $|1\rangle$. It is said to be *maximally mixed*, and no wavefunction exists that would describe such a system [22, p. 4]. In comparison, the density matrix

$$\rho = \begin{pmatrix} \frac{1}{2} & \frac{1}{2} \\ \frac{1}{2} & \frac{1}{2} \end{pmatrix} \quad (2.33)$$

describes a quantum superposition of a pure state and can be expressed as the wavefunction

$$|\psi\rangle = \frac{1}{\sqrt{2}}(|0\rangle + |1\rangle). \quad (2.34)$$

Note that for the mixed state the probabilities are classical probabilities, while for the quantum superposition of pure states they are probability amplitudes.

What is the difference between a pure and a mixed state? An analogy to the polarization of light. Circularly polarized light is the superposition of s- and p-polarized light with a $\pi/2$ phase shift described by the state vector $|\Psi\rangle = \frac{1}{\sqrt{2}}(|s\rangle + |p\rangle)$. When passing the circularly polarized light through a linear polarizer 50% of its intensity will be transmitted. In the case of unpolarized light 50% of the light intensity will be transmitted as well.

In a single photon picture these probabilities can be thought of as quantum- or classical probabilities. In case of the circularly polarized light the measurement (the polarizer) ‘decides’ whether or not the photon passes (100% or 0%), whereas the unpolarized light consists of a statistical mixture of photons and each photon has a 50% probability to have the correct polarization to pass the polarizer.

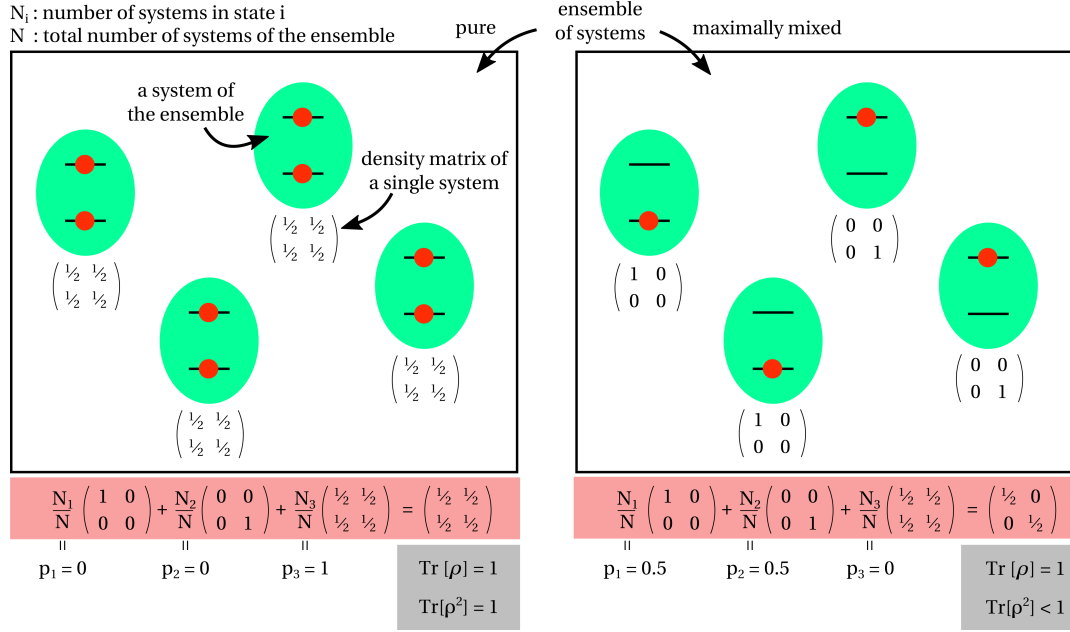


Figure 2.3 – Pictorial explanation of the density matrix for a pure state (left) in which all systems are in a superposition state and a maximally mixed state (right) in which half of the sub-systems are in the ground- and half in the excited state. N_i are the number of systems in state i .

After introducing the concept of the density matrix we can calculate its expectation value $\langle A \rangle = \langle \psi(t) | A | \psi(t) \rangle$ for a generic operator A by expanding the wavefunction into the basis set $|\psi(t)\rangle = \sum_n c_n |n\rangle$ and replacing the sum over the coefficients with the expression for ρ_{nm} from Equation (2.30) and Equation (2.31), which leads to the expression

$$\begin{aligned} \langle A \rangle &= \sum_{n,m} c_n(t) c_m^*(t) \langle n | A | m \rangle = \sum_{n,m} c_n(t) c_m^*(t) A_{nm} \\ &= \sum_{n,m} \rho_{nm}(t) A_{nm} \equiv \text{Tr}[\rho(t) A]. \end{aligned} \tag{2.35}$$

Since the trace operator is linear ($\text{Tr}(cAB) = c\text{Tr}(AB)$), Equation (2.35) holds as well for the density matrix of the ensemble. With this, we arrived at a convenient expression for the expectation value of an ensemble:

$$\langle A \rangle = \text{Tr}[\rho(t) A]. \tag{2.36}$$

2.3.4 Time evolution of the ensemble density matrix

Since we are ultimately interested in the time evolution of the ensemble we derive the time-dependence of the ensemble density matrix by taking the time derivative of Equation (2.31), considering that p_s , c_n , and c_m are time-dependent,

$$\frac{d}{dt}\rho = -\frac{i}{\hbar} [\hat{H}, \rho]_{nm} + \sum_s \frac{dp_s}{dt} c_n c_m^*. \quad (2.37)$$

The full derivation can be found in ref. [21, p. 50 f]. The first term is ‘easy’ to derive from quantum mechanics and corresponds to the Liouville-von Neumann equation, which describes the time evolution of the density operator. The meaning of the second term is more difficult and is treated by statistical mechanics, which leads to a microscopic description of dephasing and population relaxation. Since it is difficult to treat dephasing and population relaxation rigorously, these effects have been introduced phenomenologically by replacing the second term in Equation (2.37) with $\Gamma \rho_{nm}$, where $\Gamma = T_2$ is the dephasing rate [21, p. 52, 28 f]. Examples of a more rigorous treatment of dephasing will be discussed in Subsection 2.3.9.

Perturbative expansion of the density matrix

To examine the time evolution of the ensemble density matrix we will now (i) use the time evolution operator and (ii) perturbatively expand the system Hamiltonian to treat the interaction with the laser field, then (iii) change to the interaction picture to separate the dynamics caused by the perturbation from those intrinsic to the system, and finally (iv) introduce the Liouville representation and describe microscopic theories of dephasing.

If we let the Hamiltonian be time-independent, a time-evolution operator $U(t, t_0)$ can be defined that describes the evolution of a wavefunction

$$|\psi(t)\rangle = U(t, t_0)|\psi(t_0)\rangle = e^{-\frac{i}{\hbar}H(t-t_0)} |\psi(t_0)\rangle. \quad (2.38)$$

Its time derivative is

$$\frac{d}{dt}U(t, t_0) = -\frac{i}{\hbar}HU(t, t_0). \quad (2.39)$$

Chapter 2. Concepts in ultrafast spectroscopy

Adding a small, time dependent perturbation $H'(t)$ – later this will be the electric field of a laser pulse – to the system Hamiltonian H_0 the total Hamiltonian becomes

$$H(t) = H_0 + H'(t), \quad (2.40)$$

where the perturbation Hamiltonian $H'(t)$ is time-dependent, but the system Hamiltonian H_0 remains time-independent. With this the expression for the Hamiltonian, the total wavefunction can be defined as

$$|\psi(t)\rangle \equiv U_0(t, t_0)|\psi_I(t)\rangle, \quad (2.41)$$

where $|\psi(t)\rangle$ is the time evolution of the total wavefunction and $|\psi_I(t)\rangle$ includes both the time-independent and the time-dependent part of the system wavefunction, the latter being due to the weak perturbation $H'(t)$. The subscript I denotes that the wavefunction in the so-called *interaction picture*.

What are all these pictures? In the *Schrödinger picture* of quantum mechanics, the wavefunction is time-dependent, while the operator is not, and the expectation value is calculated as

$$A(t) = \langle \Psi(t) | \hat{A} | \Psi(t) \rangle = \langle \Psi(t_0) | u^\dagger(t, t_0) \hat{A} u(t, t_0) | \Psi(t_0) \rangle$$

, whereas, in the *Heisenberg picture*, the operator is time-dependent instead

$$\hat{A}_H(t) = u^\dagger(t, t_0) \hat{A} u(t, t_0) \quad \rightarrow \quad \bar{A}(t) = \langle \Psi(t_0) | \hat{A}_H(t) | \Psi(t_0) \rangle.$$

In the so called *interaction picture*, both, the operator and wavefunction, become time-dependent. It can be understood as a hybrid between the Schrödinger- and the Heisenberg picture

$$\hat{A}_I(t) \equiv U_0^\dagger(t, t_0) \hat{A}(t) U_0(t, t_0) \quad \text{and} \quad |\Psi_I(t)\rangle \equiv U_i(t, t_0) |\Psi(t_0)\rangle$$

and the expression for the expectation value becomes

$$A(t) = \langle \Psi_I(t) | \hat{A}_I(t) | \Psi_I(t) \rangle.$$

The interaction picture thus separates the dynamics caused by a perturbation (found in the interaction wavefunction $|\Psi_I\rangle$) from those intrinsic to the system (found in the time evolution operator $U(t, t_0)$).

2.3. Theory of light-matter interaction

The time derivative of the interaction picture wavefunction, following the derivation in [22, p. 15], is

$$\frac{d}{dt}|\psi_I\rangle = -\frac{i}{\hbar}H'_I(t)|\psi_I\rangle, \quad (2.42)$$

where the interaction picture Hamiltonian of the perturbation is defined as

$$H'_I(t) = U_0^\dagger(t, t_0)H'(t)U_0(t, t_0) \quad (2.43)$$

and contains the time evolution of the perturbation Hamiltonian. Together with Equation (2.41) the density matrix becomes

$$\rho(t) = |\psi(t)\rangle\langle\psi(t)| = U_0(t, t_0)|\psi_I(t)\rangle\langle\psi_I(t)|U_0^\dagger(t, t_0) = U_0(t, t_0)\rho_I(t)U_0^\dagger(t, t_0), \quad (2.44)$$

where $\rho_I(t)$ is now the density matrix in the interaction picture and the dagger denotes the Hermitian adjoint. Its time derivative is formally equivalent to the Liouville-von Neumann equation

$$\frac{d}{dt}\rho_I(t) = -\frac{i}{\hbar}[H'_I(t), \rho_I(t)], \quad (2.45)$$

which can be solved by formal integration and iteratively plugging the solution into itself. Its power expansion in terms of the perturbation reads

$$\begin{aligned} \rho_I(t) = \rho_I(t_0) + \sum_{n=1}^{\infty} \left(-\frac{i}{\hbar}\right)^n \int_{t_0}^t d\tau_n \int_{t_0}^{\tau_n} d\tau_{n-1} \dots \int_{t_0}^{\tau_1} d\tau_1 \\ [H'_I(\tau_n), [H'_I(\tau_{n-1}), \dots [H'_I(\tau_1), \rho(t_0)] \dots]]. \end{aligned} \quad (2.46)$$

Importantly, the expansion is only in the perturbation and *not* the full Hamiltonian, which could be done as well but would not converge very quickly, cf. ref. [22, p. 12 f] for details. Switching the density matrix back to the Schrödinger picture and using the perturbation $H'(t) = E(t)\hat{\mu}$ caused by an electric field, where $E(t)$ is the time-dependent electric field and $\hat{\mu}$

is the transition dipole operator¹, Equation (2.46) becomes

$$\rho^{(n)}(t) = \rho^{(0)} + \sum_{n=1}^{\infty} \rho^{(n)}(t) \quad (2.47)$$

with

$$\begin{aligned} \rho^{(n)}(t) = & - \left(-\frac{i}{\hbar} \right)^n \int_{t_0}^t d\tau_n \int_{t_0}^{\tau_n} d\tau_{n-1} \cdots \int_{t_0}^{\tau_2} d\tau_1 E(\tau_n) E(\tau_{n-1}) \cdots E(\tau_1) \\ & \cdot e^{-\frac{i}{\hbar} \hat{H}_0(t-t_0)} [\hat{\mu}_I(\tau_n), [\hat{\mu}_I(\tau_{n-1}), \cdots [\hat{\mu}_I(\tau_1), \rho(t_0)] \cdots]] e^{+\frac{i}{\hbar} \hat{H}_0(t-t_0)}, \end{aligned} \quad (2.48)$$

where the transition dipole moment $\mu_I(t) = U_0^\dagger(t, t_0) \mu U_0(t, t_0)$ is in the interaction picture. It is common practice to discard the subscript I , since the notation μ or $\mu(t)$ specifies explicitly if an expression is in the Schrödinger or the interaction picture. Multiplication with the dipole moment operator and subsequently taking the trace $\langle \dots \rangle$ yields an expression for the n th order macroscopic polarization

$$P^{(n)}(t) = \text{Tr}(\mu(t) \rho^{(n)}(t)) \equiv \langle \mu(t) \rho^{(n)}(t) \rangle \quad (2.49)$$

and, since $\rho(t_0)$ is stationary, we set $t_0 \rightarrow -\infty$ so that

$$\begin{aligned} P^{(n)}(t) = & - \left(-\frac{i}{\hbar} \right)^n \int_{-\infty}^t d\tau_n \int_{-\infty}^{\tau_n} d\tau_{n-1} \cdots \int_{-\infty}^{\tau_2} d\tau_1 E(\tau_n) E(\tau_{n-1}) \cdots E(\tau_1) \\ & \cdot \langle \hat{\mu}(t) [\hat{\mu}(\tau_n), [\hat{\mu}(\tau_{n-1}), \cdots [\hat{\mu}(\tau_1), \rho(-\infty)] \cdots]] \rangle. \end{aligned} \quad (2.50)$$

We made use of the fact that the trace is invariant to cyclic permutation and unitary transformations and thus $\langle e^{+\frac{i}{\hbar} \hat{H}_0(t-t_0)} e^{-\frac{i}{\hbar} \hat{H}_0(t-t_0)} \rangle = 1$. The expression within the trace of Equation (2.50) together with the factor $-\left(-\frac{i}{\hbar}\right)^n$ is called the n th order response function

$$R^{(n)} = - \left(-\frac{i}{\hbar} \right)^n \langle \hat{\mu}(t) [\hat{\mu}(\tau_n), [\hat{\mu}(\tau_{n-1}), \cdots [\hat{\mu}(\tau_1), \rho(-\infty)] \cdots]] \rangle \quad (2.51)$$

and Equation (2.50) is the convolution of n electric fields with this n th order response function. Note that the last interaction, $\hat{\mu}(t)$, is different from the previous, as it describes the signal

¹Whose off-diagonal elements $\hat{\mu} = \begin{pmatrix} 0 & \mu_{01} \\ \mu_{10} & 0 \end{pmatrix}$ couple states $|0\rangle$ and $|1\rangle$.

emission.

The third order polarization is

$$P^{(3)}(t) \propto \int_0^\infty dt_3 \int_0^\infty dt_2 \int_0^\infty dt_1 E_3(t-t_3) E_2(t-t_3-t_2) \cdot E_1(t-t_3-t_2-t_1) R^{(3)}(t_3, t_2, t_1), \quad (2.52)$$

where the absolute time points τ_n have been replaced by time the intervals $t_n = \tau_{n+1} - \tau_n$, since these are the experimentally relevant quantities. This expression is quite similar to the one derived in nonlinear optics, where

$$\begin{aligned} P &= \epsilon_0 \chi E = P^{(1)} + P^{(2)} + p^{(3)} + \dots \\ &= \epsilon_0 (\chi^{(1)} E + \chi^{(2)} EE + \chi^{(3)} EEE + \dots) \end{aligned} \quad (2.53)$$

with the vacuum permittivity ϵ_0 , the nonlinear susceptibility $\chi^{(n)}$, and the electric field E .

2.3.5 Response functions and their representation using vertical Feynman diagrams

Taking the trace of the product between the transition dipole operator and the density matrix shows that $P(t)$ depends on the off-diagonal elements of $\rho(t)$ only, i.e. a coherence is responsible for a macroscopic polarization. This can be seen when evaluating $\langle \mu \rho(t) \rangle$ for a two-level system

$$P(t) = \langle \mu \rho(t) \rangle = \left\langle \begin{pmatrix} 0 & \mu_{12} \\ \mu_{21} & 0 \end{pmatrix} \begin{pmatrix} \rho_{11} & \rho_{12} \\ \rho_{21} & \rho_{22} \end{pmatrix} \right\rangle = \rho_{12} \mu_{21} + \rho_{21} \mu_{12}. \quad (2.54)$$

Remember the argument that a superposition of states is responsible for the creation of an electric field, at the beginning of this section. Writing out the commutator expression for the third-order response function, multiplying with the transition dipole moment operator, and

taking the trace leads to the expression

$$\begin{aligned}
 R^{(3)}(t_1) \propto & \langle \mu(t_3 + t_2 + t_1)\mu(t_2 + t_1)\mu(t_1)\mu(0)\rho(-\infty) \rangle + c.c. \Rightarrow R_4 + R_4^* \\
 & + \langle \mu(t_3 + t_2 + t_1)\mu(t_2 + t_1)\rho(-\infty)\mu(0)\mu(t_1) \rangle + c.c. \Rightarrow R_3 + R_3^* \\
 & + \langle \mu(t_3 + t_2 + t_1)\mu(t_1)\rho(-\infty)\mu(0)\mu(t_2 + t_1) \rangle + c.c. \Rightarrow R_2 + R_2^* \\
 & + \langle \mu(t_3 + t_2 + t_1)\mu(0)\rho(-\infty)\mu(t_1)\mu(t_2 + t_1) \rangle + c.c. \Rightarrow R_1 + R_1^*
 \end{aligned} \tag{2.55}$$

Each term of Equation (2.55) describes an interaction pathway of the density matrix with the three electric fields, via the transition dipole operators and they are often referred to as *response functions* or *Liouville-space pathways*.

Let us consider the first term of this equation. It reads as follows: The first electric field interacts at $t = 0$ from the left with (i.e. with the ket of) the equilibrium density matrix and creates a $|1\rangle\langle 0|$ coherence. The coherence evolves in time as $e^{-i\omega_0 t}$ until the second interaction at t_1 , again from the left, transfers the coherence back into a ground state population $|0\rangle\langle 0|$. This population state evolves in time until the third interaction at $t_2 + t_1$, again from the left, creates another coherence $|1\rangle\langle 0|$, which is responsible for the emission of a signal field, which is described by the multiplication with the dipole operator at $t_3 + t_2 + t_1$ and taking the trace.

Since it is tedious to write out the response functions we can use vertical Feynman diagrams to visualize them. The rules for this pictorial representation are summarized in Figure 2.4 for the R_3 pathway in Equation (2.55), which describes a ground state bleach.

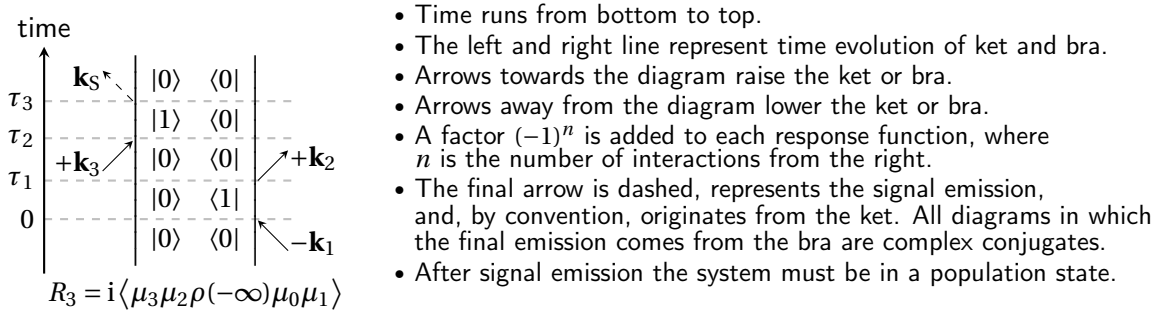


Figure 2.4 – Rules for writing and reading double-sided vertical Feynman diagrams. The notation $\mu(t_n + t_{n-1} + \dots + t_1)$ has been abbreviated as μ_n .

An alternative way of thinking about Liouville-space pathways is the ladder diagram, as exemplified in Figure 2.5 for the case of the an excited state absorption pathway, which is not found amongst the pathways for a two-level system in Equation (2.55).

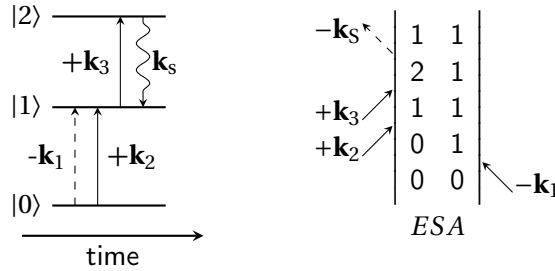


Figure 2.5 – (left) An alternative way to describe the excited state absorption Liouville-space pathway is the ladder diagram. Interactions with the bra (ket) of the density matrix are drawn as dashed (solid) arrows and the final emission as a wiggly arrow. Time runs from left to right. (right) The corresponding vertical Feynman diagram.

Ultimately, the system evolution in the time interval t_2 is of interest for the experimentalist and the coherences during t_1 and t_3 are ‘tools’ to obtain the excitation- and detection frequency dependence of the system evolution.

2.3.6 Time-ordering and the rotating wave approximation

Just above we have described three different response pathways. The R_4 pathway in Equation (2.55) involved two coherences with the ket in the excited state and the bra in the ground state, which implies that the phase evolution of the first and second coherence is in-phase and hence the pathway is called non-rephasing. In the pathway shown in Figure 2.4, the second coherence is phase conjugate to the first, leading to the rephasing of the signal and the appearance of a *photon echo*. The third pathway in Figure 2.5 is rephasing and describes an excited state absorption (ESA) in a three-level system. We could write out all different response pathways, but when convoluted with the electric fields the expression for the third-order macroscopic polarization of a *two-level system alone* has $6 \times 6 \times 6 \times 4 = 864$ terms. $6 \times 6 \times 6$ terms since each electric field in Equation (2.52) is the sum of 3 electric fields, which in turn consist of two terms with positive and negative frequency, and there are 4 distinct Liouville-space pathways, if we count R_n and R_n^* together.

If we assume **time-ordering** of the pulses, i.e. the interaction from pulse 1 comes before the one from pulse 2, which comes before the interaction from pulse 3, the number of possible interactions decreases to $2 \times 2 \times 2 \times 4 = 36$. This is realistic when the pulse delay is larger than the pulse length and in this situation it is common to assume δ -pulses, which is called the semi-impulsive limit.

$$\begin{array}{cc}
 \begin{array}{c}
 -\mathbf{k}_s \swarrow \\
 \begin{array}{|c|} \hline 0 \quad 0 \\ \hline 1 \quad 0 \\ \hline 0 \quad 0 \\ \hline \end{array} \\
 \nearrow +\mathbf{k}_1
 \end{array} &
 \begin{array}{c}
 -\mathbf{k}_s \swarrow \\
 \begin{array}{|c|} \hline 0 \quad 0 \\ \hline ? \quad 0 \\ \hline 0 \quad 0 \\ \hline \end{array} \\
 \nearrow +\mathbf{k}_1
 \end{array} \\
 -\frac{i}{\hbar} \mu_{10}^2 e^{-i\omega t} \int_0^\infty dt_1 E_0(t-t_1) e^{-\Gamma t_1} &
 -\frac{i}{\hbar} \mu_{10}^2 e^{+i\omega t} \int_0^\infty dt_1 E_0(t-t_1) e^{-\Gamma t_1} e^{-i2\omega t_1}
 \end{array}$$

Figure 2.6 – Vertical Feynman diagrams illustrating the rotating wave approximation. The expressions below each diagram show that for the right Liouville-space pathway, the argument of the integral oscillates with 2ω .

A second assumption is the **rotating wave approximation** (RWA), which reduces the number of terms to $1 \times 1 \times 1 \times 4$. If the electric field is written as

$$E(t) = E_0(t)(e^{-i\omega t} + e^{+i\omega t}), \quad (2.56)$$

the expression for $P(t)$ contains integrands that slowly vary in time ($e^{-i0\omega t}$), as well as integrands that are highly oscillatory ($e^{-i2\omega t}$). The integral of a term oscillating at 2ω is however essentially zero for near resonance conditions and for a slowly varying envelope $E_0(t)$, i.e. more slowly than the carrier frequency ω [22]. We can thus discard all integrands with highly oscillatory terms, since they will not contribute significantly to the macroscopic polarization. Figure 2.6 illustrates the RWA. In the left case the interaction of the system with the electric field acts on the ket of the density matrix to yield a coherence between the excited and the ground state $|1\rangle\langle 0|$. In the right case the interaction with the electric field would lead to a deexcitation of the ground state ket, which is physically impossible [22].

2.3.7 Rephasing and non-rephasing response functions

Finally, via **phase matching** only Liouville-space pathways that are emitted in a specific spatial direction, i.e. with a specific \mathbf{k} -vector, are selected. Figure 2.7 shows the Feynman diagrams for

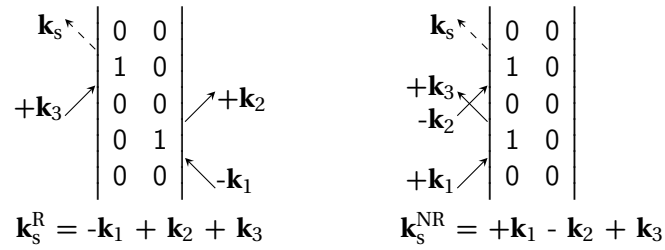


Figure 2.7 – Example of (left) a rephasing and (right) a non-rephasing Liouville-space pathway.

$\mathbf{k}_s^R = -\mathbf{k}_1 + \mathbf{k}_2 + \mathbf{k}_3$ and $\mathbf{k}_s^{\text{NR}} = \mathbf{k}_1 - \mathbf{k}_2 + \mathbf{k}_3$ for a two-level system. Note that the second coherence in the left diagram is phase conjugate w.r.t. the first coherence. This pathway leads to the *rephasing* (R) of the macroscopic polarization. In the right diagram the second coherence is in-phase with the first and thus the pathway is *non-rephasing* (NR).

The R and NR response functions lead similar expressions for the macroscopic polarization:

$$P_R^{(3)} \propto e^{-i2\pi\omega_{01}(t_1-t_3)} e^{-\Gamma(t_1+t_3)} e^{-\sigma^2 \frac{(t_1-t_3)^2}{2}} \quad (2.57)$$

and

$$P_{\text{NR}}^{(3)} \propto e^{-i2\pi\omega_{01}(t_1+t_3)} e^{-\Gamma(t_1+t_3)} e^{-\sigma^2 \frac{(t_1-t_3)^2}{2}}. \quad (2.58)$$

The first exponential term is due to the coherences, while the second and third exponential terms phenomenologically introduce dephasing via the dephasing rate $\Gamma = 1/T_2$, and inhomogeneous broadening via the width σ of the inhomogeneous distribution, respectively.

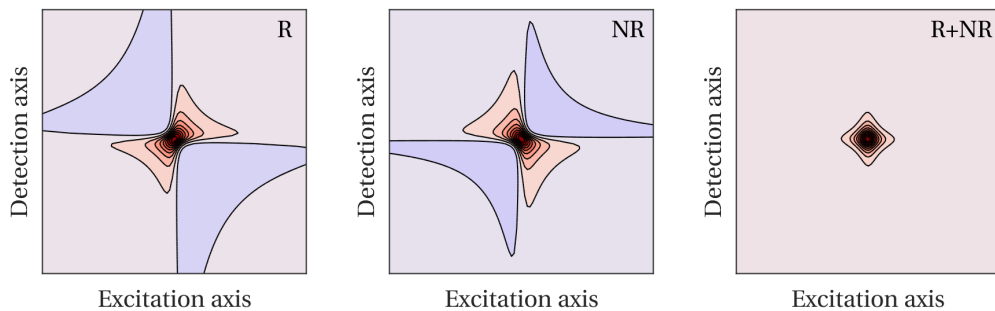


Figure 2.8 – Comparison between the (left) rephasing, (middle) non-rephasing, and (right) absorptive 2D spectrum, which is the addition of the R and NR spectra. Improper weighing off either R or NR component leads to ‘phase twists’ in the absorptive 2D spectrum.

Note that the sign of t in the first exponential is different for the two pathways, leading to the rephasing of the macroscopic polarization in Equation (2.57) after $t = \tau$. Figure 2.8 shows 2D spectra calculated according to (left) Equation (2.57) and (middle) Equation (2.58), and we see that in these R and NR spectra only spectral slices at resonance yield absorptive lineshapes [25]. Phase shifts away from $\omega_t = 0$ or $\omega_\tau = 0$ result in the mixing of absorptive and dispersive lineshapes, which can be recovered as the real- and imaginary part of the complex 2D spectrum by adding properly weighted R and NR spectra. Due to the distortion of the R and NR lineshapes, absorptive 2D spectra are preferred over rephasing and non-rephasing 2D spectra, when it comes to the identification of transient signals. However, the distinction between R and NR signals is advantageous in determining the origin of coherences in the population time of the system, cf. Subsection 2.5.3.

2.3.8 The Liouville representation

A final aspect that is worth considering is how to treat **dephasing** in the response function formalism. Writing out the commutator of the Liouville-von Neumann equation (first term in Equation (2.37)) and reordering for the individual elements $aa, bb, \dots, ab, \dots, ba, \dots$ leads to the *Liouville representation* [18, p. 53 ff]

$$\frac{d}{dt}\rho_{jk} = -\frac{i}{\hbar} \sum_{nm} \mathcal{L}_{jk,nm} \rho_{nm}, \quad (2.59)$$

where the density matrix has been reordered as a vector with N^2 elements and the Liouville superoperator \mathcal{L} , a $N^2 \times N^2$ matrix in Liouville space with 4 indices per element, is defined as

$$\mathcal{L} = H_{jm}\delta_{kn} - H_{kn}^* \delta_{jm} \quad (2.60)$$

such that, if it is applied to the density matrix, the expressions reads

$$\mathcal{L}\rho = H\rho - \rho H \equiv \mathcal{L}\rho = [H, \rho], \quad (2.61)$$

where the right-hand side is the corresponding notation in Hilbert space. For a two-level system with states $|0\rangle$ and $|1\rangle$ Equation (2.59) reads

$$\frac{d}{dt} \begin{pmatrix} \rho_{00} \\ \rho_{11} \\ \rho_{01} \\ \rho_{10} \end{pmatrix} = +\frac{i}{\hbar} \begin{bmatrix} 0 & 0 & -V_{10} & V_{01} \\ 0 & 0 & V_{10} & -V_{01} \\ -V_{01} & V_{01} & E_0 - E_1 & 0 \\ V_{10} & -V_{10} & 0 & E_1 - E_0 \end{bmatrix} \begin{pmatrix} \rho_{00} \\ \rho_{11} \\ \rho_{01} \\ \rho_{10} \end{pmatrix} \quad (2.62)$$

with the energies of the levels E_a and E_b , and the perturbation V . Liouville and density matrix representation are equivalent as they describe the same physics, however, the Liouville representation simplifies the treatment of dephasing significantly. To describe dephasing in the density matrix representation phenomenologically via the dephasing rate $\Gamma = \frac{1}{T_2}$ we could write the following expression for *every* off-diagonal density matrix element ([22, p. 6])

$$\dot{\rho}_{nm} = -\frac{i}{\hbar}(E_n - E_m)\rho_{nm} - \Gamma\rho_{nm} \quad \text{for } n \neq m, \quad (2.63)$$

which leads to $(N^2 - N)$ equations. In the Liouville representation this simplifies to a single expression

$$\frac{d}{dt}\rho = -\frac{i}{\hbar}\mathcal{L}\rho - \Gamma\rho. \quad (2.64)$$

2.3.9 Treatment of dephasing: Kubo's theory and the Brownian oscillator

With the dephasing rate Γ the time evolution of the off-diagonal elements of the density matrix becomes $e^{i\omega_{mn}t} e^{-\Gamma t} = e^{i\omega_{mn}t} e^{-t/T_2}$ [21, p. 52 f], leading to a simple expression for the third order polarization

$$P^{(3)}(t_1, t_2, t_3) = \frac{i}{\hbar^3} \mu^4 e^{-i\omega_{nm}(t_1-t_3)} e^{-\Gamma(t_1+t_3)} e^{-\sigma^2 \frac{(t_1-t_3)^2}{2}}. \quad (2.65)$$

Kubo introduced the idea of a stochastic time-dependence of the energy gap frequency $\omega \rightarrow \omega(t)$ that describes the lineshape broadening of nonlinear signals. With this, the expression

Chapter 2. Concepts in ultrafast spectroscopy

for the time derivative of off-diagonal dipole operator elements becomes

$$\frac{d}{dt}\mu_{nm}(t) = i\omega_{nm}(t)\mu_{nm}(t) \quad (2.66)$$

and thus the solution for $\mu_{01}(t)$ contains the integration of the time evolution of the energy gap frequency $\omega_{nm}(t)$. The latter can be decomposed into an average frequency and a fluctuating frequency $\delta\omega$ [22, p. 43 f]. Microscopically, dephasing can then be described by considering that every system of an ensemble possesses an energy gap frequency that fluctuates stochastically in time. Right after a coherent excitation event all the system emit coherently, but since their frequencies change over time, their emissions will quickly dephase and the macroscopic polarization will vanish. Note that this does not mean that the coherences of the independent systems have been damped. A good example for the latter is the wavepacket revival in time-resolved spectroscopy of molecules in the gas phase [26]. Kubo's theory leads to the lineshape function

$$g(t) = \frac{1}{2} \int_0^t \int_0^t d\tau' d\tau'' \langle \delta\omega(\tau' - \tau'') \delta\omega(0) \rangle + O(\delta\omega^3) \quad (2.67)$$

which replaces the phenomenologically expression $e^{-\Gamma t}$ by $e^{-g(t)}$. The lineshape is thus determined by the frequency-frequency correlation function $\langle \delta\omega(\tau' - \tau'') \delta\omega(0) \rangle$, which in the fast modulation, or homogeneous limit reads

$$g(t) = t/T_2 \quad \text{with} \quad T_2 = (\Delta^2 \tau_c)^{-1} \quad (2.68)$$

and in the slow modulation, or inhomogeneous limit

$$g(t) = \frac{\Delta^2}{2} t^2, \quad (2.69)$$

where Δ is the fluctuation amplitude and τ_c the correlation time.

A microscopic interpretation of Kubo's theory is provided by the Brownian oscillator model. Starting all over with the definition of the time evolution operator in Equation (2.38) but this time letting the Hamiltonian be time-*dependent* results in a modified expression for the

derivative of the time-evolution operator

$$\frac{d}{dt}U_0(t, t_0) = -\frac{i}{\hbar}H(t)U(t, t_0). \quad (2.70)$$

Integration and iterative substitution leads to a solution of time-order integrals [22, p. 55 f], similar, but not identical, to the results above. In essence, while Kubo's theory of dephasing postulates that the solvent is responsible for the time-dependent change in energy gap frequency of the solute, the Brownian oscillator model gives a microscopic, i.e. quantum mechanical, explanation of its origin. Briefly, by describing the electronic states of a system as a set of displaced harmonic oscillators any change in the nuclear coordinate q will result in a linear change of the energy gap frequency. This provides an elegant connection of the lineshape to QM and allows the calculation of absorption spectra, as well as the description of equilibrium system dynamics and the Stokes shift.

2.3.10 Examples: Absorption and fluorescence

Absorption of light

To illustrate the formalism that was developed in the previous section we describe the absorption of light. The most simple way to think of the absorption of a photon is that the photon excites an electron from an occupied system state to an unoccupied state with higher energy. The photon provides the energy that is required by the electron, i.e. its energy is resonant with the transition energy. Figure 2.9 describes the absorption of light in the response function formalism. In this picture the interaction with the electric field $+E_1$ creates a coherence between the ground- and excited state, $|0\rangle$ and $|1\rangle$. This coherence radiates an electric field that is phase shifted from the excitation field

$$E^{(1)}(t) \propto -iP^{(1)}(t), \quad (2.71)$$

which follows from Maxwell's equations. Since the observer is behind the sample, the excitation field will interfere destructively with the signal field, i.e. the light intensity after the sample is reduced, i.e. the light has been absorbed. The circumstance that we detect the interference between the signal and the reference (here also the excitation) field is responsible

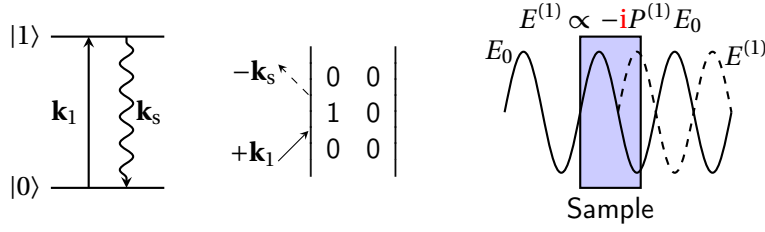


Figure 2.9 – (left) Ladder diagram and (middle) double sided Feynman diagram describing the response function of light absorption in a two-level system. (right) The macroscopic polarization generates a signal field that is phase shifted w.r.t. the exciting field and their destructive interference, as seen by an observer behind the sample, is interpreted as the absorption of light.

for the physical interpretation of absorption and we say that the signal is heterodyne detected.

The expression for the 1st order macroscopic polarization reads

$$\begin{aligned}
 P^{(1)} &= -\frac{i}{\hbar} \int_0^{\infty} dt_1 \cdot \langle \mu(t_1) [\mu(0), \rho(-\infty)] \rangle \\
 &= -\frac{i}{\hbar} \int_0^{\infty} dt_1 (\langle \mu(t_1) \mu(0) \rho(-\infty) \rangle - \langle \mu(t_1) \rho(-\infty) \mu(0) \rangle) \\
 &= -\frac{i}{\hbar} \int_0^{\infty} dt_1 (\langle \mu(t_1) \mu(0) \rho(-\infty) \rangle - \langle \rho(-\infty) \mu(0) \mu(t_1) \rangle),
 \end{aligned} \tag{2.72}$$

where the transition dipole operators $\mu(0)$ and $\mu(t_1)$ represent the interaction of the light field with the density matrix at time 0 and after an interval t_1 . In the last step we used the invariance of the trace to cyclic permutation to show that the two terms of the 1st order response function are complex conjugates, i.e. that they describe the same physical process.

Fluorescence

Since the intensity of fluorescence scales linearly with the intensity of the incident light field, it intuitively appears to be a linear process. However, fluorescence is described by a 3rd order response function with $\omega_S = -\omega_L + \omega_L + \omega_S$, where L is the classical excitation light field and S stands for the scattered light field, which contains no photons initially and one photon after the emission process. This requires a QM treatment of the field, which, unlike for classical fields, does not show up in the signal amplitude [18, p. 261 ff].

$$\begin{array}{c}
 \mathbf{k}_S \nearrow \\
 +\mathbf{k}_L \nearrow
 \end{array}
 \left|
 \begin{array}{cc}
 0 & 0 \\
 1 & 0 \\
 1 & 1 \\
 0 & 0
 \end{array}
 \right|
 \begin{array}{c}
 \nearrow +\mathbf{k}_S \\
 \nwarrow -\mathbf{k}_L
 \end{array}$$

Figure 2.10 – Feynman diagram for fluorescence.

More precisely, the ω_S mode is initially in the vacuum state and spontaneous emission is the consequence of vacuum fluctuations of the radiation field. Interestingly, if the order of field interactions were swapped to $-\mathbf{k}_L - \mathbf{k}_S - \mathbf{k}_L - \mathbf{k}_S$ the response function would describe a Raman scattering process instead.

2.4 Transient absorption spectroscopy

2.4.1 Observable transient signals in the visible

Transient absorption spectroscopy measures the change in absorption upon photoexcitation of a sample. It can be described by the response function formalism by setting $\mathbf{k}_1 = \mathbf{k}_2$ and $t_1 = 0$. Then we can use the Feynman diagrams in Figure 2.16 to describe three different transient features that can be observed in a TA measurement and are illustrated in Figure 2.11: ground state bleach (GSB), stimulated emission (SE), and excited state absorption (ESA). Physically the GSB is a result of the lack of ground state electrons in the system, i.e. after photoexcitation less electrons are in the S_0 state and thus less photons can be promoted by the resonant electric field in a $S_0 \rightarrow S_n$ transition. The electrons in the S_n state can be promoted

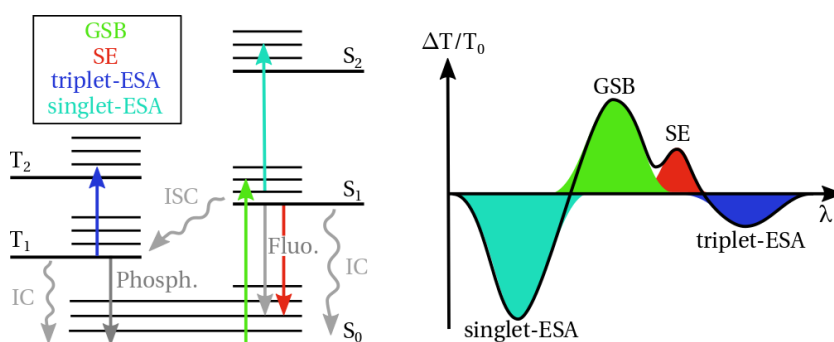


Figure 2.11 – (left) Jablonski diagram showing the different signal- (colors) and relaxation (gray) channels in a pump-probe experiment. Straight arrows indicate radiative-, wiggly arrows non-radiative processes. (right) Exemply transient spectrum illustrating the signals.

to even higher electronic states S_m ($m \geq n$) by the probe pulse ($S_n \rightarrow S_m$) in an ESA, or they can decay to the ground state, stimulated by a photon of the probe pulse ($S_0 \leftarrow S_n$). Since the latter creates an additional photon, the overall number of photons in the probe field is increased after the sample, and the transient signal of the SE appears with the same sign as the GSB. The sign of the signal can also be deduced from the prefactor $(-1)^n$ of the response function, where n is the number of interactions with the bra. In general, SE can only occur at frequencies lower than the excitation frequency and often originates from the S_1 state, due to very fast internal conversion (IC) processes within the singlet manifold of states (Kasha's rule). Note that, while the observed SE originates from a singlet state, ESA can occur within the singlet- or the triplet manifold of electronic states.

2.4.2 Relaxation channels

The initially excited electrons will eventually decay to the ground state via non-radiative processes, such as internal conversion (IC), intersystem crossing (ISC), and vibrational relaxation (VR, not shown), as well as radiative processes, namely fluorescence and phosphorescence. While IC is the relaxation between electronic states within a manifold states of the same multiplicity, ISC involves a change of multiplicity during the electronic relaxation. VR describes the loss of vibrational while the system is in an electronic state is called. TA spectroscopy indirectly yields insight into the cascade of energy relaxation processes, via the signals described above. Typically, a certain process will have a very specific time scale, i.e. VR relaxation will occur within a few picoseconds, while ISC, a forbidden process, since it involves a change in spin multiplicity, will typically occur on a few picosecond to 100s of picosecond time scale.

The time scales in Table 2.1 are commonly encountered time scales, however many cases exist in which relaxation processes do not fall within these ranges. Examples are the counterintuitive ultrafast ISC times in metal- complexes [27–29], which cannot be justified using spin-orbit coupling arguments. Instead it was found that solvent- and vibrational degrees of freedom play an important role in these fundamental processes [30–32].

A last aspect that is worth considering is that the time constants that can be obtained from a transient measurement merely reflect the *apparent* rate constants of a relaxation process [33].

Table 2.1 – Summary of typical time scales associated with energy relaxation channels. Many of the current problems in physical chemistry deal with relaxation channels that do not obey these time scales.

	time scale [s]
<i>radiative relaxation</i>	
fluorescence	$10^{-9} - 10^{-7}$
phosphorescence	$10^{-3} - 10^2$
<i>non-radiative relaxation</i>	
vibrational relaxation	$10^{-14} - 10^{-11}$
internal conversion	$10^{-14} - 10^{-11}$
intersystem crossing	$10^{-10} - 10^{-8}$

E.g. a reaction mechanism that feeds the same final state through two different reaction pathways will have an apparent rate of product formation that is the combination of the individual pathways and thus different from the *intrinsic* rate constants that describe the individual pathways. One of the promises of multidimensional spectroscopy is that the information about the excitation frequency, which is not available in TA spectroscopy, can be exploited to extract the intrinsic rate constants directly from the spectroscopic observables [34].

2.4.3 Anisotropy and molecular structure

Transient absorption anisotropy (TAA) can be used to study molecular dynamics, i.e. the connection between electronic relaxation and structural changes, in addition to the pure kinetics of the system. The anisotropy of a transient absorption signal is due to the orientational difference between the excited- and the observed transition dipole moment [35]

$$r(t) = \frac{3[\boldsymbol{\mu}_{\text{ex}}(t)\boldsymbol{\mu}_{\text{ob}}(t)]^2}{5} = \frac{3\cos^2\{\beta(t)\}}{5}. \quad (2.73)$$

Here, $\boldsymbol{\mu}_{\text{ex}}$ and $\boldsymbol{\mu}_{\text{ob}}$ are the excited and observed transition dipole moments, respectively, and β is the angle between them. Since the relative orientation between $\boldsymbol{\mu}_{\text{ex}}$ and $\boldsymbol{\mu}_{\text{ob}}$ can vary with time, due to changes of the molecular structure or the electronic relaxation from one excited state to another, the observed signal anisotropy is time-dependent. This can be exploited to follow energy relaxation pathways within a system and gain information about the relationship between its electronic- and geometric structure. An overview of time-resolved- and broadband anisotropy can be found in refs. [36–40].

Eventually, rotation of the molecules will randomize the anisotropy and the associated time constant t_R can be compared to the rotational diffusion constant via the Stokes-Einstein equation [41]

$$t_R = \frac{1}{D_R} = \frac{\eta V}{k_B T}, \quad (2.74)$$

where D_R is the rotational diffusion constant, η is the viscosity of the solvent, V is the hydrodynamic volume of the molecule, and k_B and T are the Boltzmann constant and the temperature, respectively.

An experimental complication arises from the fact that the measured TAA signal is a linear combination of the individual anisotropies for the GSB, ESA and SE weighted by the corresponding transient signal relative to the total transient [37]

$$r = \frac{\Delta OD_{\text{GSB}}}{\Delta OD} r_{\text{GSB}} + \frac{\Delta OD_{\text{ESA}}}{\Delta OD} r_{\text{ESA}} + \frac{\Delta OD_{\text{SE}}}{\Delta OD} r_{\text{SE}}. \quad (2.75)$$

Here, ΔOD_{GSB} , ΔOD_{ESA} and ΔOD_{SE} are the isolated transient signal associated with the GSB, ESA, and SE, and ΔOD is the total transient signal. r_{GSB} , r_{ESA} and r_{SE} are the time-dependent anisotropy of the component. Since the transient features in a TA measurement generally overlap spectrally, it is often difficult to use the TAA quantitatively. Takaya et al. illustrate how it is possible to decomposed TAA spectra into its components [42], but the analysis becomes increasingly complicated with increasing complexity of transient signals.

2.5 Coherent multidimensional spectroscopy

Two-dimensional photon echo (2DPE) spectroscopy is an experimental technique that resolves the excitation energy dimension of a transient signal. 2D spectra reveal information about a system that cannot be obtained by TA spectroscopy, namely the homogeneous linewidth of an optical transition and the mechanism for inhomogeneous broadening, as well as the energy relaxation pathways, via the correlation between the excitation- and detection frequencies. In addition it allows to study truly ultrafast (sub-100 fs) molecular dynamics, since it is not limited by the time-energy uncertainty. *In this thesis I use the convention that the x-axis*

corresponds to the excitation- and the y-axis to the detection dimension and, unless otherwise noted, units are given in wavenumbers to facilitate the comparison between the transient spectra and vibrational coherences.

2.5.1 Microscopic picture of two-dimensional photon echo spectroscopy

Figure 2.12 shows the pulse sequence of a three pulse photon echo experiment in black and the corresponding evolution of the off-diagonal density matrix elements in red (projection of the Bloch vector onto the real axis: $\rho_{10} + \rho_{01}$). Note that the interactions at $\tau_{1,2,3}$ are not coincident with the pulse maxima to indicate that the interaction can take place at any time point within the pulse envelope. This is taken into account by the convolution of the response function with the three incident electric fields in Equation (2.52). We adapt the common way of writing the time intervals, by replacing $t_1 \rightarrow \tau$, $t_2 \rightarrow T$, and $t_3 \rightarrow t$, as well as the delay of the reference pulse (*vide infra*) by t_{LO} . The 2×2 matrices indicate which element of the density matrix is relevant for the macroscopic polarization of an exemplary two-level system during the respective time interval.

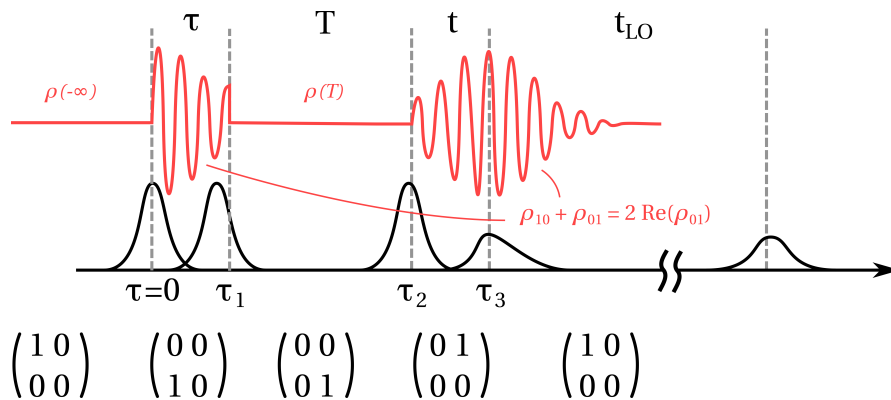


Figure 2.12 – (black) Pulse scheme of a photon echo experiment with (red) the projection of the Bloch vector onto the real axis as visualization of the density matrix. The 2×2 matrices indicate which element of the density matrix is relevant for the evolution of the density matrix during the time intervals τ , T , and t .

The first pulse creates a coherence between states $|0\rangle$ and $|1\rangle$, which is transferred into a population state by the second light-matter interaction after the coherence time delay τ . Though these two light-matter interactions also happen within a single laser pulse, the noncollinear experimental BOXCARs geometry (cf. Section 4.4) allows to detect only signals, which are

Chapter 2. Concepts in ultrafast spectroscopy

generated when each interaction is with a different laser pulse. Whenever the system does not interact with the electric field, it evolves according to the system Hamiltonian, i.e. it will undergo decoherence or population relaxation, or both. The third field interaction creates a coherence that radiates a signal field according to $E_s = iP^{(3)}$ in a phase matched direction $\mathbf{k}_s = \pm\mathbf{k}_1 \pm \mathbf{k}_2 + \mathbf{k}_3$. If this last coherence is phase conjugate to the initial coherence, the individual polarizations will rephase (R pathway) after a detection time $t = \tau$ and the observable signal, which is proportional to the macroscopic polarization, is maximized. This is referred to as a *photon echo*. If the second coherence is in-phase w.r.t. the first coherence instead, the polarizations will continue to dephase (NR pathway).

To extract its amplitude and phase information, the signal field E_{sig} is heterodyne detected via spectral interferometry with a time delayed reference pulse [43], called the local oscillator (LO). In the semi-impulsive limit (i.e. assuming δ -pulses) the convolution with the electric field disappears and the expression for the measured signal reads

$$I(\tau, T, \omega_t) \propto |E_{\text{sig}}(\tau, T, \omega_t) + E_{\text{LO}}(\tau, T, \omega_t)|^2 = |E_{\text{sig}}|^2 + |E_{\text{LO}}|^2 + 2 \text{Re} \{E_{\text{sig}}E_{\text{LO}}\}, \quad (2.76)$$

where the Fourier transform $t \rightarrow \omega_t$ has been carried out experimentally by detecting the spectrally resolved signal. $|E_s|^2$ is the homodyne signal, which is usually small and can be dismissed, and $|E_{\text{LO}}|^2$ is a slowly varying background that is removed from the total signal by background subtraction and Fourier analysis, cf. Section 4.8. The remaining interference term

$$E_{\text{sig}}E_{\text{LO}} \propto e^{-i(\mp\varphi_1 \pm \varphi_2 + \varphi_3 - \varphi_{\text{LO}})} \sum_n i R_n(\tau, T, t) \quad (2.77)$$

contains all the necessary information about the signal field and phase, and hence the system response, in form of its response function R . The phase term in Equation (2.77) contains the phases of all pulses, as well as the linear phase due to the delay between the signal and the LO, which is $\varphi_{\text{LO}} = \omega t_{\text{LO}}$. The latter can be subtracted by finding the correct LO time delay t_{LO} , and any residual phase is corrected for iteratively by comparing the integrated 2D spectrum to an auxiliary TA measurement, a procedure known as *phasing*, whose theoretical foundation is the projection-slice theorem.

2.5.2 The projection-slice theorem

The 2D spectrum $I_{2D}(\omega_\tau, T, \omega_t)$ is closely related to TA spectroscopy, as well as transient grating and photon echo techniques, since all probe the third-order nonlinear response of a system [44]. The projection-slice theorem [45] links the integral of the 2D spectrum over ω_τ to the TA signal, at each population time delay, via

$$I_{TA}(\omega_t, T) = \text{Re} \left\{ \frac{1}{2\pi} \omega_t E_{LO}(\omega_t) \int_0^\infty I_{2D}(\omega_\tau, T, \omega_t) d\omega_\tau \right\}. \quad (2.78)$$

Since the TA signal is unaffected by phase shifts of the pump- and probe pulses, the lineshapes of the transients are inherently absorptive and can be used to eliminate distortions in the 2D spectrum [44] that are due to an inaccurate determination of the LO delay or any residual phase of the laser pulses, cf. Equation (2.77). Multiplication of the complex 2D signal with a phase correction function

$$\varphi(\omega_t) = e^{i\varphi_c + i(\omega_t - \omega_0)t_c}, \quad (2.79)$$

which introduces a constant phase correction φ_c and a linear timing correction t_c [46], and iteratively searching for the parameters that minimize the difference between the projected 2D spectrum and the auxiliary TA spectrum yields the absorptive and refractive components as real and imaginary components of the complex 2D data. It is possible to add a quadratic correction term to Equation (2.79) to account for higher order phase errors [47] that could for example be due to a residual nonlinear phase, due to improper spectral calibration of the detector. However, interferometric determination of the residual nonlinear phase and subsequent correction [48] is preferable to including the quadratic term into the iterative phase correction process.

2.5.3 Wavepackets and their description using response functions

Whenever the bandwidth of a Fourier-limited excitation pulse exceeds the energy separation of vibrational- or electronic levels of a system it can create vibrational- or electronic wavepackets. While vibrational wavepackets can be created on the excited- or on the ground electronic

Chapter 2. Concepts in ultrafast spectroscopy

state, electronic wavepackets are coherent superposition of excited electronic states. Typically, electronic degrees of freedom (DOFs) couple to a large number of nuclear/vibrational DOFs, leading to a rapid dephasing of any electronic coherences within a few 10s of femtoseconds. A vibrational coherence on the other hand is (by first approximation) decoupled from other modes of the system and its dephasing time can range from 10s of femtoseconds to 10s of picoseconds, depending on the system [49]. Due to these considerations, vibrational coherences are observed much more frequently in femtosecond spectroscopy than electronic coherences.

Vibrational coherences can be *field-driven*, when the excitation creates a superposition of vibrational levels, or *reaction-driven*, if the coherence is created by the instantaneous deformation of a reaction coordinate [50, 51]. They are of importance for fundamental processes in physical chemistry, since they often contribute to a certain relaxation channel, through vibronic coupling [30, 52–59], i.e. when their frequency is resonant to a transition. E.g. a spin-vibronic mechanism can be responsible for an efficient intersystem crossing via so-called *coupling modes* of the system [60], however these are not necessarily associated with a significant displacement between the ground and excited state geometry and are thus hard to observe in optical spectroscopy [61]. *Tuning modes* on the other hand are responsible for the large structural distortions and thus dominate the spectral signature [61].

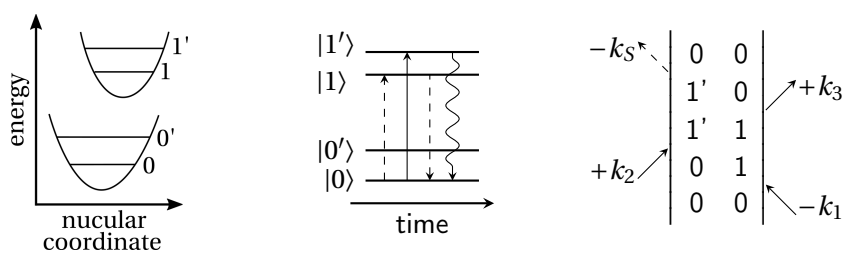


Figure 2.13 – (left) The displaced oscillator model. (middle) Ladder- and (right) Feynman diagram description of a vibrational coherence on the excited electronic state during the population time. In this example, the detection frequency is greater than the excitation frequency by one quantum of the vibrational mode, leading to an off-diagonal signal in the 2D spectrum.

Figure 2.13 exemplifies the concept of vibrational wavepackets using ladder- and vertical Feynman diagrams for a vibronic system of displaced oscillators. In such a system, the ground- and excited electronic states possess vibrational levels, which modify the optical properties

of the system. Contrary to the previous examples of response functions, the displaced oscillator system can evolve as a coherent superposition of vibrational levels ($|0'\rangle\langle 0|$ or $|1'\rangle\langle 1|$, or complex conjugate) during the population time interval. This leads to a periodic modulation of the observed signal, with a frequency Ω_T that equals the energy gap between the vibrational levels, i.e. the frequency of the vibrational mode.

Similarly to the $|1'\rangle\langle 1|$ vibrational coherence, the coherent superposition of excited electronic states $|n\rangle\langle m|$ would lead to a modulation of the signal with the frequency $\Omega_T = 2J$, where J is the resonance coupling between the electronic states of the superposition. The excitation- and detection frequency dependence of the observed modulations of the 2D signal can reveal the origin of the underlying coherences [62–64] and typically the distinction is made by explicitly considering all response functions of model systems that oscillate in T with a certain Ω_T . Model systems include the previously mentioned displaced oscillator and electronic dimer model, but also variations and combinations thereof, such as a vibronic dimer [65].

2.5.4 Signals and information in 2D spectroscopy

The observable signals in 2D spectroscopy can be grouped into kinetics, describing the energy relaxation pathways of the system, and dynamics, which reflect the structural response of a system upon excitation. The following paragraphs will give an overview of some common features in 2D spectra and the microscopic information that can be obtained from them.

2.5.5 Kinetics and relaxation pathways

The 2D spectrum and its population time evolution reveals two spectroscopic observables that cannot be obtained using TA spectroscopy, namely the 2D lineshape and cross peaks.

(i) The **2D lineshape** at early population times is inhomogeneously broadened in the diagonal-, but homogeneously broadened in the anti-diagonal direction of the 2D spectrum, which is shown in Figure 2.14. The broadening of the 2D lineshape in the anti-diagonal direction with increasing population time is directly related to the loss of correlation between excitation- and emission frequencies, which is caused by **spectral diffusion** of the ensemble systems, as described by the frequency-frequency correlation function (FFCF) [66]. E.g. in a solute-solvent

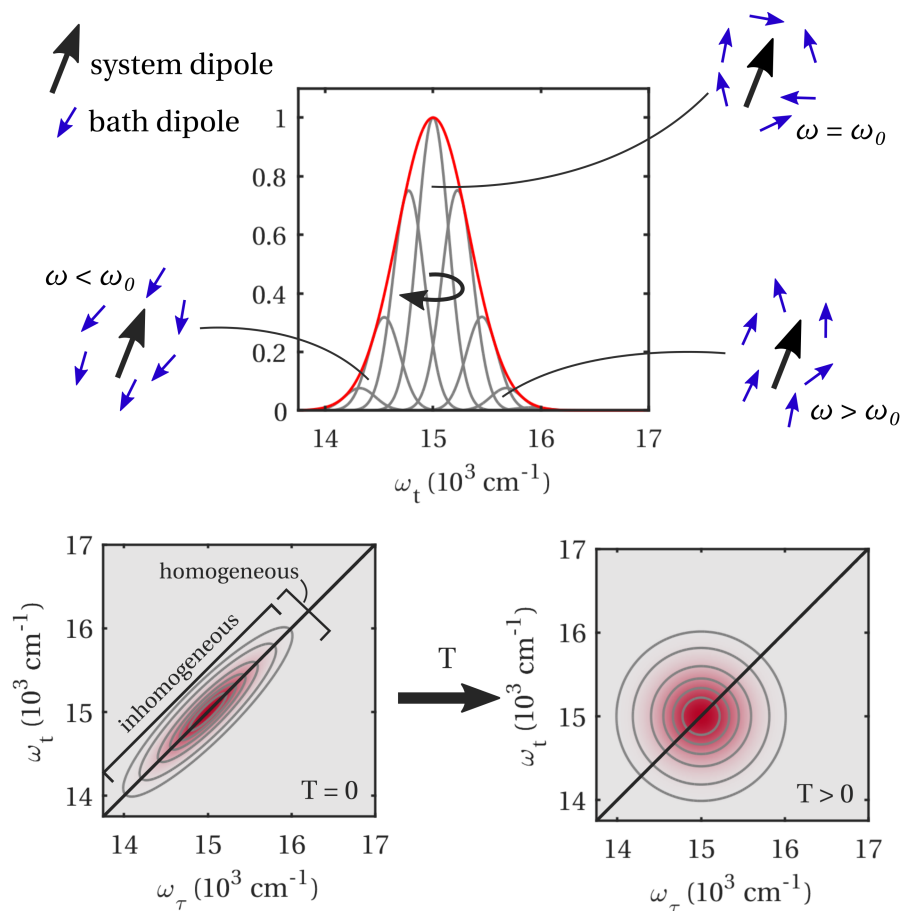


Figure 2.14 – (top) Spectral diffusion, described here by the effect of the solvent dipole orientation on the frequency of the solute dipole, leads to the loss of correlation between excitation- and detection frequency, resulting in a (bottom) broadening of the 2D lineshape along the anti-diagonal direction with increasing population time.

system a change in transition energy can be caused by the fluctuation solvent shell. This is observed as follows (from ref. [67]): During the first coherence molecules are labeled with the frequency $\omega(0)$. Dynamical changes of the solvent lead to spectral diffusion, which changes the frequency of each molecule. After a time delay T the new frequency is read out by the second coherence. This correlation between label- and readout frequencies is the FFCF

$$C(t) = \langle \delta\omega(T)\delta\omega(0) \rangle \quad (2.80)$$

and is encoded in the 2D spectrum, e.g. in form of the center line slope [66, 68, 69].

2.5. Coherent multidimensional spectroscopy

(ii) In general, **off-diagonal peaks** in a 2D spectrum reveal couplings between different states of a system. Their population time evolution allows to discern different scenarios that would result in the observation of a cross peak. (a) If two states are **coupled via a common ground state**, excitation of either state will also bleach the other. This implies that both, the on-diagonal and off-diagonal peaks, are present at $T = 0$. This is the case for electronic dimers, where two excited states of the system possess the same ground state, or vibronic systems, in which the excitation is from the ground state to two vibrational levels of the same electronic excited state. (b) In a multichromophoric system the ground state is commonly not shared between the molecules and thus excitation of one chromophore will not affect the optical properties of another chromophore. **Chemical exchange, structural transformations, or population transfer** between chromophores during the population time leads to an increase of cross peak intensity that can be associated to the forward- and backward-reaction constants k_{AB} and k_{BA} of the reaction mechanism $A \rightleftharpoons B$. The forward- and backward-reactions can be differentiated, based on which cross peak is observed, as illustrated in Figure 2.15. Since population transfer is energetically downhill in most cases with $k_{BA} > k_{AB}$ the cross peak below the diagonal is typically more intense.

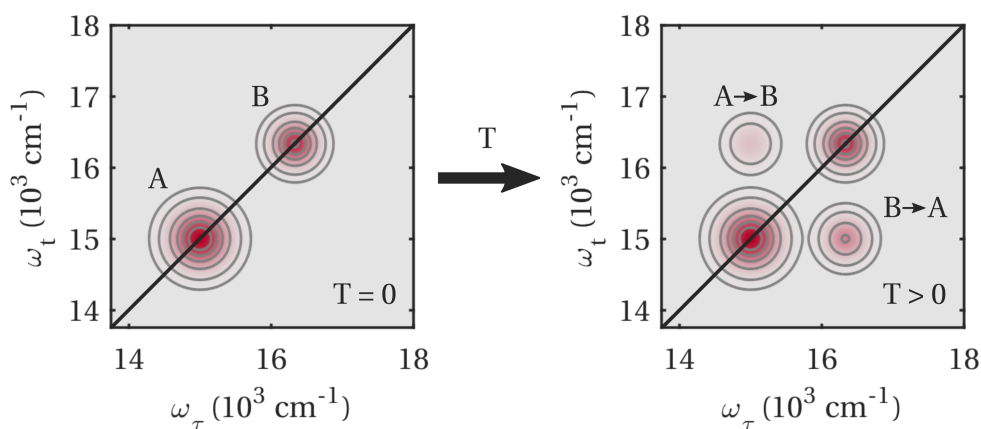


Figure 2.15 – Chemical exchange, structural transformations, or population transfer between chromophores is observed via the formation of cross-peaks in 2D spectra.

(iii) Besides the processes described in (i) and (ii), a 2D spectrum will often show overlapping ESA to a higher-lying excited state and red-shifted SE components. An illustrative spectrum of a displaced oscillator (DO) is shown in Figure 2.16, in which the vibrational energy gap

Chapter 2. Concepts in ultrafast spectroscopy

is indicated by the dashed horizontal and vertical lines. The two diagonal- and cross peaks originate from bleached transition from a common ground state, while the SE is red-shifted by one vibrational quantum (dashed horizontal line at $\omega_t = 14300 \text{ cm}^{-1}$). In this example the ESA is found as a negative signal at $\omega_t > 16500 \text{ cm}^{-1}$, though its spectral position generally depends on the electronic landscape of the system.

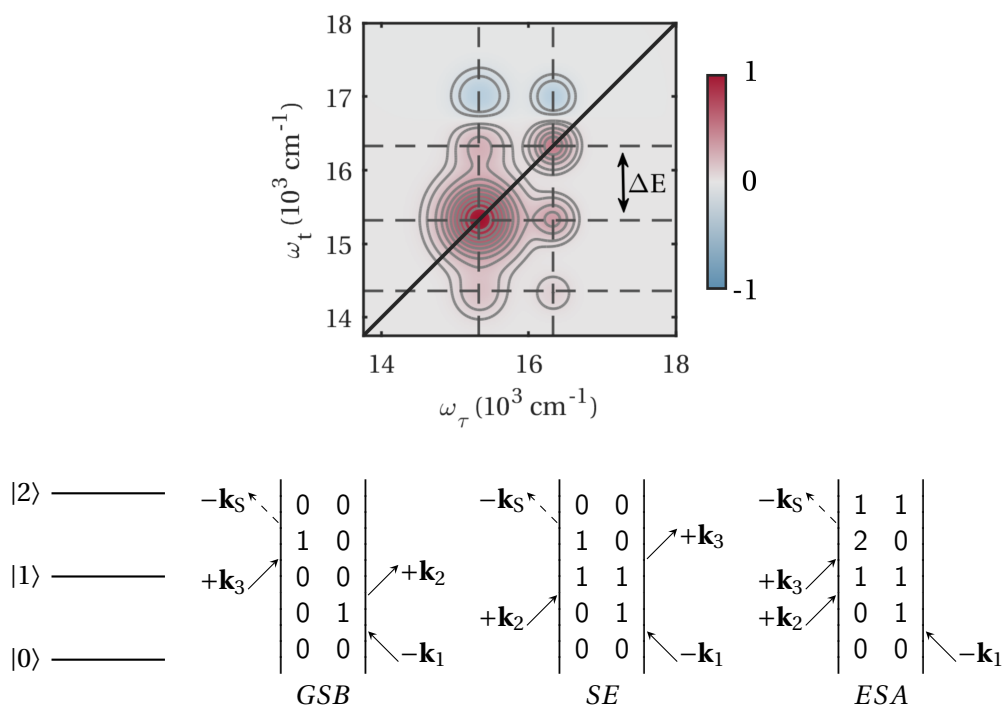


Figure 2.16 – (top) Illustrative 2D spectrum of a displaced oscillator showing a characteristic pattern of GSB and SE features. ESA to a higher lying electronic state appears as a negative signal at $\omega_t > 16750 \text{ cm}^{-1}$. (bottom) Double sided Feynman diagrams for a 3-level system. In a TA experiment the first two (\mathbf{k}_1 and \mathbf{k}_2) light-matter interactions occur within the same laser pulse and the observed signal corresponds to the integration of the 2D spectrum over the frequency range $\Delta\omega_\tau$, which corresponds to the spectral width of the excitation pulse. The dependence of the photon echo on the temporal delay between \mathbf{k}_1 and \mathbf{k}_2 is exploited in 2D spectroscopy to resolve the excitation dependence of the transient signal.

2.5.6 Coherences and wavepackets

2D spectroscopy has proved to be a powerful technique when it comes to disentangling and identifying the origin of electronic- and vibrational coherences [53, 62–65, 70–76]. Conceptually, the analysis is carried out by (i) writing out all response functions that are in a coherence

2.5. Coherent multidimensional spectroscopy

$|n\rangle\langle m|$ during the population time for a model system (DO, ED, etc.), (ii) grouping them in R and NR contributions, and (iii) visualizing them as R and NR *2D beating patterns*, ordered by their excitation- and detection frequencies (see e.g. ref. [63]). These beating patterns are shown in Figure 2.17 for a DO and ED system and can be compared qualitatively to the R and NR 2D beating spectra that are (iv) obtained by applying the Fourier transform $T \rightarrow \Omega_T$ to the residuals of the R and NR 2D spectra.

The response functions can be (v) further disentangled, since they evolve with conjugate frequencies during the population time, e.g. as $|n\rangle\langle m|$ or $|m\rangle\langle n|$, where $|n\rangle$ and $|m\rangle$ are vibrational levels on an electronic state in the DO model, or different electronic states of the ED. This procedure is outlined and applied to the description of quantum dots in ref. [74]. (vi) A

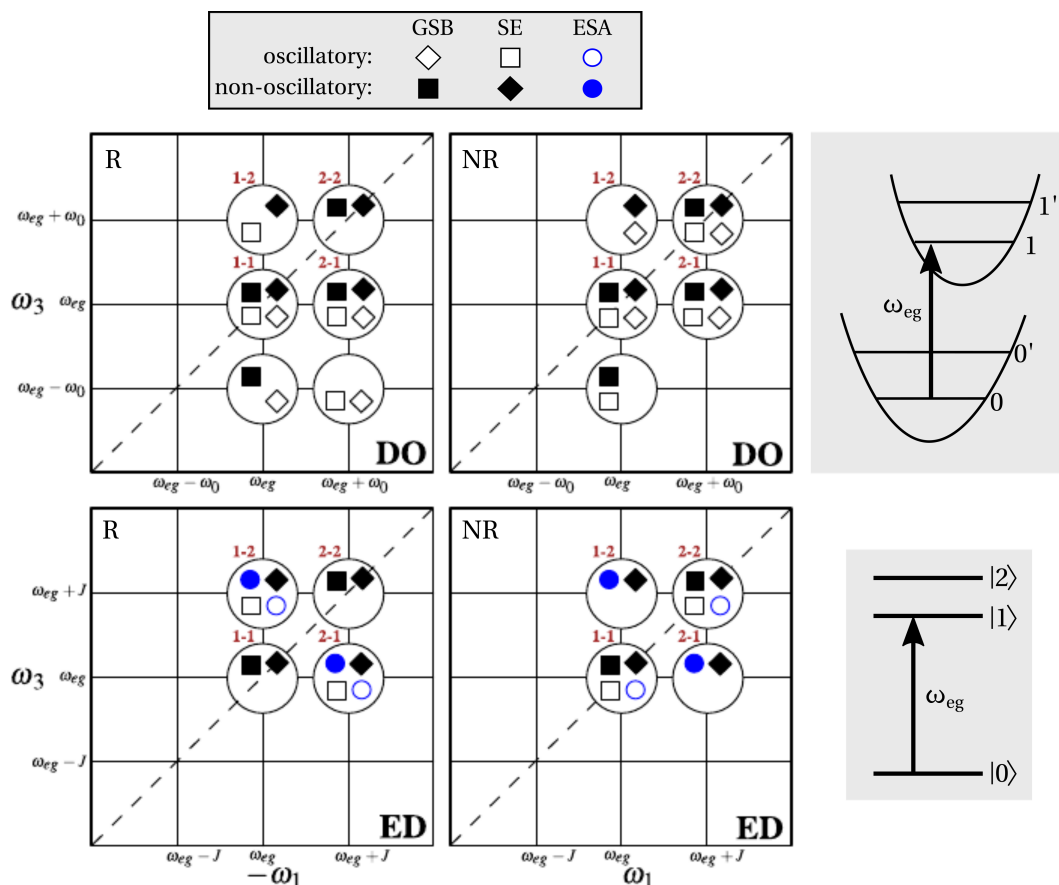


Figure 2.17 – Overview of the R and NR 2D beating patterns observed for (top row) a displaced oscillator and (bottom row) an electronic dimer. Reprinted from ref. [63], copyright 2012, with permission from Elsevier. Grey boxes have been added for the purpose of this thesis to illustrate the different model systems.

Chapter 2. Concepts in ultrafast spectroscopy

complex Fourier transform $T \rightarrow \Omega_T$ of the R and NR 2D data yields the beating maps at $\pm\Omega_T$, which can as well be compared qualitatively to the 2D maps obtained in step (iv).

It is worth mentioning that the coherence analysis described in this chapter relies on the complex 2D data, but is not strongly affected by inaccuracies of the signal phase, since the relevant information is contained in the absolute valued beating maps and not the phase. It is thus more robust than e.g. analyzing the initial phases of a temporal signal that could as well be used to differentiate between ground- and excited state coherences.

3 Methods in transient absorption spectroscopy

3.1 Overview of the transient absorption setup

The transient absorption setup shown in Figure 3.1 uses 800 nm pulses at 1 kHz repetition rate with a pulse duration of appr. 100 fs from a Spectra-Physics Tsunami oscillator and Spitfire amplifier. The 600 mW output power is split into a pump- and a probe branch by a 90/10 (T/R) beam splitter. A narrowband (bandwidth: 10-20 nm), 0.1-5 mW, visible pump pulse is created using a home-built noncollinear optical parametric amplifier (NOPA) and compressed to 25-35 fs by a folded prism compressor. It is modulated by a mechanical chopper that blocks every other laser shot to allow for difference detection. The pulse duration is determined by second harmonic generation (SHG) FROG. The probe laser pulse is delayed by an optical delay line (Thorlabs LTS) and focused by a 75 mm focal length lens into a 5 mm thick CaF₂ crystal to generate the broadband probe spectrum via self-phase modulation (SPM). The CaF₂ is continuously moved up and down to avoid unstable white light generation due to degradation of the crystal. The pump- and probe beams are overlapped at the sample position in such a way that the size of the pump focus is roughly three times the size of the probe, to allow for homogeneous excitation across the entire probe beam profile. The probe beam is then refocused into a multimode optical fiber, which is coupled to the entrance of a grating spectrograph. The dispersed white light spectrum is recorded shot-to-shot by a home-built CMOS detector and the data acquisition software calculates the difference between the pumped- and unpumped probe spectrum according to Equation (3.5).

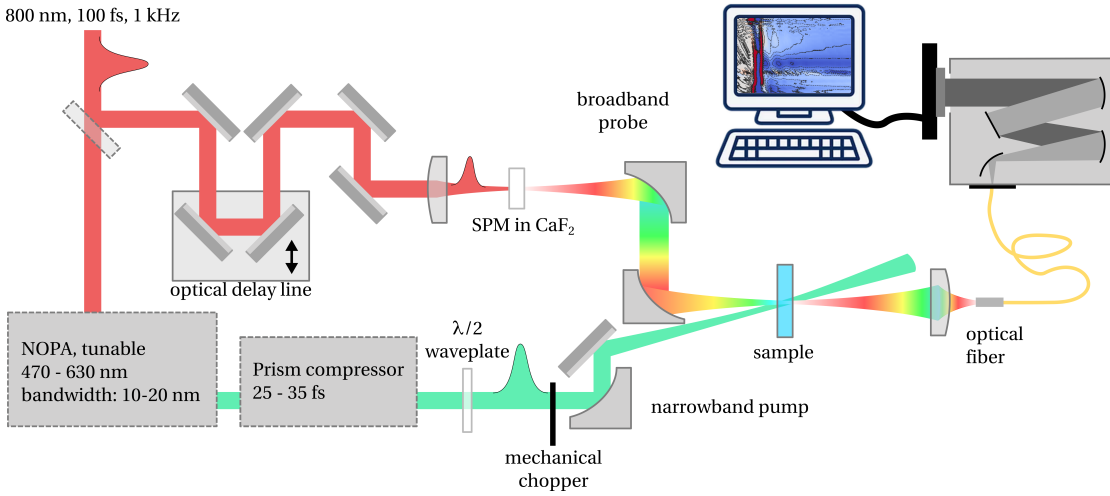


Figure 3.1 – Overview of the 1 kHz setup.

3.1.1 Excitation pulse generation

A home-built NOPA, Figure 3.2 is used to generate narrowband excitation pulses in the range 470-630 nm. Briefly, the fundamental laser beam is split by a 80/20 (T/R) beam splitter and the transmitted pulse is used to generate a 400 nm pump-pulse via SHG inside a BBO crystal. This pump beam is focused loosely in front of a 5 mm thick BBO crystal in which it undergoes spontaneous parametric down-conversion [77, 78], in which a high energy pump photon with \mathbf{k}_{pump} and ω_{pump} is split into two photons of lower energy with ω_{signal} and ω_{idler} according to

$$\mathbf{k}_{\text{pump}} = \mathbf{k}_{\text{signal}} + \mathbf{k}_{\text{idler}} \quad \text{and} \quad \omega_{\text{pump}} = \omega_{\text{signal}} + \omega_{\text{idler}} \quad (3.1)$$

The signal and idler pulses are emitted in the phase matched directions $\mathbf{k}_{\text{signal}}$ and $\mathbf{k}_{\text{idler}}$. Temporal broadening due to the group velocity mismatch between the signal and idler is avoided in the noncollinear geometry, since the group velocity of the idler projected onto the propagation direction of the signals equals the group velocity of the signal [77], which is illustrated in Figure 3.3 and quantified by

$$v_{g,\text{idler}} \cos(\Omega) = v_{g,\text{signal}}, \quad (3.2)$$

where $v_{g,\text{idler}}$ and $v_{g,\text{signal}}$ are the group velocities of the signal and the idler, and Ω is the internal angle between them.

3.1. Overview of the transient absorption setup

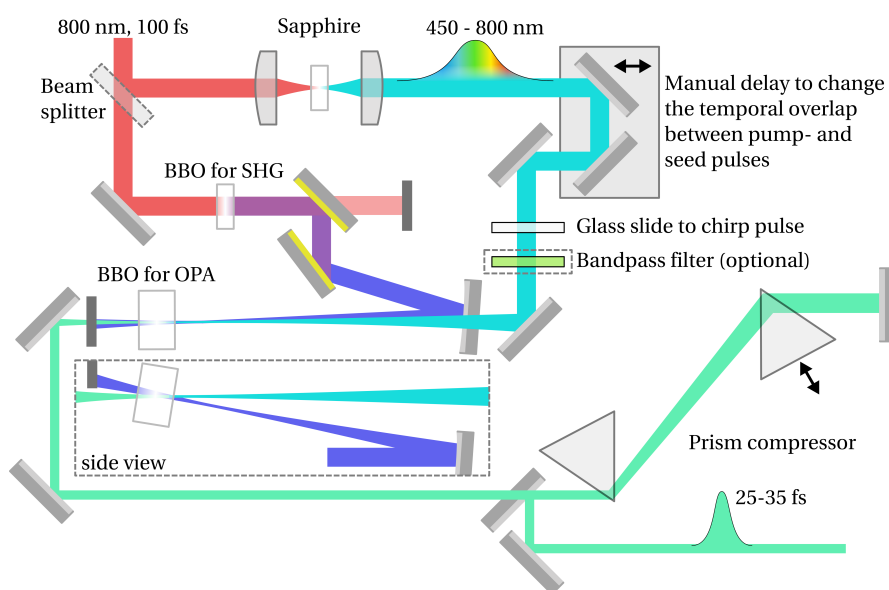


Figure 3.2 – Schematic overview of the NOPA and folded prism compressor.

The pulse reflected by the 80/20 (T/R) beam splitter is used to generate a white light seed pulse via self-phase modulation (SPM) inside a sapphire crystal. The seed is temporally chirped by inserting a glass slide and spatially overlapped with the pump pulse inside the BBO. The desired wavelength can be selected by adjusting the temporal delay of the chirped seed pulse w.r.t. the pump pulse. I.e. depending on the spectral component of the seed that is temporally coincident with the pump pulse, a different wavelength is amplified by the NOPA. Using a bandpass filter to pre-select the desired wavelength of the seed beam facilitates the alignment of the NOPA and improves the quality of the output beam, since no undesired spectral components are amplified and need to be removed by correcting the alignment of the NOPA or by spectral filtering in the Fourier plane of the prism compressor.

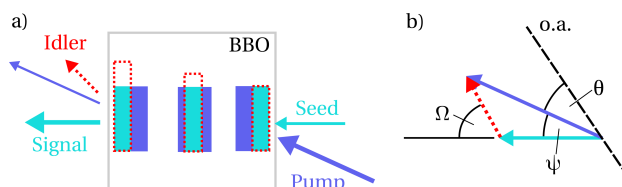


Figure 3.3 – (a) The (projected) group velocities of the idler and signal are matched in the noncollinear geometry. After refs. [77] and [79]. (b) Internal angles between signal, idler, and pump for noncollinear phase matching. o.a. is the optic axis of the nonlinear crystal.

3.1.2 Prism compressor

Angular dispersion, as introduced by a refractive optical element, leads to a negative group-velocity dispersion, which was first shown by Martinez, Gordon, and Fork in a series of seminal publications [80–83]. This can be shown by considering the generalized spectral transfer function (cf. with Equation (2.6))

$$\phi(\omega) = \frac{\omega}{c} P(\omega) = n_2 l \cos \theta, \quad (3.3)$$

where $P(\omega)$ is the frequency-dependent optical path length, c the speed of light, ω the frequency of the electric field, n_2 the refractive index of the medium, l the distance between two (so far arbitrary) points A and B, and θ the angle of refraction. The second derivative of Equation (3.3) yields an expression for the total GVD of the optical system

$$\frac{d^2\phi}{d\omega^2} = \frac{\lambda^3}{2\pi c^2} \frac{d^2P}{d\lambda^2}. \quad (3.4)$$

Since P depends on $n(\lambda)$ and $\theta(\lambda)$, its second derivative is a complex expression that depends on the optical system. It can be shown [82] that that angular dispersion necessarily introduces negative GVD. However, since the positive GVD introduced by the material dispersion $\frac{d^2 n_2}{d\lambda^2}$ is greater than negative GVD from angular dispersion $\left(\frac{d\theta}{d\lambda}\right)^2$ by roughly two orders of

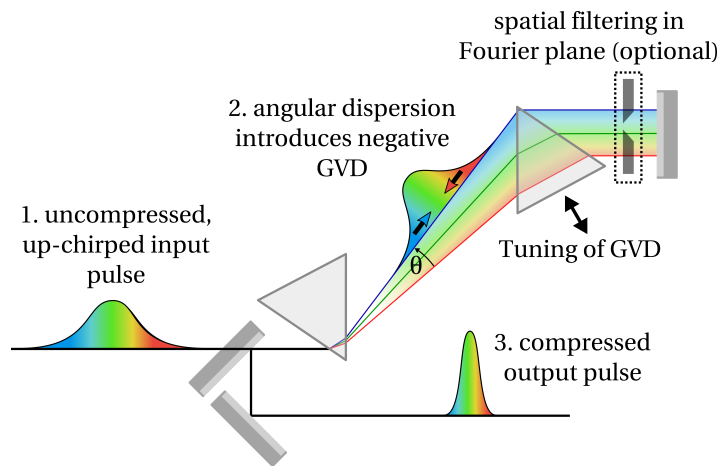


Figure 3.4 – Working principle of a prism compressor. The up-chirped input pulse experiences negative GVD, due to angular dispersion. Passing through four prisms in a folded geometry removes additional spatio-temporal distortions that have been introduced by the first prism.

3.1. Overview of the transient absorption setup

magnitude, the angular dispersion inside a medium cannot be exploited for pulse compression. Instead, the working principle of a prism compressor is that the angular dispersion after a prism (i.e. the angularly dispersed beam propagates in air rather than inside a material) is used to introduce negative GVD. Finding a solution for the second derivative of the optical path length $\frac{d^2P}{d\lambda^2}$ for an optical system of two Brewster-angle prisms, as done by Fork et al. [83], allows to calculate the negative dispersion and find the correct distances between the optical elements to compress a laser pulse. Software solutions like Lab2 [84] exist to calculate these distances for given experimental conditions. To adjust the negative dispersion of the prism compressor the second prism can be translated in and out, cf. Figure 3.4. Prisms 2 to 4 are required to correct the spatio-temporal distortions introduced by the angular dispersion [85].

3.1.3 White light generation via self-phase modulation in CaF₂

The white light probe pulse generated via SPM inside a 5 mm CaF₂ crystal is shown in Figure 3.5. In a first step the 800 nm pulse is focused behind the CaF₂ crystal using a lens with a focal length of appr. 75 mm. Moving the lens away from the crystal shifts the focus closer to the crystal. At a certain distance the threshold for filamentation and white light generation is reached, and the distance of the lens is adjusted further until a broad and stable white light can be observed. We find that the perfect alignment through the optics, i.e. when the beam is centered on the focusing lens and its angle of incidence is normal to the surface of the CaF₂ crystal, does not always result in the most stable white light generation. Changing the tip

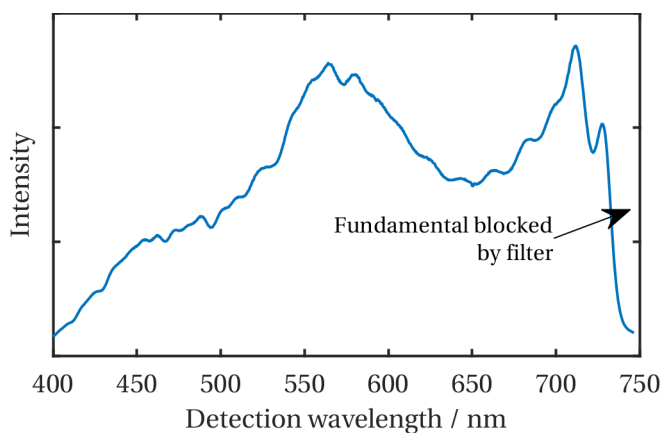


Figure 3.5 – White light spectrum generated via self-phase modulation inside CaF₂.

and tilt of the last steering mirror before the focusing lens, usually improves the stability significantly, which is likely due to imperfect spatial beam properties of the fundamental. The filament inside the CaF₂ crystal, i.e. the source of the white light beam, is subsequently imaged onto the sample and then onto the entrance of a multimode fiber, which couples it to the spectrograph. When adjusting the white light generation we typically leave the position of the CaF₂ crystal unchanged to not disturb the imaging between the CaF₂ crystal, the sample position, and the fiber entrance.

3.1.4 Pump-probe measurements and data acquisition

Transient spectra are acquired using a shot-to-shot detection scheme. The data acquisition software measures N shots of the white light spectrum and every second excitation pulse is blocked by a mechanical chopper (Thorlabs MC2000B-EC). The software calculates the change in optical density of the sample by taking the difference of the pumped- and unpumped acquisitions and dividing the result by the unpumped spectrum according to

$$\Delta OD = -\log\left(\frac{I}{I_0}\right)_p - \log\left(\frac{I}{I_0}\right)_u = -\log\left(\frac{I_p}{I_u}\right) \approx \frac{1}{\ln 10} \frac{I_p - I_u}{I_u}. \quad (3.5)$$

Typically 1000 to 2000 laser shots are acquired to obtain a good signal-to-noise ratio and the setup is sensitive enough to measure difference signals of appr. 1 mOD. Transient spectra are recorded for time delays in the range from -5 ps to 1000 ps by scanning the optical delay line. The entire measurement is repeated at least 20 times to obtain a good data quality, and up to 100 times for small signals and to measure temporal oscillation of the transient signal.

3.1.5 Magic angle and anisotropy measurements

To cancel out signal contributions that are due to rotational diffusion of the molecules the relative polarization angle between the pump- and probe pulse is set to the ‘magic angle’ (MA) at approx. 54.74°. From an experimental point of view, it is advantageous to rotate the polarization of the pump pulse to avoid artifacts caused by the polarization dependent optics of the detection system. Rotating the polarization of the fundamental beam before the white light generation instead would change the probe spectrum, as well as the detection efficiency,

3.1. Overview of the transient absorption setup

since the spectral efficiency of the grating inside the spectrometer is polarization dependent. The last concern can partly be dismissed, if the polarization of the probe pulse is scrambled after the sample, e.g. by using a multimode fiber to guide the light to the spectrometer. Measuring the frequency- and time-dependent anisotropy $r(\omega, t)$ of a transient signal reveals information about the angle between the excited- and probed transition dipole moments, cf. Sec. 2.4.3. Experimentally this involves measuring the parallel- (I_{\parallel}) and perpendicular (I_{\perp}) components of the signal and calculating the anisotropy as

$$r(\omega, t) = \frac{I_{\parallel}(\omega, t) - I_{\perp}(\omega, t)}{I_{\parallel}(\omega, t) + 2I_{\perp}(\omega, t)}. \quad (3.6)$$

In our case, measuring the anisotropy involves three separate measurements: TA with (i) parallel- and (ii) perpendicular relative polarizations to calculate the anisotropy, and at (iii) MA polarization to compare the calculated MA signal

$$\text{MA} = \frac{1}{3}(I_{\parallel} + 2I_{\perp}) \quad (3.7)$$

to the measured MA signal, which is shown in Figure 3.6. Step (iii) is solely to ensure the credibility of the measurement. An additional factor may be required, if the signal intensity has changed between the measurements with parallel and perpendicular relative polarizations, the the MA measurement, due to e.g. a change in excitation pulse energy.

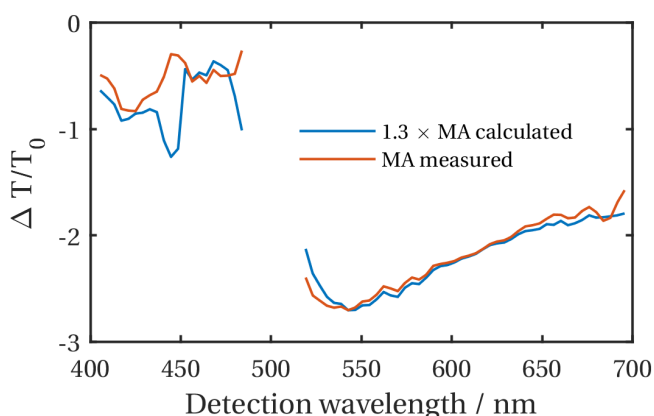


Figure 3.6 – Comparison between the measured and calculated transient MA spectrum of $[\text{Pt}(\text{ppy})(\mu\text{-tBu}_2\text{pz})]_2$. The calculated spectrum is rescaled to account for the difference in pulse energy between the measurements, but its spectral shape agrees well with the measured transient MA spectrum. The pump wavelength region is excluded due to scatter.

4 Development and characterization of the 2D photon echo setup

This chapter gives an overview of the experimental methods used in 2D Fourier transform spectroscopy. Since a large part of my work involved building and improving the 2D photon echo setup, it can be considered as a presentation of the results of my thesis. Only the way we split and delay the laser pulses has not been adapted from a previous version of the experimental setup [86].

4.1 Overview of the 2D photon echo setup

Figure 4.1 shows an overview of the 2DPE experiment. Briefly, the amplified laser pulses (800 nm, 3 kHz, 30 fs) are attenuated to 300 μJ , using the combination of a $\lambda/2$ waveplate and a transmission polarizer, before they are focused and coupled into an approx. 1.5 m long, argon-filled and differentially pumped (0.5 - 1 bar at the exit and < 10 mbar at the entrance) hollow core fiber (HCF) with an inner diameter of 260 μm . The focal spot size can be adjusted by closing or opening an iris located before the focusing mirror. The resulting white light spectrum spans from 450 to 950 nm and the pulse energy exceeds 180 μJ – 60 to 70% transmission through the HCF. Its temporal chirp is compensated by a set of double-angle chirped mirrors (CMs, Ultrafast Innovations, PC70) and fine-tuning of the phase is achieved by changing the optical path through a pair of thin fused silica (suprasil) wedges (OA924 FemtoOptics). The beam is then split into four replicas in the BOXCARS geometry by a combination of beam splitters and mirrors, as shown in Figure 4.6, which are mounted

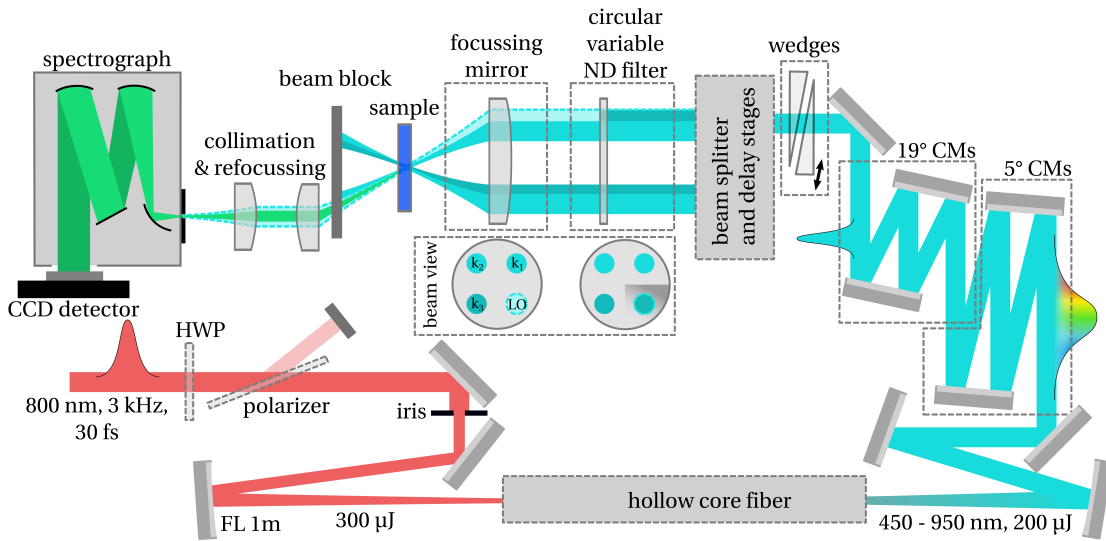


Figure 4.1 – Schematic overview of the 2D experiment.

on stable, home-built aluminium mounts to achieve a passive phase stability of approx. $\lambda/60$ at 540 nm. A 50.8 mm curved mirror with a focal length of 300, 500, or 1000 mm at normal incidence focuses all four beams to a common focal point with a diameter of 200 to 600 μm (depending on the focal length) inside the sample. Long focal lengths are chosen to reduced the angle between focused beams in order to avoid signal distortions due to spatial filtering [87]. The LO is attenuated by a factor of 10^3 to 10^4 and $\mathbf{k}_1 - \mathbf{k}_3$ are delayed w.r.t. \mathbf{k}_{LO} by passing them through a 1 mm fused silica plate (not shown in Figure 4.1). The signal and LO copropagate after the sample and are collimated and refocused onto the entrance slit of a spectrometer (Andor Shamrock 303i), and their spectral interference is recorded using a home-built CCD (Hamamatsu S11155-2048-02) detector in combination with a field-programmable gate array (FPGA) integrated circuit for fast readout. All data processing is performed in LabView.

4.2 White light generation using hollow-core fibers

Since the experiment requires white light pulses with relatively high energies, white light generation from crystals or optical fibers cannot be used. Instead, the white light pulse is generated inside an argon-filled HCF, a technique [88, 89] first implemented in attosecond experiments [6, 90–92]. The fibers used in our laboratory typically have an inner diameter of appr. 260 μm and a length between 1 and 1.5 m. To couple the 800 nm pulse efficiently

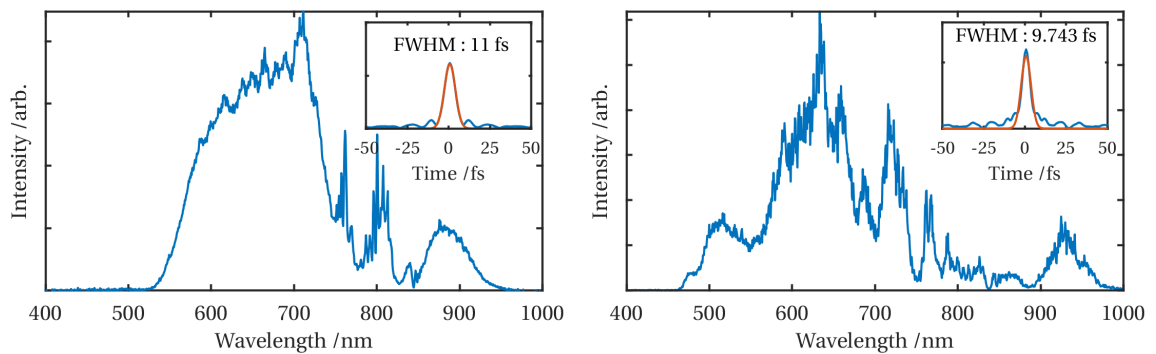


Figure 4.2 – White light spectra from SPM inside an argon-filled HCF and Fourier transforms of the spectra (insets) on different days and under different experimental conditions.

into the HCF the focus of the fundamental beam needs to match the fiber's lowest loss EH_{11} hybrid mode [88, 93]. This condition is satisfied when the $1/e^2$ radius of the laser focus is 0.65 times the inner radius of the fiber [88, 91, 94]. A concave mirror with a focal length of 1 m is used to focus the fundamental beam onto the HCF entrance and the focus size is adjusted by closing an iris before the focusing optic. If the focus is too tight, higher order radial modes in the white light beam profile are observed and typically the iris is closed to appr. 1 cm to obtain a smooth TEM_{00} white light mode. The transmission through the fiber is between 60 and 70 % at a pressure of 0.5 to 1 bar and the spectrum spans from 450 to 950 nm, as shown in Figure 4.2. Between 500 and 750 nm it is quite homogeneous, but spectral regions outside this window show significant modulations, which would pose problems in a Fourier transform technique. These wavelength regions are however not relevant for the experiment. The spectra in Figure 4.2 differ quite significantly, which is due to the fact that the experimental conditions (pulse energy, in-coupling, input and exit pressure, fiber alignment, etc.) have changed. However, on a day-to-day basis, i.e. with minimal changes of the experimental conditions, the white light spectrum from the HCF is reproducible.

4.3 Chirped mirror compressor

Chirped mirrors (CMs) are specially designed dielectric mirrors with a defined spectral transfer function. They can be engineered to compensate the phase accumulated by a laser pulse during a nonlinear optical process, such as SPM inside a HCF, nonlinear crystal or optical fiber, or from a noncollinear optical parametric amplifier. A stack of high- and low refractive index

Chapter 4. Development and characterization of the 2D photon echo setup

materials, designed such that the thickness is $1/4$ of the Bragg wavelength, is used to reflect an incident laser beam and interferences at the discontinuities add up constructively at the Bragg wavelength λ_b . Thickness variations of the layers results in varying penetration depth for different wavelengths. This is illustrated in Figure 4.3.

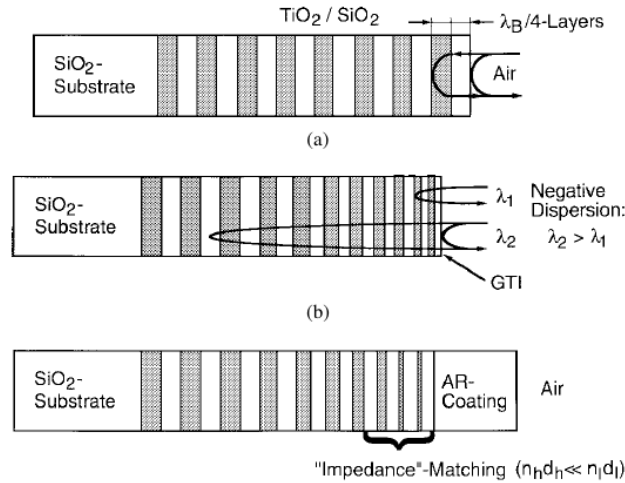


Figure 4.3 – (a) A dielectric quarter-wave Bragg mirror can be used as a highly reflective element. (b) If the Bragg wavelength is increased with each layer, longer wavelength penetrate deeper into the substrate, leading negative GDD. (c) Oscillations of the GDD can be reduced by impedance-matching and anti-reflection coating of the mirror. Reprinted, with permission, from ref. [95], copyright 1998 IEEE.

Each CM has a fixed, negative GDD and increasing the number of reflections increases the total amount of GDD experience by the laser pulse. Strong distortions of the laser pulses can arise due to spectral oscillations of the GDD, which can be compensated using complementary mirrors pairs. However, inaccuracies between different coating runs lead to residual GDD oscillations, i.e. the GDD oscillations of a complementary mirror pair does not cancel out perfectly. By using two mirrors from the same coating run at different angles the mismatch between the coatings and thus the residual oscillations of the GDD (of each pair) become negligible small and these double-angle CMs are nowadays commonly used to achieve sub-15 fs pulse duration in the visible. Figure 4.4 shows a typical spectrogram of a 12 to 14 fs laser pulse, measured by transient grating FROG. We noticed during the commissioning that the weak interference patterns at ± 30 fs are enhanced, if the spectrograph is misaligned. In those cases the spectrogram looked comparable to the one of a pulse modulated by a sine function, shown in Figure 2.2 (bottom left).

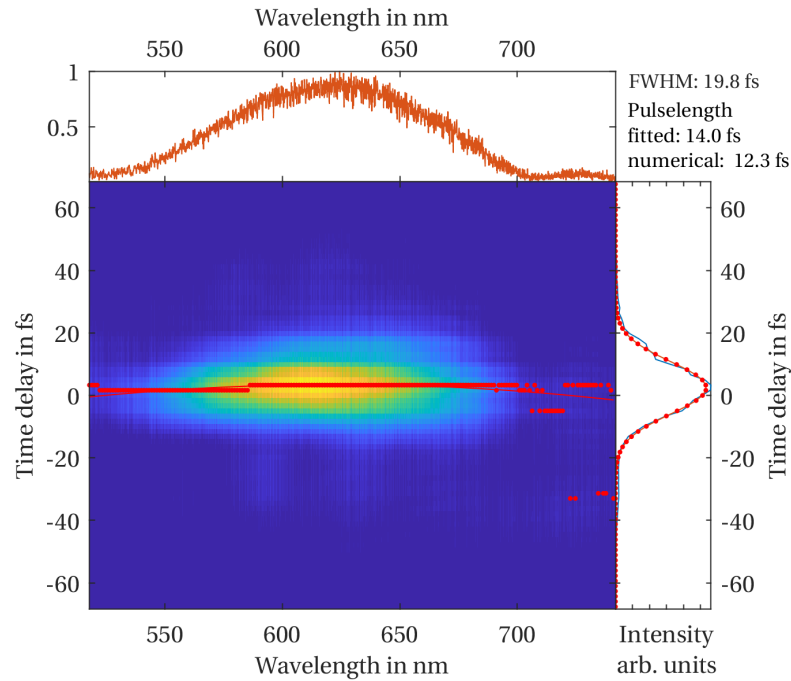


Figure 4.4 – Spectrogram of the broadband laser pulse measured by transient grating FROG. The top and left panels show the integration onto the wavelength and time axis, respectively.

4.4 The noncollinear photon echo interferometer

The three noncollinear excitation beams are arranged in the so called BOXCARS geometry to fulfill the phase matching conditions for the photon echo signal [44, 96, 97]. Beams \mathbf{k}_1 - \mathbf{k}_3 are located on three corners of a square, when looking along the beam direction (the z-axis). They are focused into the sample using a 50.8 mm concave, spherical mirror at normal incidence with a focal length of 300, 500 or 1000 mm and the signal is emitted in the direction of the fourth corner of the square, collinear to the local oscillator beam path, as illustrated in Figure 4.5 a). \mathbf{k}_1 - \mathbf{k}_3 are blocked by an aperture and the signal and LO are imaged onto the entrance slit of the spectrograph.

To split the beams and delay the laser pulses we use a compact setup based on metal-coated, 1 mm thick beam splitters and optical delay stages that is shown in Figure 4.6 and described in ref. [86]. A first beam splitter (BS1) splits the beam into $\mathbf{k}_1/\mathbf{k}_2$ and $\mathbf{k}_3/\mathbf{k}_{LO}$. The population time can be controlled by delay stage 1 (DS1, Physik Instrumente, M-664.164), which moves BS1 and a flat mirror. The assembly is mounted at 45° w.r.t. the beam path and changes the beam direction by 270°.

Chapter 4. Development and characterization of the 2D photon echo setup

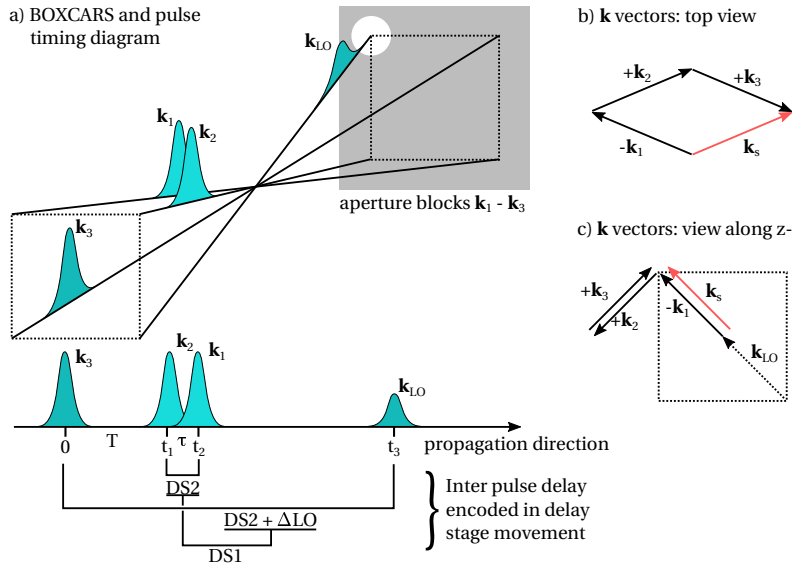


Figure 4.5 – (a) Drawing of the BOXCARS geometry showing the propagation direction of $\mathbf{k}_1 - \mathbf{k}_{LO}$. The vector diagrams show the projections of the k-vectors on (b) a horizontal plane along z and (c) onto the x - y plane, where z is the direction normal to the square of the four beams. t_{LO} is introduced by passing $\mathbf{k}_1 - \mathbf{k}_3$ through 1 mm of fused silica (not shown).

The reflected beam is passed through a compensation plate (CP), which is the uncoated substrate of the beam splitter, to keep the relative dispersion between the two arms of the interferometer close to zero. Open and filled arrows in Figure 4.6 correlate the temporal shift of the laser pulse with the direction of travel of the delay stage. In a second step, the beams from a) are split by two vertically displaced beam splitters (BS2), and the transmitted pulses \mathbf{k}_2 and \mathbf{k}_{LO} are delayed *synchronously* by delay stage 2 (DS2, Physik Instrumente, PIHera, P-625.1CL). Note that in Figure 4.6 b) two layers of optical elements are offset vertically from each other, and top- and bottom beams are distinguished by the difference in color shading. \mathbf{k}_1 and \mathbf{k}_3 are passed through CPs to compensate for the dispersion of BS2. The synchronous manipulation of the temporal shift of \mathbf{k}_2 and \mathbf{k}_{LO} allows to measure the photon echo signal in a rotating frame of reference, cf. Section 4.5.

Phase stability of approx. $\lambda/60$ at 540 nm is achieved passively by pairwise manipulation of beams, an idea introduced by Miller and co-workers [98] and Brixner et al. [46]. Briefly, since the relevant quantity is the relative phase between electric fields, arranging the beams in such a way that phase changes in one pulse, due to the oscillation of a mirror, are cancelled by the opposite phase change of another pulse. This can be seen by adding a fluctuating phase term

4.4. The noncollinear photon echo interferometer

to Equation (2.77) and requiring that this additional term is zero

$$\delta\Delta\phi = -\delta\phi_1 + \delta\phi_2 + \delta\phi_3 - \delta\phi_{LO} \stackrel{!}{=} 0. \quad (4.1)$$

For pair-wise manipulation of $\mathbf{k}_1/\mathbf{k}_2$ and $\mathbf{k}_3/\mathbf{k}_{LO}$, or $\mathbf{k}_1/\mathbf{k}_3$ and $\mathbf{k}_2/\mathbf{k}_{LO}$ the total phase deviation becomes negligible. Since the vibrations of a mirror can be decomposed into linear combinations of eigenmodes of the horizontal and vertical direction, reflections of all four beams by the same mirror does not introduce any relative phase changes. The phase stability over time can be followed by measuring spectral interferograms and determining the phase according to ref. [99].

The negative delay of the LO is introduced by passing $\mathbf{k}_1 - \mathbf{k}_3$ through a 1 mm thick glass plate. In this way, the LO passes through the same focus than the excitation beams without being influenced by the excited sample. The alternative would be to focus the LO slightly next to the excitation focus. The former method is preferred to assure that the photon echo and LO are perfectly collinear.

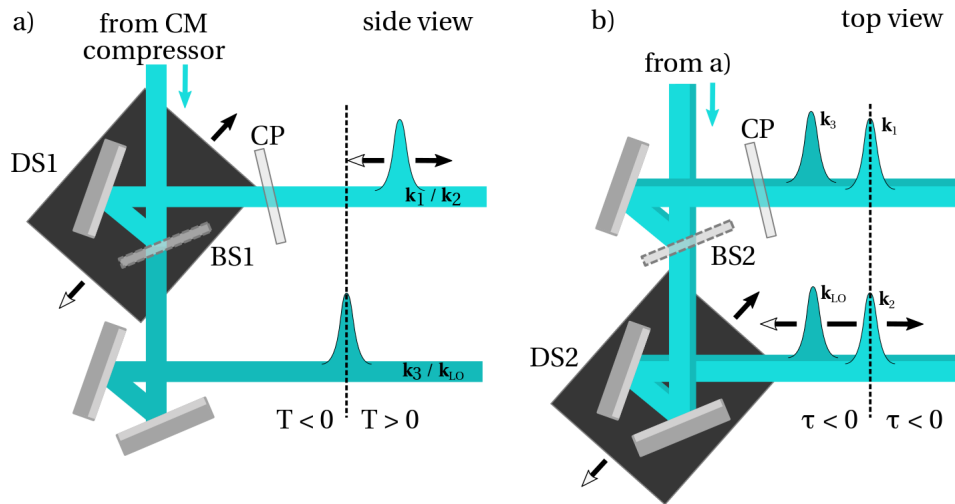


Figure 4.6 – Design of the interferometer. (a) The beam is split into $\mathbf{k}_1 / \mathbf{k}_2$ and $\mathbf{k}_3 / \mathbf{k}_{LO}$. DS1: delay stage 1, BS: beam splitter, CP: compensation plate. (b) The beams from (a) are split analogously into $\mathbf{k}_1 - \mathbf{k}_{LO}$. DS2: delay stage 2.

4.5 Measuring in a rotating reference frame

Retrieving the lineshape and excitation frequency dependence of a transient signal from a time-domain experiment requires to measure the envelop and carrier frequency of the photon echo signal. However, often the interesting observable is the lineshape of a transition, while the center frequency is of less relevance and/or can be recovered during the data treatment. When measuring the spectral interference pattern between a photon echo signal and the LO, a relative phase shift of π would change the phase of the spectral interference pattern by π as well. This implies that every time the coherence time changes by an amount equivalent to a π phase shift the phase of the detected interference changes as well and the detected signal oscillates with coherence time. If, as in our case, the LO time delay changes synchronously with the coherence time delay, the relative phase between the signal and reference field stays constant and the recorded spectral interferogram does not undergo a phase shift. The coherence time signal is ‘downsampled’ to $\omega_\tau \approx 0$ and becomes slowly varying with τ . We say it is measured in a *rotating frame*. This has the advantage that the coherence time axis can be measured with time steps exceeding the period of the carrier frequency, which is of the order of 1.5 fs to 3 fs, corresponding to an optical delay of 450 nm to 900 nm.

4.6 Data acquisition – Experimental procedure

4.6.1 Acquisition of raw data

The photon echo is heterodyne detected with the LO inside a spectrograph (Andor Shamrock 303i) and the resulting interference spectrum is recorded shot-to-shot, using a home-built CCD detector (Hamamatsu S11155-2048-02, 2048×1 pixel, $16 \times 500 \mu\text{m}$, up to approx. 5 kHz readout rate). The CCD array is read out by a field-programmable gate array (FPGA, National Instruments) integrated circuit and the interference data is subsequently background corrected and averaged in LabView, and saved as an ascii file, together with all set and readback position of the delay stages. The isolated LO spectrum is acquired during the background subtraction procedure and is saved to a separate file.

4.6.2 Background subtraction

The background subtracted signal is calculated on the four shot basis shown in Figure 4.7, where the pulses with \mathbf{k}_1 and \mathbf{k}_2 are periodically blocked by choppers at $R/2$ and $R/4$, with the repetition rate of the experiment R .

$$I_S = (I_{123LO} - I_{23LO} - I_{13LO} + I_{3LO}) / (\sqrt{I_{3LO}} + 1) \quad (4.2)$$

The number $n = 1, 2, 3$ in I_n is a shorthand notation for the pulse with wavevector \mathbf{k}_n and LO stands for \mathbf{k}_{LO} . The correct chopping sequence can be verified using the acquisition software

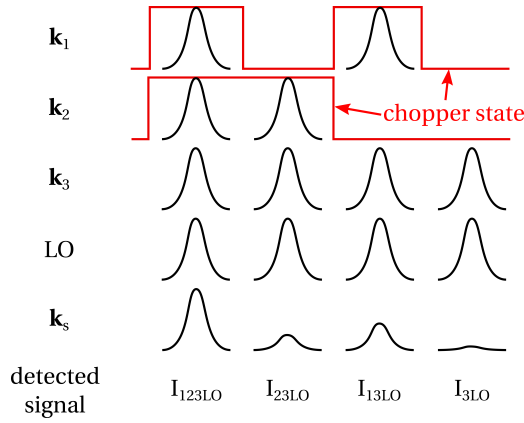


Figure 4.7 – Four shot background subtraction scheme.

or an external photodiode, when all but one of the two beams that are modulated by the choppers are blocked and lens tissue is placed at the sample position to scatter light of the selected beam into the spectrograph or onto the photodiode. Then the chopper phase is adjusted until the desired modulation of \mathbf{k}_1 and \mathbf{k}_2 is achieved.

4.6.3 Coherence time scan

The data is recorded for a range of coherence time steps and has the format $(\text{pix}, \tau_{\text{step}})$ with a size of $2048 \times N$ data points, where N is the number of coherence time steps. The acquisition time per coherence time scan varies between 1 and 2 minutes, depending on the amount of laser shots that are averaged and the number of coherence time steps. Typically, 1000 to 1500 laser shots are averaged and 80 to 120 coherence time steps from -150 to 150 fs are acquired.

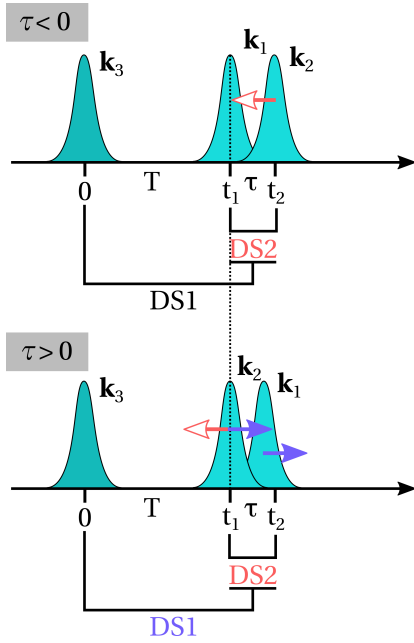


Figure 4.8 – Simplified illustration of the coherence time scan routine. Red arrows describe to temporal delay of DS2, blue arrows the temporal delay of DS1. Open- and closed arrowheads indicate the shift to positive- and negative time, respectively, and the convention is identical to Figure 4.6. Note that in the bottom diagram the red and blue arrows of \mathbf{k}_2 cancel each other, leading to a constant population time delay.

Figure 4.5 and Figure 4.8 show how the pulses are delays by DS1 and DS2. The coherence time is controlled by DS2, which shifts the temporal position of pulse \mathbf{k}_2 and \mathbf{k}_{LO} synchronously. For negative coherence times, \mathbf{k}_2 precedes \mathbf{k}_1 and it suffices to move pulse \mathbf{k}_2 closer to pulse \mathbf{k}_1 .¹ In this case the population time is constant, since the temporal delay between \mathbf{k}_1 and \mathbf{k}_3 does not change. During positive coherence times \mathbf{k}_2 arrives at the sample after \mathbf{k}_1 . Now however, since it is still the the temporal position of \mathbf{k}_2 that is changed by DS2, the time delay between \mathbf{k}_2 and \mathbf{k}_3 , i.e. the population time, decreases with increasing coherence time. To keep the population time constant, the optical delay of the pulse pair $\mathbf{k}_1/\mathbf{k}_2$, which is introduced by DS1, is decreased and thus the delay between \mathbf{k}_2 and \mathbf{k}_3 is increased, simultaneously to the decrease of the $\mathbf{k}_2/\mathbf{k}_3$ delay, which is due to the increase of the coherence time delay.

4.7 Spectral and temporal calibration

The acquired 3D dataset $I(\text{pix}, \tau_{\text{step}}, T_{\text{step}})$ is linearly spaced in the pixel, τ_{step} and T_{step} dimensions. The pixel axis [1,2048] can be replaced by a **wavelength axis from a calibration measurement** of a neon arc-discharge lamp, shown in Figure 4.9. This measurement allows

¹The fact that \mathbf{k}_2 precedes \mathbf{k}_1 in time is formally equivalent to redefining $\mathbf{k}_2 \rightarrow \mathbf{k}_1$ and $\mathbf{k}_1 \rightarrow \mathbf{k}_2$, such that the NR signal is emitted into the phase matched direction and heterodyne detected with the LO, instead of the R signal:

$$\mathbf{k}_s = -\mathbf{k}_1 + \mathbf{k}_2 + \mathbf{k}_3 \equiv \mathbf{k}_s^R \quad \Rightarrow \quad \mathbf{k}_s = -\mathbf{k}_2 + \mathbf{k}_1 + \mathbf{k}_3 = +\mathbf{k}_1 - \mathbf{k}_2 + \mathbf{k}_3 \equiv \mathbf{k}_s^{\text{NR}}$$

to calibrate the detection wavelength axis in the spectral range from 500 to 800 nm and results in a wavelength resolution of the spectrograph of 0.5 to 0.8 nm. Conversion to frequency yields an unevenly spaced frequency axis ν_{uneven} , which is subsequently interpolated onto an evenly-spaced frequency axis ν to avoid artifacts during the following Fourier transforms. Augulis and Zigmantas [48] show that despite the sub-nm resolution the spectral calibration using an arc-discharge lamp is not accurate enough to phase broadband 2D spectra. They use the interference between a white light spectrum and its time delayed replica from the inside of an empty cuvette to determine a (quadratic) residual phase function that is due to inaccuracies of the wavelength calibration. Using the inner reflection from a cuvette leads to a constant delay between pulse replicas and does not add any significant chirp to the reflected pulse, since the additional path, w.r.t. the first pulse, is exclusively in air. We find that for some of our measurements an additional quadratic phase term yields a better agreement between the integrated 2D spectrum and the auxiliary TA spectrum. Currently, we include this quadratic term in our phasing procedure, but it is plausible that the experimental origin of the quadratic phase is the inaccuracy of our wavelength calibration.

The **coherence time axis is calibrated** by multiplication of the τ_{step} -axis with a calibration factor that converts the stage position to an optical delay, $\mu\text{m} \rightarrow \text{fs}$, which is determined interferometrically. To reduce artifacts during the Fourier transform from the coherence time to the excitation frequency (last step in the data treatment) the data is interpolated from the readback value of τ onto the set value of τ , since the two differ by fractions of a femtosecond. The latter is evenly spaced, while the former is not, and Fourier transformation of the evenly spaced data clearly improves the quality of the final 2D spectrum and ensures that several measurements, at the same population time, can be averaged to increase the signal-to-noise ratio.

Calibration of the population time delay is less critical, so that the factor for the coherence time axis can be used here as well. This is a reasonable assumption, since the geometry of the two delay stages is identical. A good way to verify the accuracy of the time calibration is the comparison between the measured beating frequency Ω_{T} of a molecule and its literature value, e.g. the 590 cm^{-1} (lit. 590 cm^{-1} [72, 100, 101], 593 cm^{-1} [102]) Raman mode of Nile blue shown in Figure 4.11 (middle).

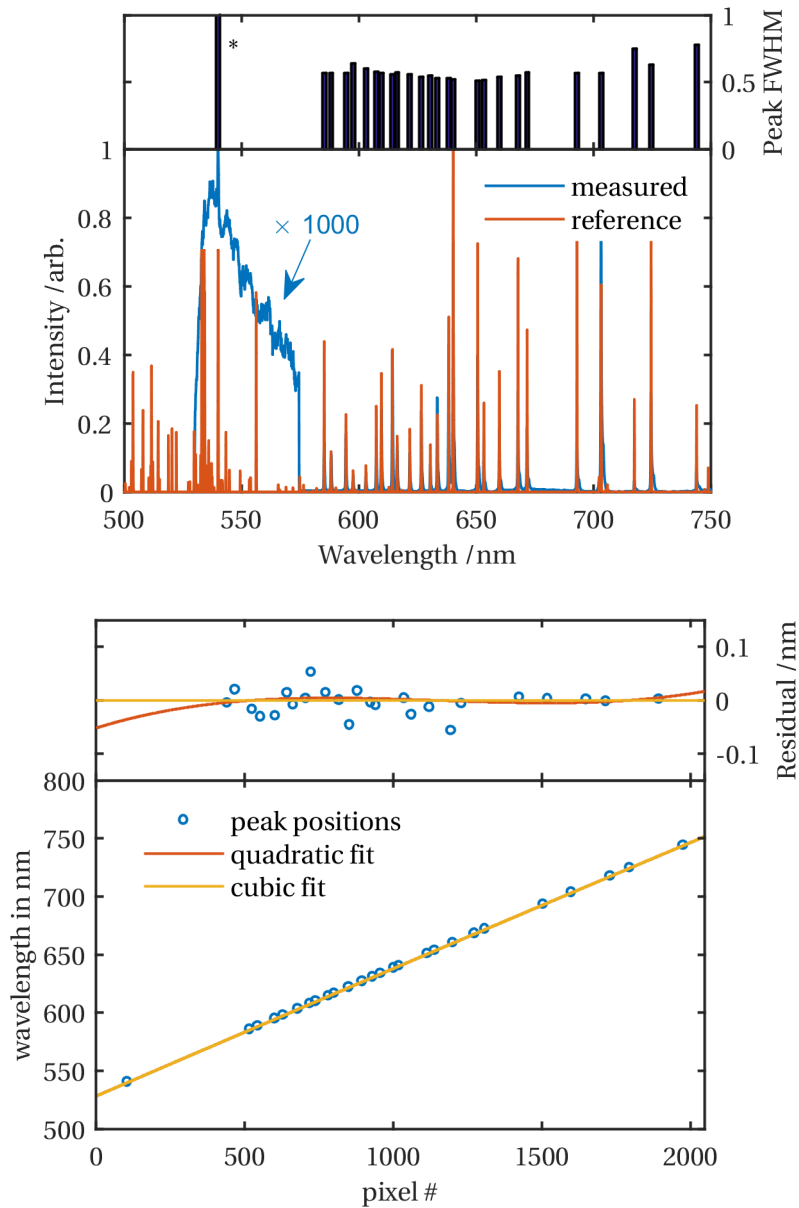


Figure 4.9 – (top) Reference neon spectrum (red) superimposed on the measured neon spectrum (blue). The region around 550 nm is amplified to observe the weak spectral features. The FWHM of the fitted peaks is shown above to assess the spectral resolution. The data point marked with an asterisk is too large, due to the small amplitude of the emission peak. (bottom) Quadratic and cubic fit of the peak positions and residuals (top panel).

4.8 Data treatment

4.8.1 From raw data to 2D spectra

The **measured interference between the photon echo signal and the LO** as a function of τ and at a fixed T is shown in Figure 4.10 and can be expressed as

$$I(\tau, T, \omega_t) = |E_{\text{sig}} + E_{\text{LO}}|^2 = |E_{\text{sig}}|^2 + |E_{\text{LO}}|^2 + 2 \text{Re} \{E_{\text{sig}} E_{\text{LO}}\}, \quad (4.3)$$

where E_{sig} and E_{LO} are the photon echo and LO fields. Inverse Fourier transformation of the data in the detection frequency dimension ($\omega_t \rightarrow \tilde{t}$) yields the Fourier components of the interference spectra (Figure 4.10, top left). Filtering of the Fourier component around $\tilde{t} = t_{\text{LO}}$ eliminates unwanted signals and reduces the noise of the measurement. Multiplication with $e^{-i\omega_t(t_{\text{LO}}+\tau)}$ removes the linear phase that results from the LO delay t_{LO} and the addition of $-i\omega_t\tau$ accounts for the fact that during the experiment t_{LO} changes synchronously with τ . Mathematically this corresponds to a rotation of the complex spectrum, transforming it back from the rotating- to the laboratory reference frame. By applying a back-Fourier transformation ($\tilde{t} \rightarrow \omega_t$) the interference term $2 \text{Re} \{E_{\text{PE}} E_{\text{LO}}\}$ is isolated (Figure 4.10, bottom left) and subsequent division by $E_{\text{LO}} = \sqrt{I_{\text{LO}}}$ yields the signal field. Expressed as an equation this procedure reads

$$E_{\text{sig}} = \frac{\mathcal{F}[\Theta(\mathcal{F}^{-1}[I_s]) e^{-i\omega(t_{\text{LO}}+\tau)}]}{\sqrt{I_{\text{LO}}}}. \quad (4.4)$$

Here, \mathcal{F} and \mathcal{F}^{-1} are the Fourier transform and inverse Fourier transform and Θ is the t -domain filtering function, either a rectangular, Hamming, or Tukey window.

The signal field E_{sig} is multiplied with a Hamming or Tukey window, this time in the τ -dimension, to minimize artifacts of the following Fourier transformation $\tau \rightarrow \omega_\tau$. Then it is zero padded in the τ -dimension to increase the excitation frequency resolution and Fourier transformed to yield the excitation frequency dependent 2D spectrum. In a final step, a phase correction function is applied to correct for inaccuracies of the $\tau = 0$ position and the phase ϕ_{LO} of the LO and any other residual phases. The parameters for the phase correction are determine in the so called ‘phasing’ procedure.

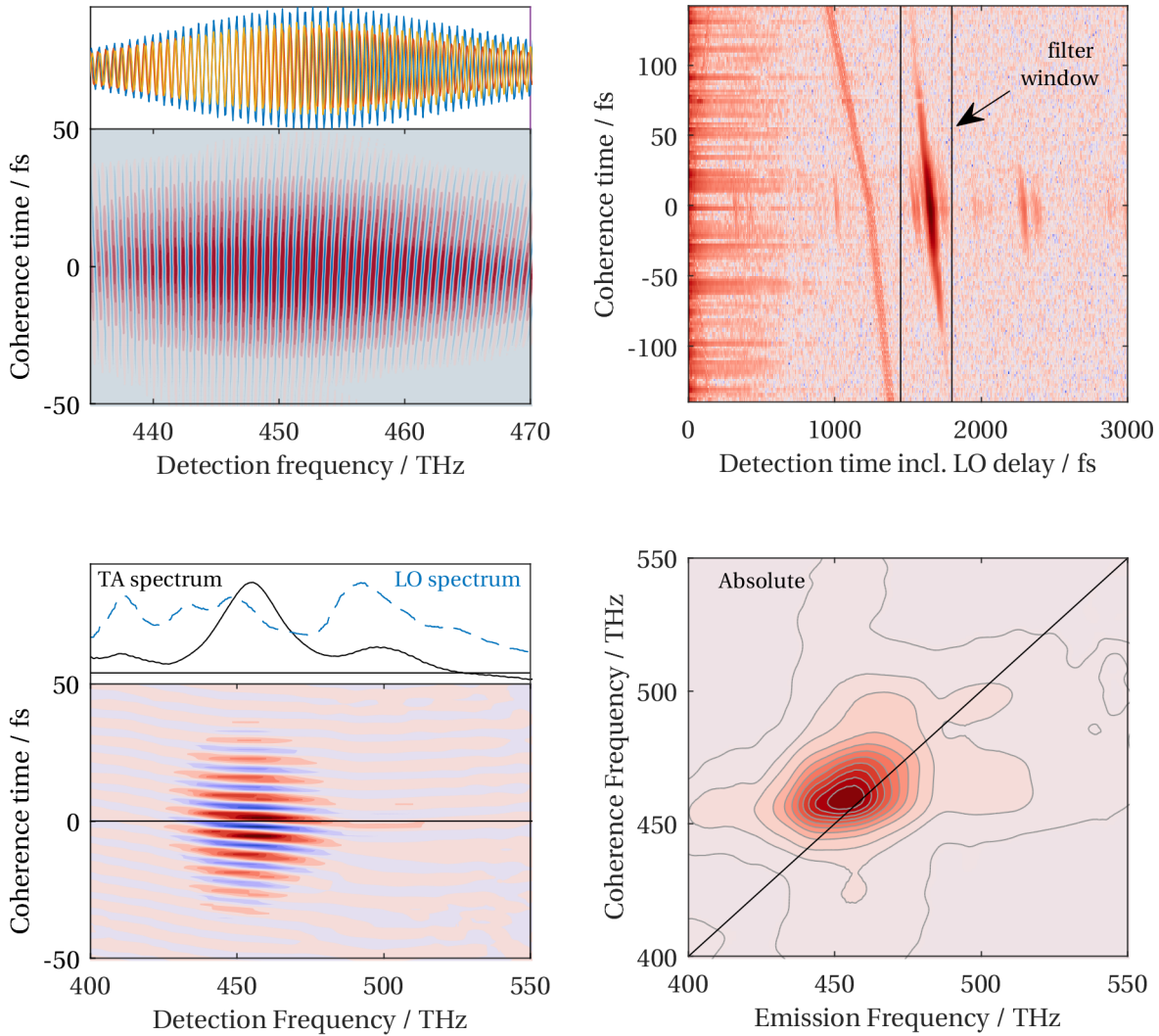


Figure 4.10 – Overview of the data treatment for terylene diimide. (top left) Fourier filtered data set showing the interference between the signal and the LO for varying coherence times. (top right) Inverse Fourier transform ($\omega_t \rightarrow t$) of the raw data. (bottom left) $I(\tau, T, \omega_t)$ after subtraction of a linear phase term that is due to the LO delay. The line plots show the TA spectrum (black, solid) and LO spectrum (blue, dashed) for comparison. (bottom right) Absolute value 2D spectrum after the final Fourier transform $\tau \rightarrow \omega_\tau$. Note the different axes and the fact that the 2D spectrum is rotated w.r.t. the rest of the spectra in this thesis. Contour lines of the 2D spectrum are at 1,5, 10, 20, ..., 90 % of the signal maximum.

4.8.2 Phasing

To *phase* the data we make use of the projection-slice theorem by comparing the 2D spectrum integrated over ω_τ to a TA measurement under identical conditions [44]. The TA measurement is performed with \mathbf{k}_1 as the pump- and \mathbf{k}_{LO} as the probe beam. Residual phase inaccuracies of the signal are corrected for by multiplying the complex 2D data with a τ_0 correction function

$$\Phi_t = e^{-i2\pi\omega_\tau\tau_c} \quad (4.5)$$

and a phase correction function

$$\Phi_c = e^{-i2\pi((\omega-\omega_0)t_c+\phi_c)}, \quad (4.6)$$

where the parameters τ_c , t_c and ϕ correct for the inaccuracy of the τ_0 position, the LO delay and the constant phase, respectively. A quadratic phase term, $2\pi(\omega - \omega_0)^2 t_q^2$, can be added to account for 2nd order phase distortions, but should only contribute minimally. The phase 'corrected' complex 2D data is compared to an auxiliary TA spectrum according to Equation (2.78) and the optimal parameters τ_c , t_c and ϕ_c (and t_q) are found using a minimization algorithm:

```

1 fun = @(r) real ( sum ( r(1) * D2D_correctPhase ( signal, nu_tau, nu_t, r(2), r
    (3), r(4))) - TA;
2 x0 = [ ... ]; % starting values
3 lb = [ ... ]; % lower bounds
4 ub = [ ... ]; % upper bounds
5 options = optimoptions(@lsqnonlin, 'Algorithm', 'trust-region-reflective', '
    FunctionTolerance', 1e-8);
6 problem = createOptimProblem('lsqnonlin', 'objective', fun, 'x0', x0, 'lb', lb, 'ub',
    ub, 'options', options);
7 ms = MultiStart;
8 [x, Fval] = run(ms, problem, 50);
9
10 function [TwoDcorr] = D2D_correctPhase ( data, nu_tau, nu_t, t_c, phi_c, tau_c
    )
11     temp = data .* exp(-1i * 2 * pi * nu_tau * tau_c)';
12     TwoDcorr = temp .* exp(-1i * 2 * pi * (nu_t * t_c + phi_c));
13 end

```

4.8.3 Analysis of dynamics and coherences

To correlate the vibronic beatings of the system during the population time T with the excitation and detection energies we need to subtract the exponential kinetics from the 2D spectrum and Fourier transform the residuals w.r.t. the population time.

$$\mathcal{F}[I(\omega_\tau, T, \omega_t)] \rightarrow I(\omega_\tau, \Omega_T, \omega_t) \quad (4.7)$$

This procedure does not require a global fit of the kinetics, since we only need to subtract the non-oscillatory components to perform the Fourier transform and, in this case, are not interested in the kinetics of the system. The time traces are thus fitted by a convolution of a Gaussian instrument response function (IRF) and its 1st and 2nd time derivative and N exponential terms. To accelerate the analysis, the 2D spectra at every T are binned onto a smaller grid with a frequency step size $\Delta\omega_t = \Delta\omega_\tau \approx 65 \text{ cm}^{-1}$. A histogram of the IRFs full width half maximum (FWHM) is used to assess the temporal resolution of the measurement.

The resulting 3D dataset is visualized as 2D maps $I(\omega_\tau, \Omega_T, \omega_t)$ at a fixed beating frequency Ω_T . Summation along ω_τ and ω_t yields the total frequency content of the measurement, which can be compared to a static Raman spectrum to identify different vibrational modes of the system. Separate treatment of R and NR signals helps to identify the origin of the observed coherence. To achieve this, the $I(\tau, T, \omega_t)$ data set is split at $\tau = 0$ and treated separately, resulting in the rephasing and non-rephasing contributions.

4.9 Exemplary 2D spectra of dye molecules in solution

To commission the 2D photon echo experiment we performed measurements on solutions of nile blue (nb), rhodamine 800 (rh800), terylene diimide (tdi), and pinacyanol iodide (pin), whose broad absorption bands lie within the 500 to 750 nm spectral window, accessible with the HCF white light spectrum and the CM compressor. nb, rh800, and pin are dissolved in ethanol and tdi in chloroform. Figure 4.12 shows an overview of the absolute and absorptive 2D dye spectra. The absorption- and transient absorption spectra are shown as red and black lines on the x- and y-axis, respectively. All 2D measurements were performed without major

4.9. Exemplary 2D spectra of dye molecules in solution

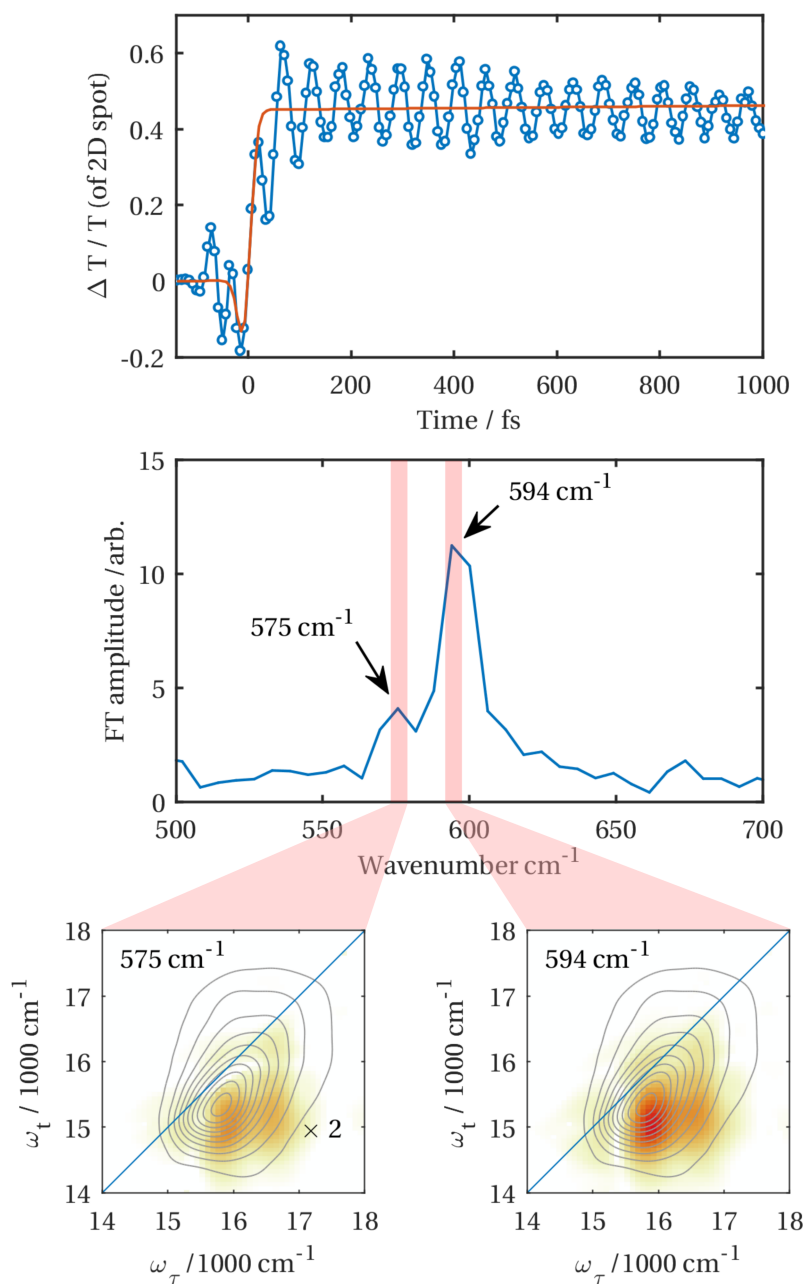


Figure 4.11 – Exemplary coherences analysis of Nile blue. (top) Time traces at every point of the 2D spectrum are fitted by a Gaussian IRF and exponential decays. The residual of the fit is Fourier transformed to reveal the (middle) coherence frequency spectrum. (bottom) The excitation / detection dependence of each coherence can provide insight into their microscopic origin.

Chapter 4. Development and characterization of the 2D photon echo setup

experimental readjustments, proving the versatility and stability of the setup. The spectral window is currently only limited by the approx. 200 nm acceptance bandwidth of the detector, which is necessary to achieve a sufficient spectral resolution in order to record the interference between the signal and the LO.

We note a few remaining issues in the 2D spectra:

- The absorptive spectrum of rh800 shows negative amplitude signals on the diagonal at $17000\text{ cm}^{-1} / 17000\text{ cm}^{-1}$, which might be due to phase twists of the data.
- The intensities of the high energy diagonal peak and of the cross-peaks is lower than expected, judging by the amplitudes of the respective features in the static- and transient absorption spectra.
- Noise from the Fourier transform $\tau \rightarrow \omega_\tau$ ends up in the 2D data. This artifact is observable in the vicinity of the largest amplitude peak.
- All peaks seem to be less well resolve than in the literature, which might be related to the missing intensity of the upper diagonal- and cross-peaks.

4.10 Experimental outlook

The quality of the 2D spectra of molecular dyes confirms that the technical developments that have been discussed significantly improved the experimental setup. Slight modifications and adjustments will however be necessary to address the issues mentioned at the end of the previous section. These involve, but are not limited to, pulse compression, different white light spectra, and focusing conditions. Beyond these possible improvements, future work will be dedicated towards data analysis, specifically the separation of 2D spectra into R and NR components and the extraction of beatings maps (cf. Section 2.5.6). Subsequently, we intend to measure systems with increasing complexity, to gain experience with- and assess the possibilities of multidimensional coherent spectroscopy and move towards studying the interplay between electronic- and structural degrees of freedom in porphyrin monomers and dimers, metal complexes, and molecular assemblies.

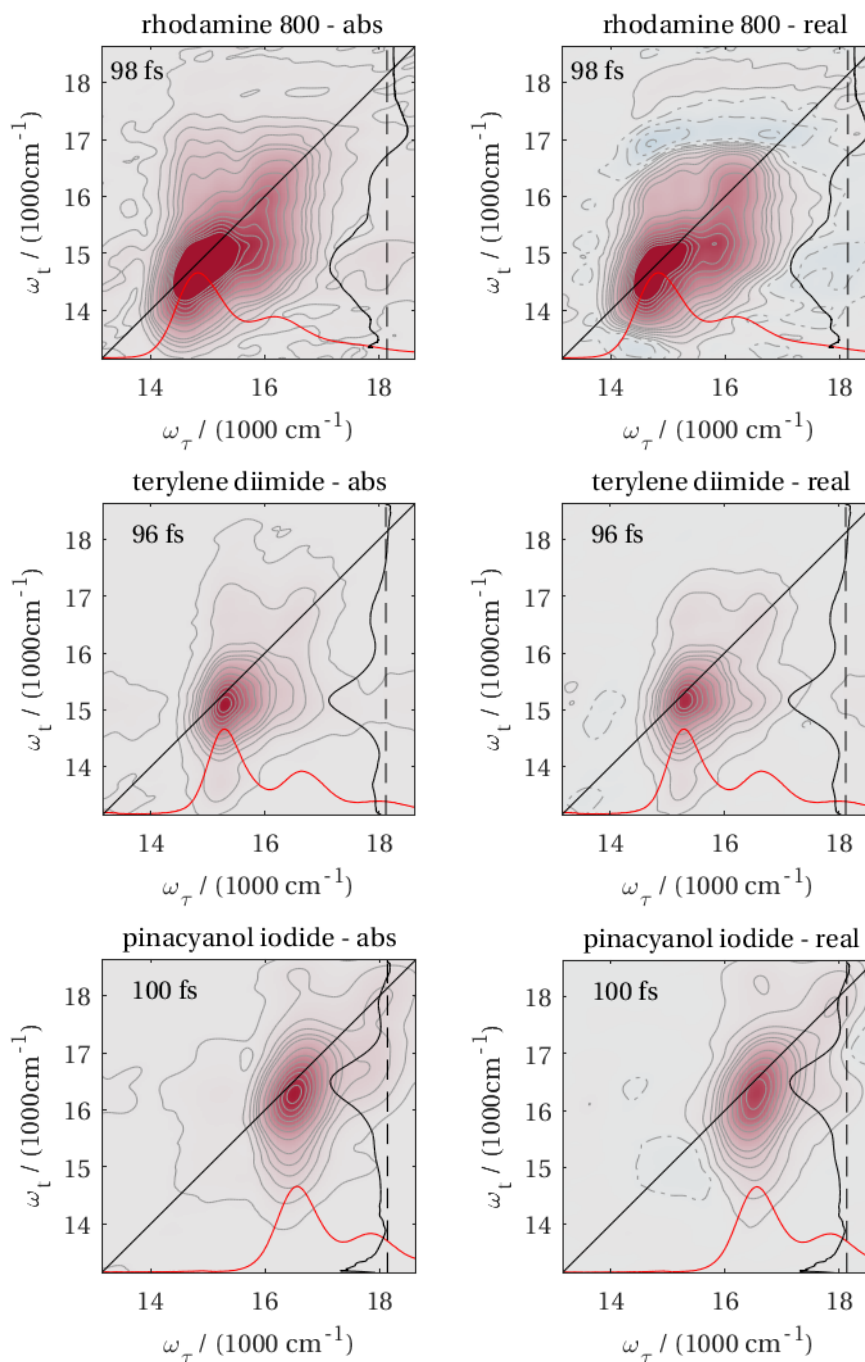


Figure 4.12 – Comparison of the 2D spectra of test dyes. Rows: nb, rh800, tdi, and pin. Columns: absolute- and real (absorptive) 2D spectra. Contour lines are at 1, 4, 8, 12, 16, 20, 30, 40, ... 100 % of the data set, which is normalized to a global maximum, excluding the data around $T = 0$. The absorption spectrum (red line) and transient absorption spectrum (black line) for each dye is shown for comparison on the x-axis and y-axis, respectively.

5 Transient spectroscopy of

$[\text{Pt}(\text{ppy})(\mu\text{-tBu}_2\text{pz})]_2$

5.1 Background

$[\text{Pt}(\text{ppy})(\mu\text{-tBu}_2\text{pz})]_2$, hereafter abbreviated as Ptppy, belongs to a class of di-metal complexes that have been synthesized [103–105] and studied extensively because of their interesting photophysical properties, which have e.g. been exploited in organic light emitting diodes [106–108], photocatalysis [109, 110], and as model systems to understand the connection between topology of excited state potential energy surfaces and photoinduced structural dynamics [30, 32, 111–116, and others]. The structural dynamics are typically observed via a periodic modulation of a transient signal, a so-called wavepacket, reflecting snapshots of the coherent spatial localization of the nuclei in a certain vibrational mode. Champion and co-workers highlight that wavepackets can be *field-* or *reaction-driven* [32, 50, 51]. The former implies that the exciting laser field directly creates the wavepacket on a given excited state, which may or may not subsequently be transferred to a ‘final’ state, as observed in Pt(pop) [30, 32, 115], while the latter means that the wavepacket is generated during a sudden structural deformation, such as the contraction or expansion of bonds upon optical excitation, even if the initially excited mode does not form a wavepacket [114, 117].

In Ptppy optical excitation of the $S_0 \rightarrow S_1$ transition promotes an electron from an antibonding Pt-Pt σ^* molecular orbital to a mixed metal-ligand centered Pt- π^* orbital, in a so called metal-metal-to-ligand-charge transfer (MMLCT) excitation, cf. Figure 5.1 (right). The common motif between Ptppy and other di-platinum complexes, such as Pt(pop) or Pt(pop-BF₂) [31, 32,

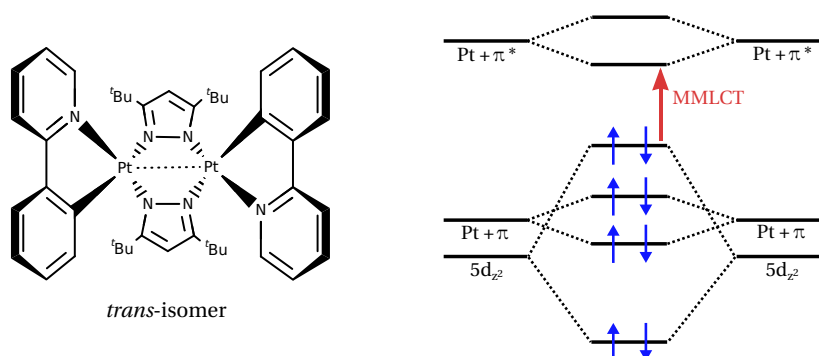


Figure 5.1 – (left) Molecular structure of Ptppy showing the cis-isomer and (right) molecular orbital diagram. Electronic interaction between the two halves of the molecule lifts the degeneracy between the orbitals leading to the appearance of the MMLCT transition.

111], or other di-metal complexes [112], is that the optical excitation promotes an electron from an antibonding metal-metal molecular orbital to a higher lying electronic state, which is not necessarily a metal-metal molecular orbital. The removal of an electron from an antibonding orbital effectively creates or increases the σ -like bonding character between the metal centers. As a result the molecule starts to oscillate about its new equilibrium Pt-Pt bond distance in the excited electronic state. Controlling the distance between the Pt atoms by changing the size of the residual (tert-butyl in Ptppy) on the pyrazolate linker has allowed study of the effect of the equilibrium Pt-Pt distance on the optical properties. It was found that for shorter distances between the Pt atoms the optical properties change significantly due to the interaction between the two halves of the molecule [105, 118, 119]. The reason is that, due to the proximity of the two Pt atoms and π -electron systems of the phenylpyridine (ppy) ligands ($d_{\text{PtPt}} = 2.83 \text{ \AA}$ in Ptppy), the degeneracy between the orbitals on each half of the molecule is lifted, leading to the appearance of the MMLCT band. Hypothetically, a sufficiently broadband, Fourier transform-limited laser pulse can be used to excite an electronic superposition of $\text{Pt} + \pi^*$ states [118], which has been the subject of study of refs. [118, 120–122].

Most of the work on Ptppy has been carried out by Chen and co-workers who concluded that upon optical excitation the molecule relaxes to a triplet state within approx. 150 fs [118–122]. Monochromatic transient absorption anisotropy (TAA) measurements¹ of the lowest absorption band at 500 nm initially suggested that the electron density after optical excitation is delocalized between the ppy ligand and subsequently the contraction and associated

¹Narrowband femtosecond laser pulses and spectrally integrated detection

5.2. Short excursion: Coherences in time-domain spectroscopy

oscillation of the Pt-Pt distance localizes the electron density on one of the ligands, alternating with every period of the Pt-Pt oscillation [118, 120]. This behavior persists following intersystem crossing (ISC), which is identified from a change in oscillation frequency of the anisotropy signal from 320 cm^{-1} to 110 cm^{-1} . Subsequent broadband transient absorption (TA) experiments have been analyzed, assuming a 150 fs ISC process, and the observed few picosecond dynamics are interpreted as internal conversion (IC) and vibrational relaxation (VR) processes within the triplet state manifold [119]. Recent TA measurements by the same group rationalize their previous observations as being due to coherent vibrational motion rather than an electronic coherence, since the latter would have an oscillatory period of 10 – 20 fs [120, 122], which corresponds to $1600 - 3300\text{ cm}^{-1}$.

It is clear that the orbital overlap between the two halves of the molecule leads to the modification of the electronic structure and lifts the degeneracy between them. The questions that then arise are whether (i) the excitation is to one or more singlet states and if so, (ii) is this electronic coherence observable and (iii) does it influence the kinetics and dynamics of the system, by interacting with the vibrational coherence. Regarding the reported [118, 120–122] vibrational coherence, it is of interest to understand if (iv) it is field- or reaction-driven and (v) how it is involved in the ultrafast ISC.

We try to address these questions by providing a thorough analysis and interpretation of the transient absorption spectra with the help of broadband transient absorption anisotropy and fluorescence up-conversion measurements. The aim of the latter is to determine the lifetime of the singlet excited state, and help assign the observed signal to kinetics within the singlet or triplet manifold of states.

5.2 Short excursion: Coherences in time-domain spectroscopy

The availability of time-domain spectroscopy with femtosecond or nowadays even attosecond temporal resolution has motivated the study of coherent non-equilibrium dynamics (in addition to energy relaxation kinetics) in a large variety of scientific fields, including molecular chemistry [123–126], biochemistry [127–129], solid-state physics [130], and atomic physics [131, 132]. To grasp the concept of *coherence*, it is instructive to consider its general

definition as the phase (and amplitude) relation between two or more classical or quantum mechanical *fields*. A phenomenon is *coherent*, if the superimposed fields have a fixed phase relationship. If however the phases between fields are random, the phenomenon is *incoherent*. The most frequent coherences encountered in femtosecond time-domain spectroscopy of molecules are vibrational wavepackets, i.e. coherent superpositions of vibrational eigenfunctions. A wavepacket on an single, isolated, anharmonic potential will ‘oscillate’ on said potential until the individual components of the wavepacket, the vibrational eigenfunctions interfere destructively (dephase) after a time T . Since the system is isolated, the eigenfunctions will interfere constructively again (rephase) leading to a revival of the wavepacket with a π phase shift after $2T$ (for details see [26]). Interactions with a dissipative bath decrease the ability of the system to revive the wavepacket. These interactions can be elastic collisions² [133, p. 2], which introduce random ‘phase jumps’, or fluctuations of the local environment, which modulate the shape of the potential and effectively change the spacing of the vibrational levels and thus the frequencies (phases) of the vibrational eigenfunctions (cf. Brownian oscillator model, [22, 134–136]). Both of these effects lead to the loss of the coherence of the system – remember that coherence describes the possibility to predict a future state of the system. The revival of the wavepacket is only observed for systems with weak or no interactions with the bath, e.g. in gas-phase experiments. In solutions wavepacket revival is not observed, due to the described loss of coherence, caused by the system-bath interaction.

Since it is difficult to measure individual molecules, experiments are typically performed on ensembles, e.g. a large number of molecules in solution, where the measured signal is an average over the ensemble. As a consequence, since every sub-system evolves in a slightly different local environment, the relative phases between the microscopic signals, which are initially in-phase, will randomize, leading to the loss of the coherent macroscopic signal. Compared to the effects on the individual anharmonic oscillator described above, this effect is a property of the ensemble, i.e. the macroscopic coherent signal is lost even though the individual sub-systems still evolve coherently. In the literature these phenomena are referred to as *dephasing* and *decoherence*, but the terms are often used synonymously or are poorly defined. Sometimes, dephasing is described as the combination of decoherence and the loss

²Inelastic collisions results in population relaxation and are not considered here.

5.3. Sample preparation and characterization

of phase correlation between sub-systems of an ensemble. In this case, decoherence describes the loss of coherence of an individual sub-system. Another discrimination is between *pure* dephasing and *ensemble* dephasing, which describe the loss of coherence of the individual sub-system and the loss of phase correlation between sub-systems, respectively.

Many coherences manifest themselves as periodic modulations of the observable signal, but identifying the origin of the oscillations, i.e. if they are electronic, vibrational, or vibronic (breakdown of Born-Oppenheimer approximation) in nature, is far from being trivial. However, there is a clear necessity for a better understanding of the experimental signatures of coherences to help understand the interplay between structural and electronic degrees of freedom in a variety of systems, such as donor-acceptor dyads [137, 138], organic photo-voltaics [139], polymers [140], and dimetal complexes [30–32, 110, 116], to name a few. Many of these systems have been used as test systems to observe and identify coherences and the latter are the subject of this study.

5.3 Sample preparation and characterization

Ptppy was synthesized according to the procedure in ref. [105] by E. Baranoff (University of Birmingham), yielding two geometrical isomers, in which the direction of the phenylpyridine (ppy) ligands is reversed, with a cis:trans ratio of ~1:2. Absorption and emission measurements of Ptppy in toluene have been performed on low concentrations inside 1 cm cuvette and the extinction coefficient at 500 nm is $\sim 6000 \text{ M}^{-1} \text{ cm}^{-1}$. To achieve an optical density (OD) that is sufficiently high for TA measurements in a 1 mm cuvette a saturated solution is prepared by first dissolving Ptppy in toluene until a solid residue is observed and sonication of the suspension further increases the amount of dissolved molecules. Filtration and subsequent evaporation of the solvent by sparging the solution with argon or evaporation of the solvent under vacuum (23°C, 30 mbar) yields a concentrated solution with an OD of 0.15 to 0.2 at 500 nm inside a 1 mm cuvette. Under these conditions the solution remains stable for 2 to 3 days after which the formation of a solid residue is observed. The aggregation of molecules can be observed by the increase of scattering or via the appearance of a characteristic tail on the red side of the absorption spectrum. Figure 5.2 shows the absorption and emission spectrum of Ptppy in toluene. The absorption spectrum is in good agreement with previously

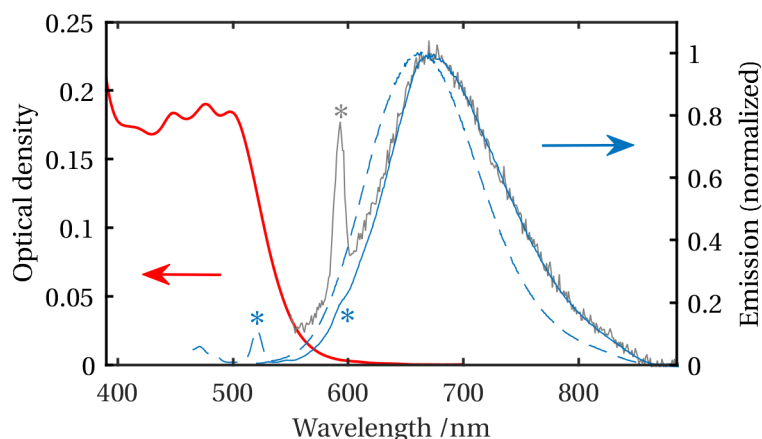


Figure 5.2 – Absorption (red) and emission (blue) spectrum of $[\text{Pt}(\text{ppy})(\mu\text{-tBu}_2\text{pz})_2]$ in toluene and the emission spectrum (light gray) at low solute concentration. The blue dashed line is the emission spectrum measured on a different fluorometer. The shoulder and peaks marked by asterisks are due to Raman scattering of the 500 nm excitation.

published data [118], while the emission spectrum measured on our fluorometer (blue, solid line) is redshifted by 10 nm. The emission spectrum at low solute concentration (light gray in Figure 5.2) shows that this shift is not due to self-absorption, or aggregation [141]. It may however be the result of an improper or missing wavelength dependent correction [142], since the emission measured on the fluorometer of the Temps group at the Christian-Albrecht-University of Kiel (blue, dashed line in Figure 5.2) is shifted by 10 nm and agrees with the literature.

5.4 Experimental details

5.4.1 Transient absorption

The transient absorption setup has been described in detail in Chapter 3. Briefly, the output of a Spectra Physics regenerative amplifier (795 nm, 1 kHz, 600 mW) is split by a 90/10 (T/R) beam splitter into a pump and a probe beam. The 500 nm pump pulse is generated using a home-built noncollinear optical parametric amplifier (NOPA) and is compressed to its Fourier limit (25-30 fs, determined by second-harmonic generation (SHG) frequency resolved optical gating (FROG) at the sample position) in a prism compressor. The polarization of the pump pulse is controlled by a broadband $\lambda/2$ waveplate and is set to the magic angle at

54.7°(relative to the probe polarization). For anisotropy measurements the polarization of the pump pulse is set parallel and perpendicular relative to the probe. The probe beam is delayed and focused into a 5 mm calcium fluoride (CaF₂) crystal, generating a white light continuum from 400 to 900 nm. The 750-850 nm region is blocked by a bandstop filter, to decrease the average power of the probe pulse on the sample. The pump and probe beams are overlapped at the sample position with focal diameters of approx. 150 μm and 20 μm , respectively, to guarantee a homogeneous excitation across the probe volume. The probe beam is focused into a multimode fiber and coupled into a grating spectrograph. The dispersed white light is imaged onto a home-built line CCD detector and read out using our in-house data acquisition software. The temporal resolution of the experiment is on the order of 190 fs (FWHM) as determined by fitting of the coherent artifact, which is very intense and dominates the TA signal between ± 100 fs.

5.4.2 Fluorescence up-conversion

Single-color detected femtosecond fluorescence up-conversion spectroscopy (FIUPS) has been performed in collaboration with the Temps group at the Christian-Albrecht-University of Kiel. The setup has been described previously in ref. [143]. Briefly, a Ti:Sa laser (Clark MXR CPA-2001) provides femtosecond laser pulses (150 fs, 775 nm, 1 kHz) that are used to generate the 480 nm excitation pulses using a home-built NOPA and a prism compressor is used to achieve a pulse duration < 50 fs. The sample is circulated inside a 1 mm flow cell with 0.2 mm thin fused silica windows and a beam stop in combination with a Schott WG glass filter is used to block the transmitted and scattered pump light. The fluorescence is collected using large aperture, 90° off-axis parabolic mirrors ($f = 119$ mm, 63.5 mm aperture) and refocused into a β -barium borate (BBO) crystal, where it is time-gated with the 775 nm fundamental pulse using sum-frequency generation (SFG) under type I phase matching conditions. The 100 μJ gate pulses are delayed by a computer controlled translation stage and focused into the BBO at an angle of approx. 14° w.r.t. the fluorescence. The up-converted fluorescence signal is monochromated using a $f = 0.1$ m double monochromator and detected by a photomultiplier (Hamamatsu R1527P) in combination with a preamplifier (Stanford Research SR 445), which records the up-converted signal intensity for each time delay. The measurement is repeated

for a fixed excitation wavelength over a range of emission wavelengths by rotating the grating of the monochromator. The up-conversion crystal is not changed during the measurements, which implies that the spectral intensity of the measured signal is a poor indication of the spectral shape of the transient fluorescence signal.

5.5 Results

5.5.1 Magic angle transient absorption

The transient absorption measurement under magic angle conditions is shown in Figure 5.3 (convention: $\Delta T/T_0$). During the temporal overlap of the pump and probe pulses the data shows a strong ‘**coherent artifact**’ [144–147], similar to the one observed in an auxiliary solvent-only measurement (SI, Figure 5.12), that can be fitted by the wavelength-dependent, linear combination of a Gaussian and its first- and second derivative with a FWHM of 190 fs. We do not observe any significant contribution that could be associated to the Ptpy dynamics or kinetics convoluted with the coherent artifact. The transient signal of Ptpy is weak and negative during the entire delay scan from 0.15 ps to 250 ps. Between **400 nm and 500 nm** the spectrum is very congested, but upon closer inspection the transient can be analyzed in two different ways. *Either*, as two negative bands, with a width of ~10 nm, that are centered at 428 nm and 457 nm and shift to 425 nm and 463 nm, respectively, over the course of a few ps. *Alternatively*, the signal is composed of two positive-going bands³ at 445 nm and 473 nm, also with a width of ~10 nm, that have negative amplitude due to a broad, overlapping negative band, and do *not* show any significant spectral shift over time. *For comparison*, the linear absorption bands are centered at 447 nm, 476 nm, and 499 nm (cf. Figure 5.2). Over the course of a few tens of ps the transient signal in the spectral region below 500 nm continues to decay, which is not observed at longer wavelength. This discrepancy makes a global fit of the data difficult (*vide infra*). The **500 nm to 700 nm** region shows a negative band at approx. 537 nm with a width of ~20 nm that is present immediately after excitation. Between 580 nm and 700 nm a negative signal grows in during the first ps. Both of these features oscillate in the

³Positive-(negative)-going bands are defined here as tending towards positive or negative infinity even though they may have negative (positive) amplitude. E.g. a band is positive-going, but has negative amplitude, if it is a positive band superimposed by a (broad) negative band with larger amplitude.

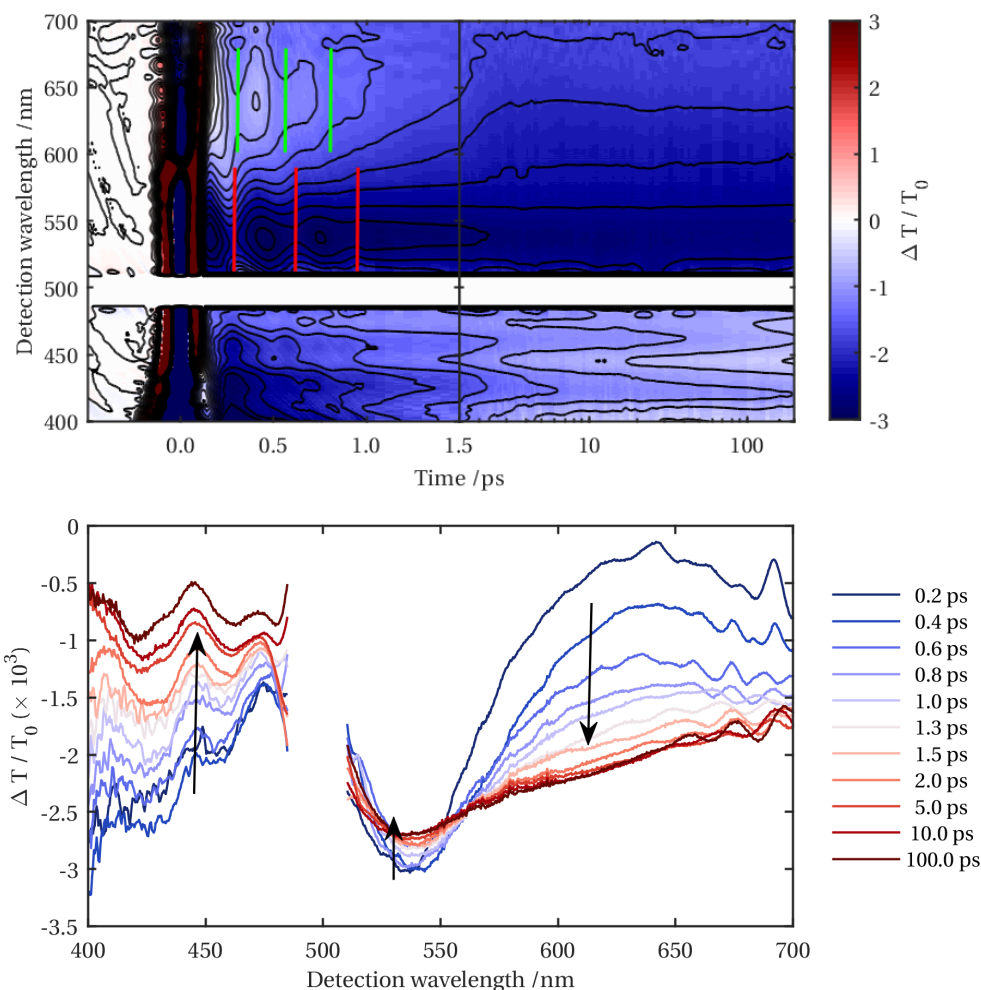


Figure 5.3 – Chirp-corrected TA measurement of Ptpy in toluene. (top) The time-wavelength representation reveals oscillations of the signal during the first picosecond. Red and green vertical lines indicate the two distinct frequency with periods of 245 fs (130 cm^{-1}) at 540 nm and 340 fs (103 cm^{-1}) at 640 nm, respectively. (bottom) The transient spectra suggest the presence of an isosbestic point between 550 nm and 560 nm.

time-domain with periods of 330 to 350 fs ($\tilde{\nu}_{540\text{nm}} \approx 100\text{ cm}^{-1}$) at 537 nm and 235 to 255 fs ($\tilde{\nu}_{630\text{nm}} \approx 135\text{ cm}^{-1}$) around 630 nm (Figure 5.9). They are damped with time constants of $\sim 0.2\text{--}0.4\text{ ps}^4$. A Fourier analysis of the oscillations cannot resolve the two components, since the fast damping of the oscillations does not allow for sufficient frequency resolution. We note however that a global fit of the oscillations requires a minimum of two frequencies and visual inspection of the data (Figure 5.9) clearly shows two distinct periods.

⁴From a global fit with two or three exponential terms and two damped oscillations.

In addition to the coherences due to Ptpy, we observe a **coherent response of the solvent**, shown in Figure 5.12, with a period of 155 fs ($\tilde{\nu} = 215 \text{ cm}^{-1}$) under parallel and perpendicular relative pump-probe polarization, which we attribute to a rovibrational out-of-plane toluene Raman mode with a_2'' symmetry, as previously measured with $\tilde{\nu} = 217 \text{ cm}^{-1}$ [148, 149]. The mechanism that leads to the observation of coherences of a transparent solvent in TA spectroscopy is described in detail by Cho et al. [150]. At magic angle this coherent signal of the solvent is absent, however, since we calculate the anisotropy from the parallel and perpendicular TA data, we need to consider that it can potentially contribute to the oscillations observed in the sub-ps anisotropy (*vide infra*). **Global fitting** of the magic angle TA data (excluding the pump wavelength region from 485 to 510 nm, as well as the ‘coherent artifact’ before $t = 0.15$ ps) with three exponential functions and two damped oscillatory functions works well above 500 nm, but does not fully capture the kinetics below 500 nm, as shown in Figure 5.4. In general, we note that for the present data set the result of the global fit strongly depends on the fitting parameters and thus the resulting time constants should be understood, and treated accordingly, i.e. qualitatively rather than quantitatively. Details of the algorithm for the global fit can be found in ref. [151]. Figure 5.4 shows (top) the **decay associated spectra** (DAS) and (bottom) time traces of the data and the fits at selected wavelengths. **Below 500 nm** the kinetics are described by three time constants, sub-1 ps, 20 ps, ∞ (fixed, lit. triplet lifetime $0.85 \mu\text{s}$ [118] or $0.9 \mu\text{s}$ [152]). The sub-1 ps DAS has a negative band that increases with decreasing wavelength with a shoulder at ~ 440 nm. The oscillations of the signal during the first ps are weaker in this spectral region, but nevertheless introduce uncertainty in the fit of the exponential kinetics. An intermediate time constant of approx. 20 ps has only little amplitude, but is required to fit the data convincingly. We note that the residuals between 10 and 200 ps show a trend that deviates from zero, especially at a few tens of picoseconds, but adding a fourth time constant does not improve the fit significantly and does not add any additional information. It is possible that the kinetics slightly deviate from being purely exponential, which can be justified by the observed spectral shift of these bands. Finally, the constant DAS agrees with the observed transient spectrum at the longest measured time delay and has two negative bands at 425 and 460 nm, or, analogously to the description of the transient signal (*vide supra*) two positive-going bands at 445 nm and 475 nm. In the **500 to 700 nm** region the kinetics are sufficiently described by two of the three time constants. The

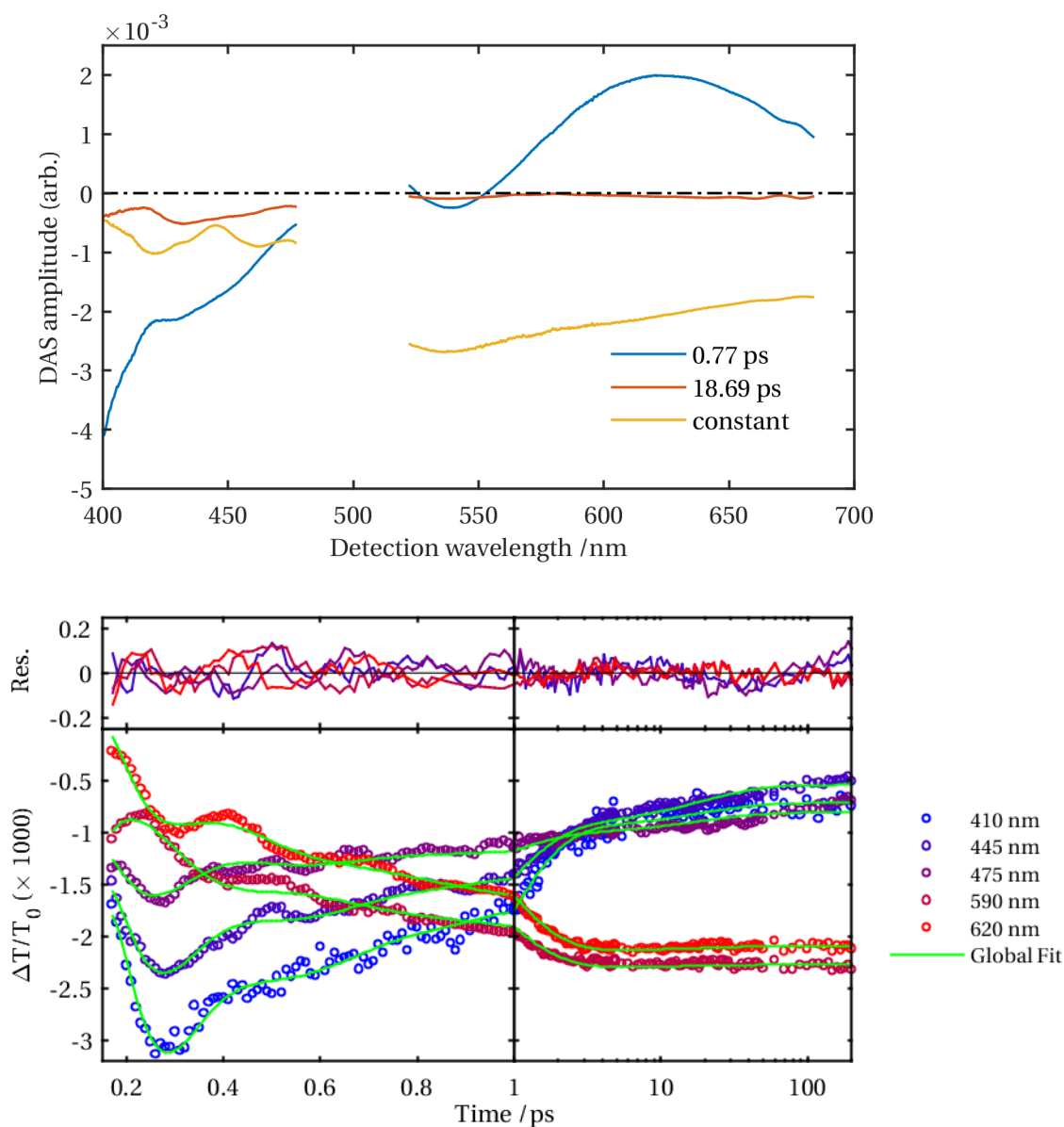


Figure 5.4 – (top) A global fit of the magic angle data (400 to 680 nm, excluding the pump wavelength region) and delay times < 0.15 ps, reveals three decay associated spectra. (bottom) The fit agrees reasonably well with the time traces, as seen by the residuals, however some deviations during the first picosecond and between 10 and 100 ps below 500 nm are observed. The residual at 410 nm has a larger spread around 0 and has been omitted for clarity.

0.77 ps DAS has a broad positive band centered at 625 nm and a small negative contribution at 535 nm. The constant component is negative with increasing amplitude for decreasing wavelengths with a minimum at 535 nm.

Table 5.1 – Summary of extracted time constants.

	τ_1 (ps)	τ_2 (ps)	τ_3 (ps)	$\tilde{\nu}$ (cm ⁻¹)	τ_{deph} (ps)
DAS	0.77	18.69	∞		
SAS	0.74		∞		
SVD	0.87 (decay)	0.66 (rise)			
osc ₁				103	380
osc ₂				130	210

We also perform global fits using the Optimus software [153], which can fit the kinetics and the coherent artifact, but lacks the possibility to fit oscillations of the signal. The results qualitatively agree with the description above and in addition we extract the **species associated spectra** (SAS) using a sequential model with two species (SI, Figure 5.10, top). The SAS with a sub-1 ps decay time constant of has three, negative bands centered at 550 nm (width:~60 nm), and to the blue and red side of the detection wavelength region. It evolves into a constant SAS (within the temporal window of the measurement) with two negative bands below 500 nm and a broad, negative, and featureless band between 500 nm and 700 nm, again with a minimum at 535 nm. SI Figure 5.10 (bottom) shows the spectra associated with the first two **singular values** of a singular value decomposition (SVD) in the 500 nm to 700 nm region only, using the KOALA software [154]. The decaying component of the SVD analysis (blue line in SI, Figure 5.10, bottom) has a negative- and a positive band, which disappear with a time constant of 0.87 ps, while the rising component (red line in SI, Figure 5.10, bottom) only has a negative contribution and appears with a similar time constant. The spectral region below 500 nm has been excluded from the SVD analysis, since it is less easily described. While all data analysis approaches reproduce the experimental data reasonably well, we note that they suggest quite different dynamics, which will be topic of the discussion.

With the information from the TA measurement we cannot confirm or dismiss the 150fs ISC time constant reported by Chen and co-workers [118], since it is faster than our temporal resolution and falls within the strong coherent artifact.

5.5.2 Transient absorption anisotropy

Figure 5.5 shows the TA measurements with parallel (top) and perpendicular (bottom) relative polarizations and Figure 5.6 shows the transient anisotropy of Ptpy that is calculated according to

$$r(\lambda, t) = \frac{I_{\parallel}(\lambda, t) - I_{\perp}(\lambda, t)}{I_{\parallel}(\lambda, t) + 2I_{\perp}(\lambda, t)}, \quad (5.1)$$

where the signal intensity I depends on the wavelength λ and time t . Note that the values do not fall within the expected range of -0.2 to 0.4. This can be rationalized by the fact that, according to

$$r = \frac{\Delta T_{\text{GSB}}}{\Delta T} r_{\text{GSB}} + \frac{\Delta T_{\text{ESA}}}{\Delta T} r_{\text{ESA}} + \frac{\Delta T_{\text{SE}}}{\Delta T} r_{\text{SE}}, \quad (5.2)$$

the transient anisotropy of each spectral feature is scaled by the features in the transient spectrum divided by the total transient [37], which is negative over the entire detection wavelength region and temporal window. We set $I \equiv \Delta T$ since we plot changes in transmission throughout this work. This implies that the denominators in Equation (5.2) are negative and thus the contributions of GSB and SE features to the total anisotropy signal are negative, since ΔT_{GSB} and ΔT_{SE} are positive. The anisotropy of an ESA however contributes with a positive sign to the total transient anisotropy. As an example, let us consider the GSB. Since the pumped- and probed transition dipole moments are necessarily parallel, the anisotropy of a GSB signal is 0.4. Were the GSB feature isolated in the transient data ($\Delta T_{\text{GSB}} = \Delta T$) we would indeed obtain $\frac{\Delta T_{\text{GSB}}}{\Delta T} \times r_{\text{GSB}} = 1 \times 0.4 = 0.4$. However, since $\Delta T < 0$, the observed anisotropy in the GSB spectral region is negative. In additions, since the anisotropy is the sum of the GSB, SE, and ESA components and all of these contributions overlap spectrally, we do not observe an intuitive broadband transient anisotropy signal. It is still possible though to analyze the transient anisotropy in detail in order to obtain useful information about the kinetics of Ptpy. Similar to the procedure above, the transient anisotropy spectrum can be separated into two wavelength regions. **Below 500 nm** the anisotropy shows two negative bands at 447 nm and 475 nm, whose temporal evolution is shown in Figure 5.6 (bottom). During the first ~10 ps the anisotropy at 447 nm and 475 nm (and generally below 500 nm) increases from -0.1 and -0.4

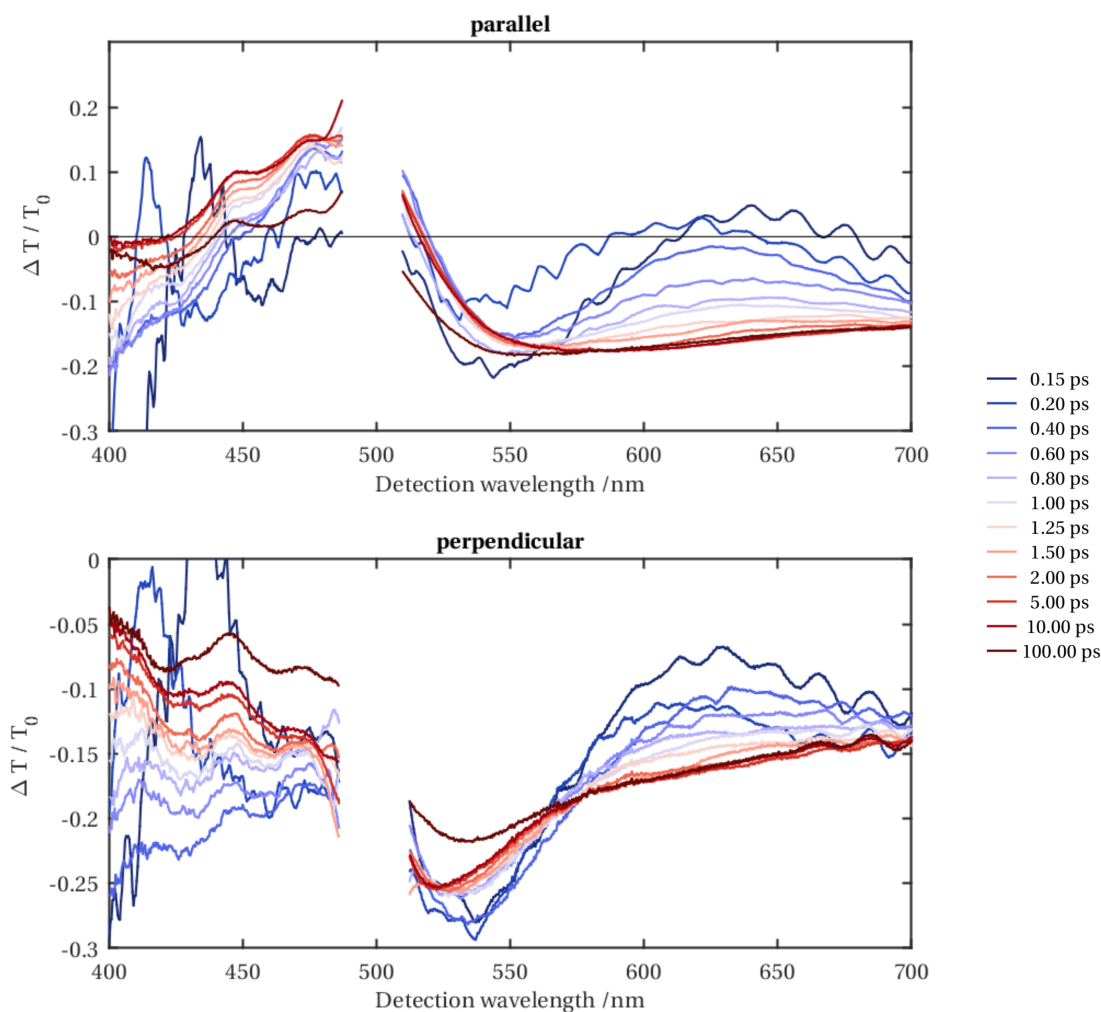


Figure 5.5 – Transient spectra under parallel (top) and perpendicular (bottom) relative polarization of pump and probe pulses at selected time delays. The pump wavelength region has been omitted for clarity and the narrow, positive-going peaks below 450 nm are due to the coherent artifact.

to -0.8. Subsequently, it decays on a time scale of tens of ps. Note that in this spectral region we also observe a slow decay of the magic angle TA signal. Additionally, during the first ps the anisotropy shows coherent oscillations with a period of 0.15 ps ($\tilde{\nu} \approx 220 \text{ cm}^{-1}$), from visual inspection. **Above 500 nm** the transient anisotropy (Figure 5.6, top) features a single, ~ 50 nm broad band centered at 620 nm that decays from a value of -0.2 (at 150 fs) to 0 within 1 ps. At earlier times, the anisotropy is larger (-0.4), but overlapped and modulated by a combination of the coherent artifact and the observed coherences. The evolution of the anisotropy in this spectral region is shown representatively at 510, 535, 640 nm in Figure 5.6 (bottom). It shows

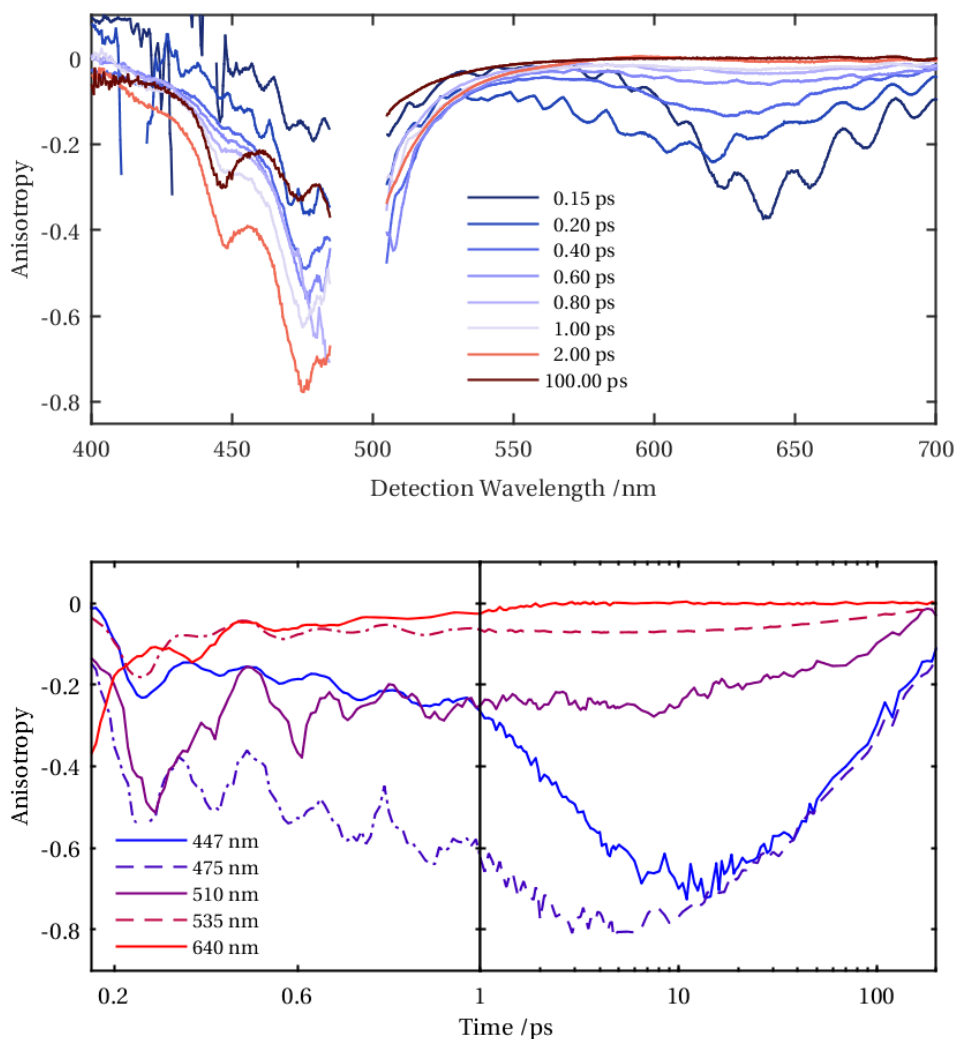


Figure 5.6 – (top) Broadband transient anisotropy of Ptpy excited at 500 nm. The pump wavelength region is omitted for clarity. (bottom) Temporal evolution of the anisotropy at selected wavelengths. See text for details.

coherent oscillation during the first picosecond with a period of approx. 0.15 ps ($\tilde{\nu} \approx 220 \text{ cm}^{-1}$), similar to the wavelength region below 500 nm. Finally, while the anisotropy behaves very different across the detection wavelength region before 10 ps, the decay to 0 from 10 ps to 200 ps seems to be a common feature across the detection wavelength region. This is likely due to the rotation of the molecules and a back-of-the-envelope calculation indeed shows that the rotational diffusion time constant

$$t_R = \frac{1}{6D_R} = \frac{\eta V}{k_B T} \quad (5.3)$$

for a molecule with a hydrodynamic radius of approx. 6-7 Å in toluene (viscosity: 0.59 cP) lies between 130 and 200 ps. Here, η is the solvent viscosity, $V = \frac{4}{3}\pi r^3$ is the hydrodynamic volume of the solute, k_B is the Boltzmann constant, $T = 295$ K, and D_R is the rotational diffusion coefficient of spherical molecule [41].

So far we used transient absorption spectroscopy to study the non-equilibrium dynamics of Ptpy upon optical excitation of its MMLCT band. The anisotropy of the transient signal allows us to tentatively assign the sub-ps evolution of the signal between 580 and 700 nm to the decay of a positive-going band instead of the appearance of a negative signal. Our hypothesis is tested by fluorescence up-conversion experiments in collaboration with the Temps group at the Christian-Albrecht University of Kiel, which are described hereafter.

5.5.3 Transient fluorescence up-conversion

Figure 5.7 shows FIUPS measurements at various detection wavelengths after excitation at 480 nm. At a detection wavelength of 550 nm the signal is dominated by the impulsive Raman response of the solvent whereas at longer wavelengths we observe the decay of the fluorescence. The measured signal intensity depends on the fluorescence intensity, as well as the detection efficiency, which is a combination of the up-conversion process, as well as the spectral efficiency of the monochromator and cannot easily be corrected for. As a consequence, the spectral maximum of the sub-ps fluorescence, which is found between 590 and 610 nm, does not necessarily coincide with the 'real' transient fluorescence maximum. However, we note that the maximum clearly falls between the spectral maxima of the absorption at 500 nm and the long-lived phosphorescence at 662 - 672 nm. Single color FIUPS traces are fit by the convolution of two exponential functions with a Gaussian IRF and the results are summarized in SI Table 5.2. An impulsive decay (A_1 and τ_1) is observed below 580 nm and accounts for the impulsive Raman response of the solvent. The sub-ps decay (A_2 and τ_2) is observed at all detection wavelengths, peaks around 600 nm, and decays with longer time constants for longer wavelengths. A few-ps component with low amplitude appears at wavelengths greater than 590 nm. The width of the IRF is approx. constant with $\sigma \approx 115$ fs for all detection wavelengths.

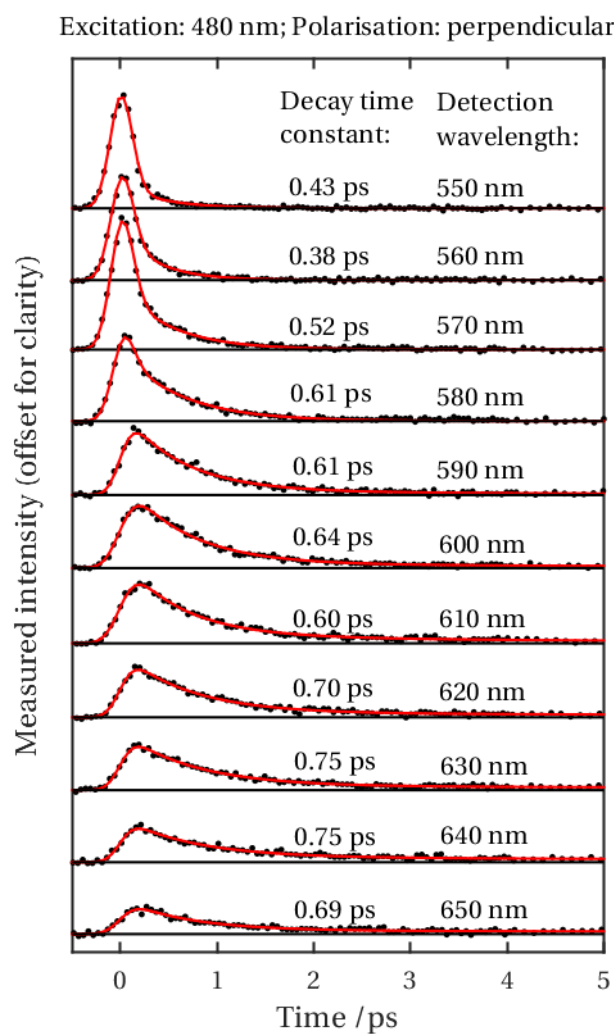


Figure 5.7 – Fluorescence up-conversion signal monochromatically detected between 550 nm and 650 nm in steps of 10 nm under perpendicular polarization conditions. The time constants for the sub-ps decay increase with increasing detection wavelength (Standard error: 20 - 50 fs). A second exponential decay with time constants of a few tens of ps is required for fitting the data, but its amplitude is low. See text for details.

5.6 Discussion

To understand the non-equilibrium dynamics of Ptpy it is instructive to (i) discern between the various components that contribute to the transient signal. It is then possible to (ii) identify the origin of the observed coherences and (iii) propose a mechanistic picture of the dynamics in Ptpy.

(i) Assignment of spectral features Although the TA signal is negative it is possible to discern different contributions to the total signal. The **400 to 500 nm region** shows two distinct positive-going peaks at wavelengths corresponding to the linear absorption bands and a third peak at 499 nm is obscured by the strong pump scatter around 500 nm. TA measurements at parallel relative polarization between pump- and probe pulses (Figure 5.5, left) show positive bands at these spectral positions, which can be rationalized by the fact that GSB signals are enhanced, since the excited- and probed transition dipole moments are necessarily parallel. The overlapping ESA contribution has only slightly more amplitude than the GSB, resulting in a weak negative TA signal that decays biexponentially with sub-1 ps and 20 ps time constants. The remaining ESA is still more intense than the GSB and remains constant over the 250 ps time window of the experiment. In the **500 to 700 nm region** a complex behavior with exponential- and oscillatory components is observed. Brown et al. [119] interpret the kinetics in this spectral region as being due to IC and VR within the triplet state manifold after an initial and ultrafast (≤ 150 fs) ISC, which they cannot resolve temporally. A follow-up study by Kim et al. with 30 fs temporal resolution fails to capture a distinct spectral signature of the 150 fs ISC as well, due to the strong coherent artifact, as well as the coherences within the first 100 - 150 fs [122]. For comparison, the longest probe wavelength in ref. [122] is 560 nm and time delays before 350 fs are omitted. Based on the analysis of our TA and TAA measurements we tentatively assign the transient signal with a 0.6-1 ps time constant and centered around 625 - 650 nm to SE from a *singlet* electronic state, i.e. it manifests itself as a positive-going, decaying signal, overlapped by a broad negative ESA that is present at all delay times. This assignment is confirmed by FIUPS measurements showing the **sub-ps decay of the fluorescence in the 550 to 650 nm region**. The maximum of the transient fluorescence signal is found between 590 and 620 nm, notably between the absorption and phosphorescence bands. The decay time constant increases with

increasing wavelength from 0.5 to 0.7 ps, which is not matched by a corresponding rise of the fluorescence signal in the red-most fluorescence traces (cf. Figure 5.11), but is accompanied by a shift of the respective TA feature between 560 nm and 610 nm (cf. Figure 5.3). This behavior can hypothetically be attributed to the cooling of vibrational modes on the S_1 state.

Additional insight into the kinetics of Ptpy can be gained from preliminary time-dependent density functional theory (TDDFT) calculations (R. A. Ingle, EPFL). Linear interpolations in internal coordinates (LIIC) between the S_0/S_1 geometries, shown in SI, Figure 5.13, indicate that the electronic character between S_1 and T_1 is similar, but differs between S_1 and T_2 . Since the ISC has to be accompanied by a change of orbital angular momentum, it is likely that the ISC happens between the S_1 and T_2 state, rather than the S_1 and T_1 state.

(ii) Origin of coherences Based on the assignment of the transient spectral features, we conclude that the coherences in the TA measurements with 103 cm^{-1} at 550 nm and 130 cm^{-1} at 640 nm are due to the ground- and excited state dynamics of Ptpy, respectively. The higher frequency in the excited state is due to the increase of the Pt-Pt bond order and the associated stiffness of the Pt-Pt vibrational mode upon optical excitation, similar to the case of Pt (pop) [30–32]. We note that the FIUPS measurements do not show any coherences, which might be due to the lack of temporal resolution. The coherences observed in the TAA has a dominant period of 0.15 ps ($\tilde{\nu} = 220\text{ cm}^{-1}$), corresponding to the Raman mode of toluene, which is also observed under parallel- and perpendicular relative pump-probe polarization in an auxiliary solvent-only measurement shown in SI, Figure 5.12. It averages out at MA, but not in the anisotropy, due to the term $I_{\parallel} - I_{\perp}$.

(iii) Current understanding of the non-equilibrium dynamics of Ptpy Upon 480 - 500 nm excitation of the MMLCT transition an electron is transferred from an anti-bonding Pt-Pt orbital to a ligand centered orbital. The 0.5 - 0.8 ps decay of the initial singlet ESA and SE signals, concomitant with the decay of the transient fluorescence signal, is due to ISC, while the expected rise of the triplet ESA signal is masked by the overlapping GSB, singlet- and triplet ESA, and SE contributions. Vibrational coherences in the ground- and excited electronic states are damped out within 0.2 - 0.4 ps, due to the flexibility of Ptpy, since

compared to Pt(pop), Ptpy is only linked by two tBu₂pz groups. Together with the additional conformational degrees of freedom of the ppy ligands, this structural ‘flexibility’ results in an efficient redistribution of vibrational energy, and the loss of the system’s vibrational coherence. The only observable evolution of the triplet ESA is a small 20 ps contribution below 500 nm, which might be associated to an IC within the triplet manifold of states. However, currently this assignment is only tentative.

5.7 Summary and outlook

Using TA and TA anisotropy in conjunction with fluorescence up-conversion, we provide a consistent analysis of the transient spectral features of Ptpy upon optical excitation of the MMLCT transition. Using complementary TDDFT calculations we conclude that the initially excited S₁ state undergoes ISC from the S₁ to the triplet manifold of states with a time constant of 0.5 to 1 ps (Figure 5.8). Vibrational coherences in the ground- and excited state are associated with the periodic modulation of the Pt-Pt distance and are damped out within a few hundred femtoseconds, due to the flexibility of Ptpy. In depth comparison of the experimental data to TDDFT calculations will reveal additional details of the relaxation pathways and help assess the interplay between the molecule’s electronic and structural degrees of freedom.

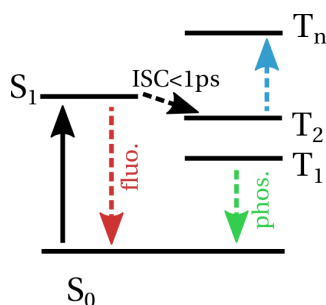


Figure 5.8 – Hypothetical microscopic picture of the energy relaxation in Ptpy.

5.8 Supplementary information

Close-up of the coherences observed in the MA transient absorption

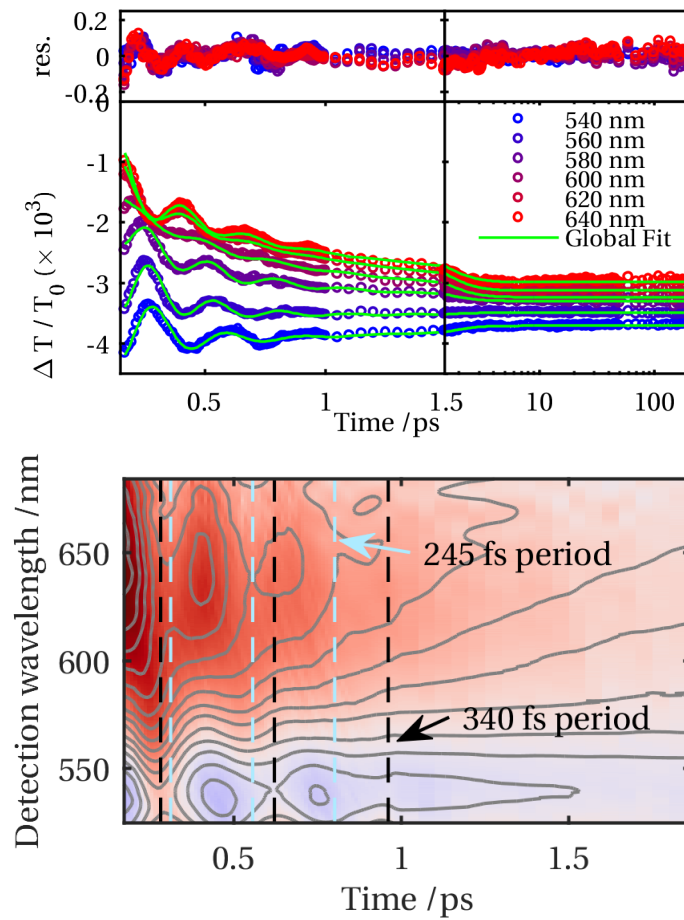


Figure 5.9 – (top) Time traces of the transient signal fitted by a sum of three exponential decays and two damped oscillations. The upper panel shows the residuals of the fit. (bottom) Subtracting the > 10 ps kinetic component highlights the oscillations during the first ps. The vertical lines indicate the periods of the two oscillatory functions that are used to fit the data. For details see text.

Alternative models to fit the TA data

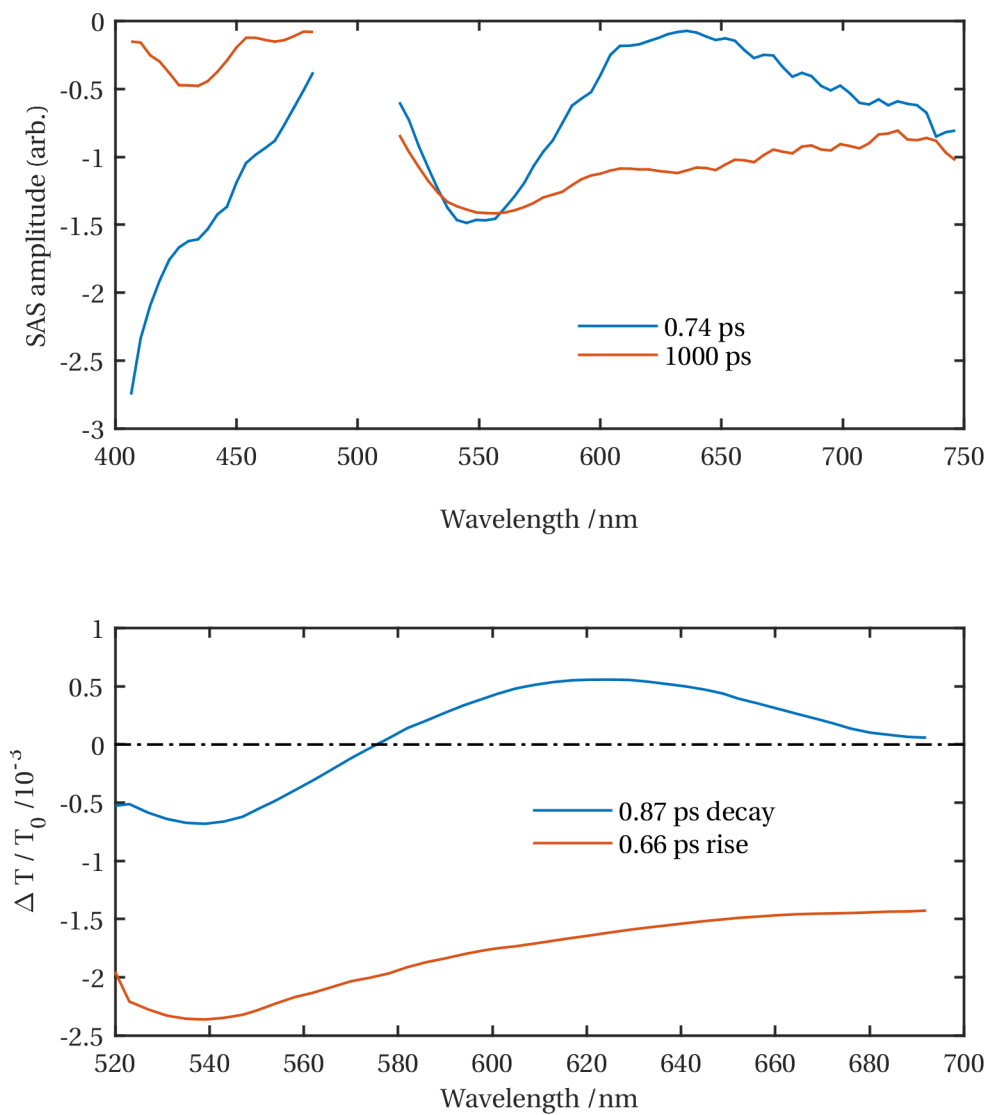


Figure 5.10 – (top) Species associated spectra and (bottom) SVD components of the MA transient of Ptppy in the 500 to 700 nm region.

Wavelength-dependent fluorescence decay time constant

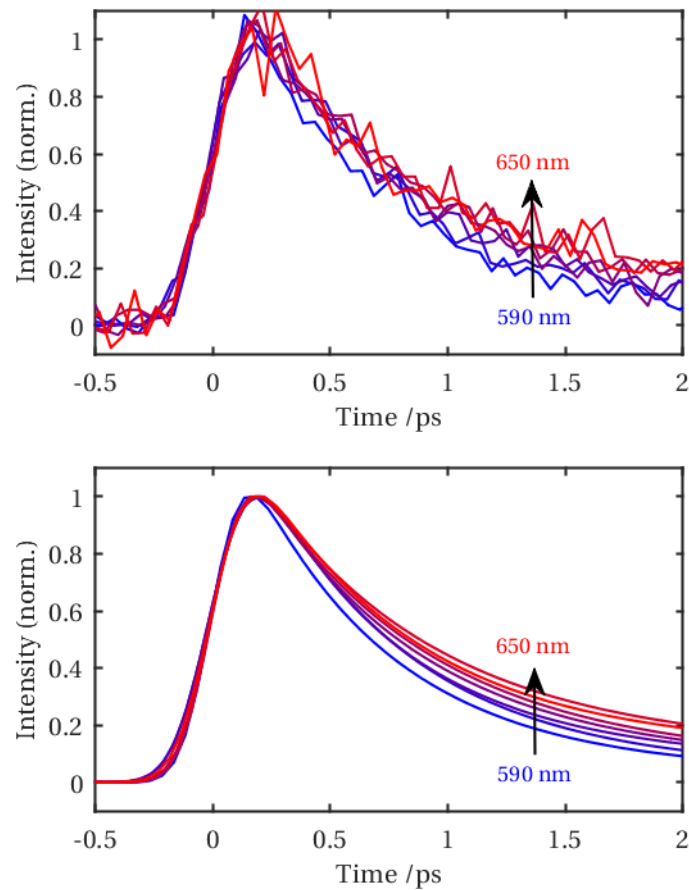


Figure 5.11 – (top) Fluorescence up-conversion data and (bottom) fits of the data with detection wavelength varying from 590 nm to 650 nm in 10 nm steps. The increase in the decay time constant for increasing wavelength is not accompanied by an additional rise of the signal, but by a shift of the respective TA feature.

Table 5.2 – Results of fitting the single wavelength FIUPS data. The IRF is described by its standard deviation σ and time zero position t_0 . Exponential functions 1 to 3 with amplitude A_n and decay constants τ_n describe the impulse, sub-ps, and few picosecond signal decay, respectively.

Wavelength [nm]	IRF σ [ps]	IRF t_0 [ps]	A_1	τ_1 [ps]	A_2	τ_2 [ps]	A_3	τ_3 [ps]
550	0.115	0.27	3.50E+04	0.003	61.5	0.429		
560	0.117	0.243	1.00E+04	0.006	126	0.376		
570	0.116	0.242	1.60E+04	0.005	164	0.522		
580	0.111	0.209	4.90E+03	0.007	188	0.612		
590	0.103	0.116			223	0.608	10.2	5.31
600	0.13	0.172			236	0.644	10.7	8.49
610	0.13	0.204			212	0.598	21	4.79
620	0.112	0.153			165	0.704	10.9	13.8
630	0.112	0.162			148	0.748	9.5	27.2
640	0.109	0.141			107	0.753	12.7	14.3
650	0.122	0.133			84.6	0.692	8.66	28.9

Coherent oscillations of toluene in the TAA measurements

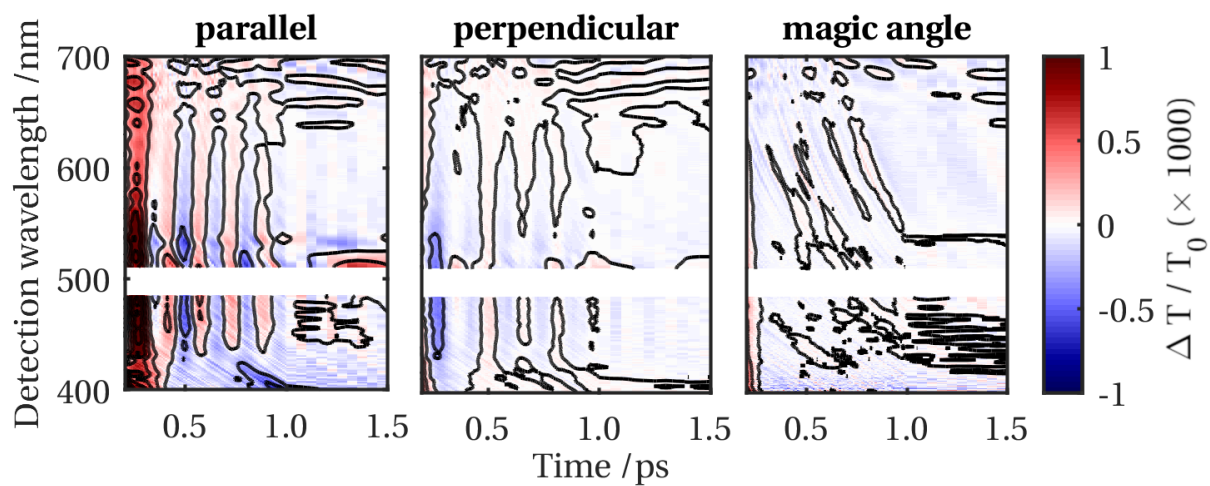


Figure 5.12 – TA response of toluene with parallel, perpendicular, and magic angle relative pump-probe polarization, showing a coherent oscillations with 215 cm^{-1} (Raman mode at 217 cm^{-1} [149]).

Preliminary results from TDDFT

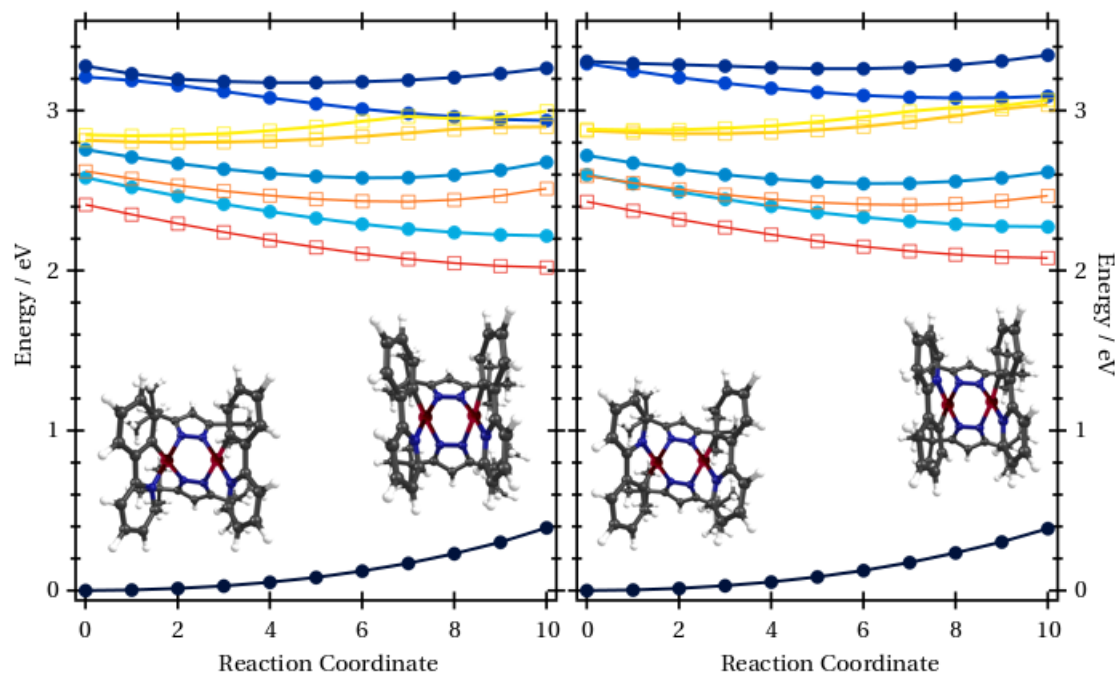


Figure 5.13 – Linear interpolations in internal coordinates (LIIC) between the S_0/S_1 minimum energy geometries for the cis (left) and trans (right) isomers of Ptpy. The geometries shown represent the initial and final points of each LIIC. The filled circles denote singlet states and the open squares denote triplets. Excited-state energies were calculated at each point on the LIIC at the TDDFT/PBE0 level of theory within the Tamm-Dancoff approximation. For the light elements, a 6-31G(d) basis set was used and a LAN2DZ ECP and basis set on the platinum atoms.

6 Multidimensional electronic spectroscopy of Nile blue

6.1 Background

Two-dimensional coherent spectroscopy has proved to yield insight into molecular- and solid-state dynamics beyond the possibilities of transient absorption spectroscopy, by adding the excitation frequency dimension, while maintaining the highest possible time resolution. In the visible the latter is often on the order of 10 fs or less – theoretically sufficient to capture even the fastest molecular dynamics (H₂ stretch: 7.5 - 8 fs) [155]. On the one hand, this opens the possibility to study the dynamics of molecular motion as part of a reaction mechanism in great detail. On the other, it poses the experimental and theoretical challenge to disentangle the observed signal (a mix of nuclear and electronic coherences, as well as electronic relaxations) and identify the origin of each component. One aspect is that, since the observable is often a change in transmission, the total signal is a mix of ground state- (GSB) and excited state (SE and ESA) signals and any observed coherence can thus be in the ground state (initiated via an impulsive Raman process) or in the excited state (initiated via an absorption). Though sometimes their origin can be clearly identified, the more general case is that spectral signatures of ground- and excited states strongly overlap. Another aspect is to differentiate between vibrational and electronic coherences, a coherent behavior of two or more electronic states, both of which can be observed by time-domain techniques. The fundamental, underlying question is to understand the coupling between vibrational and electronic degrees of freedom, or differently speaking the coupling of electronic relaxation pathways to vibrational motions

Chapter 6. Multidimensional electronic spectroscopy of Nile blue

of the system, which can have substantial influence on chemical or biological functionality, e.g. in artificial light-harvesting [55–57, 156], vision [157–159], or photosynthesis [160–163]. The latter brings us back to the previous chapter of this thesis and the question about the connection between excited state potential energy surfaces and vibrational coherences.

In this work we study Nile blue (nb), a commonly used test molecule for transient absorption- [100, 164–166] and two-dimensional spectroscopy [47, 167, 168], as it has a strong absorption cross section, rather simple kinetics and few characteristic vibrational frequencies. In addition, it has been studied thoroughly by experimental [101, 102, 169] and theoretical [72, 170] research groups to understand its photophysical properties, such as the strong solvent dependence of its absorption and fluorescence spectrum. In addition nb is pH sensitive, can be modified to bind as a fluorescent marker to specific receptors and can be used as a photosensitizer. These properties make nb and similar molecular dyes interesting for applications in fluorescence labeling and cell biology [171–173], Förster resonance energy transfer measurements [174], super-resolution microscopy [175], photo-sensitization of DNA bases to study lesions and DNA repair mechanisms [176–178]. Multipulse excitation has been used to selectively excite molecular modes of nb and enhance population transfer [179], exploring the possibilities of coherently controlled chemistry [180–183].

Recently, Kukura and co-workers used nb and rhodamine 101 as test systems for their broadband impulsive vibrational spectroscopy experiment and found that a shift of the vibrational frequencies under off- and on-resonant pumping conditions can be used to discern between ground and excited state vibrational coherences [166]. Their hypothesis is that an off-resonant pump will mainly excite ground state vibrations via an off-resonant Raman process, while an on-resonant pump will generate excited state vibrational coherence via absorption. These findings will become relevant, when examining the beatings observed in the 2D spectra of nb.

In this thesis, I use nb to benchmark our 2D experiment, but beyond, I find that the beating of different vibrational frequencies may yield insight into the molecular dynamics of the system, specifically the distinction between ground- and excited state dynamics. These findings are analyzed in detail to elucidate the capabilities of 2D spectroscopy to determine the origin of vibrational coherences.

6.2 Coherences in the ground- and excited state measured in the time-domain

Vibrational levels in the electronic ground state can be conveniently and accurately measured by frequency-domain Raman- and infrared spectroscopy, offering insight into the equilibrium structural dynamics of the system and the topography (though only close to the equilibrium position) of its ground state potential energy surface (PES). In addition to frequency and amplitude information, time-domain spectroscopy yields the phase differences and dephasing times of a system's vibrational motions in the ground- *and* the excited electronic states. This is achieved by monitoring the evolution of vibrational wavepackets, which are initiated by the coherent excitation of several vibrational levels, or via instantaneous structural changes of the system [50, 51] and can be of any mode slower than twice the laser pulse duration, e.g. $\sim 2800\text{ cm}^{-1}$ (12 fs period) for a 6 fs pulse. These information help understand the topography of the ground- and excited PESs, the interaction of the system with a bath, and the coupling between nuclear and electronic degrees of freedom. Typically a laser pulse creates a large number of ground- and excited state vibrational coherences, which can be difficult to disentangle experimentally. In addition, the coherent excitation of several electronic states can lead to *electronic wavepackets*, superpositions of electronic states, which are fundamentally different from vibrational coherences. Again it is often less than trivial to identify the different contributions in an experiment. To make things even more complex, vibrational motion in the excited electronic state is often linked to a change of the equilibrium distance along the reaction coordinate, essentially mixing electronic and nuclear degrees of freedom, in which case we speak of a vibronic (vibrational-electronic) behavior. In many cases it is advantageous to consider simple model systems, such as the displaced oscillator (DO) and electronic dimer (ED) shown in Figure 6.1, to understand the various signals that can be observed in time-domain spectroscopy. Briefly, the DO model describes a single system whose electronic states are coupled to one vibrational mode, leading to a vibrational level structure. The ED model features two excited electronic states that are coupled via a common ground state. If the vibrational energy gap of the DO matches the electronic energy gap between the excited states of the ED, the two scenarios can hardly be discerned using linear spectroscopy [63]. This is exemplified in Figure 6.1 (right). Multidimensional coherent spectroscopy is a tool

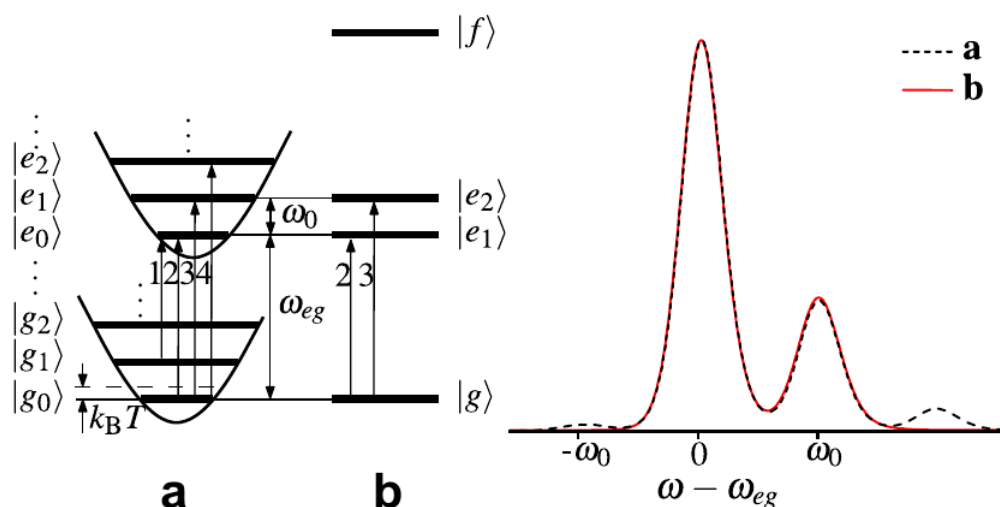


Figure 6.1 – Comparison between (a) the displaced oscillator- and (b) the electronic dimer model. The first two bands of the linear absorption spectrum are identical, making it difficult to differentiate between these very different microscopic situations. Reprinted from ref. [63], copyright 2012, with permission from Elsevier.

to dissect the macroscopic temporal response of a system via the excitation and detection frequency dependence of the coherences, the possibility to distinguish between rephasing and non-rephasing Liouville pathways [63, 65, 184, 185], and the distinction between positive- and negative coherence frequencies [54, 74]. It can thus be used to differentiate between different microscopic pictures, e.g. DO or ED systems. Often scenarios arise in which the two situations mix, requiring a combined, vibronic dimer model [53, 65, 186, 187], and the fundamental question “how vibrations interfere with electronic coherences” [63] remains a driving force in the field of coherent spectroscopy.

6.3 Sample characterization and photophysics

nb was purchased from Sigma Aldrich and dissolved in spectroscopic grade ethanol. The concentration was adjusted to achieve an optical density between 0.1 and 0.3 for all optical measurements, i.e. inside a 1 cm cuvette for static absorption measurements and inside a 100 μm cuvette for time-resolved experiments. Figure 6.2 (left) shows the absorption- and emission spectrum of nb in ethanol with the absorption maximum at 629 nm, corresponding to a $\pi\text{-}\pi^*$ electronic transition. The emission maximum is centered at 661 nm and the Stokes

6.3. Sample characterization and photophysics

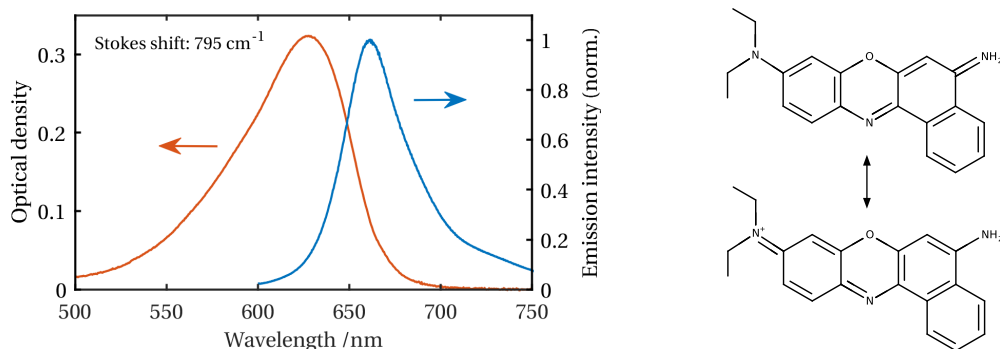


Figure 6.2 – (left) Visible absorption spectrum of nb. The main peak at 626 nm is vibrationally broadened by coupling of the electronic transition to a large number of Raman active modes, which are dominated by modes at 593 cm⁻¹ and 1640 cm⁻¹, according to ref. [101]. (right) Resonance structure of nb, showing the delocalization of the positive charge. Depending on the solvent properties, the ground state character will be predominantly one of the two resonance structures [169].

shift is 795 cm⁻¹. Marazzi et al. [170] calculated vertical excitation energies at the TDDFT / CASPT2 levels with both a water polarizable continuum model (PCM) and explicit solvent to show that the positive charge is transferred from the -NH₂ group (94 % in S₀) to the -N(Et)₂ group (22 % at FC). The interaction between nb and ethanol is comparable to water, since both are protic solvents and the normalized solvent polarity (normalized to water) of ethanol is 0.65 [169, 188]. In general the transition energy depends on the ground and excited state properties, as shown by [170], and thus the interaction with nearby counterions or solvent molecules [169] leads to strongly solvent/environment dependent optical properties. Aprotic solvents with low normalized polarity lead to a blue shift of the absorption band and an increase of the Stokes shift. The latter differs strongly in solvents with high polarity (~780 cm⁻¹), low polarity (~2800 cm⁻¹), and in gas-phase (~1300 cm⁻¹) [169].

The absorption band is vibronically broadened due to the coupling of the electronic transition to Raman-active vibrational modes of the molecule [101] and early femtosecond TA spectra have been modeled by a two-level system of displaced harmonic oscillators with a vibrational frequency of ~590 cm⁻¹ [100]. Note that the exact frequency is solvent dependent, which is why slightly different numbers appear throughout the literature and in this thesis. This simple model, in which the ground- and excited state wavepackets oscillate with the same frequency, reproduces the broadband TA data, which shows how the excited state wavepacket oscillates

between the Frank-Condon point and longer wavelength (650 – 800 nm), while the ground state wavepacket oscillates around the absorption maximum and is shifted by $\pi/2$ [164]. The reported vibrational dephasing time (> 1.5 ps) indicates an inefficient dephasing mechanism for the 590 cm^{-1} mode [100], justifying the assumption of harmonic PESs. The origin of the 593 cm^{-1} peak in the Raman spectrum of nb in ethanol has been assigned to a ring-breathing mode and the second prominent peak at 1647 cm^{-1} to a deformation of the NH_2 group [101, 102]. The 1300 cm^{-1} Stokes shift of the isolated molecule reveals an energy relaxation of two vibrational quanta of the 596 cm^{-1} breathing mode between the absorption (Frank-Condon point) and the emission [169]. Early two-pulse photon echo experiments show that the pure, electronic dephasing time is on the order of 60 fs [165].

6.4 Experimental methods

The 2D photon echo (2DPE) experiment has been described in Chapter 4 and is based on a preceding version in our laboratory [86]. Briefly, white light pulses spanning from 450 nm to 950 nm are generated from amplified laser pulses (800 nm, $300\mu\text{J}$, 3 kHz, 30 fs; Coherent Astrella) via self-phase modulation inside a differentially pumped, argon-filled hollow core fiber and are compressed using a set of chirped mirrors (PC70, Ultrafast Innovations) in combination with a pair of fused silica wedges to fine-tune the GVD. The temporal resolution is determined at the sample position by transient grating FROG measured in ethanol (0.1 mm cuvette) and is typically on the order of 10 to 15 fs. 2D experiments are performed in a background-free, passively phase-stabilized BOXCARS geometry using beam splitters to generate \mathbf{k}_{1-3} and \mathbf{k}_{LO} [167] with a phase stability of approx. $\lambda/60$ at 600 nm. \mathbf{k}_{LO} precedes \mathbf{k}_{1-3} in time by ~ 1.8 ps by passing \mathbf{k}_{1-3} through an additional 1 mm of glass. Auxiliary TA measurements are performed under identical conditions, using \mathbf{k}_1 and \mathbf{k}_{LO} as pump and probe beams, respectively. The signal (PE and LO, or the probe for TA) is coupled into a spectrograph (Andor Shamrock 303i) and recorded shot-to-shot using a home-built CCD detector (2048 x 1 pixels, CCD chip: Hamamatsu S11155-2048-02), using a field-programmable gate array (FPGA) for fast readout. Wavelength calibration is performed using an argon gas-discharge lamp and the spectral detection range is 200 nm with a wavelength resolution of 0.5 nm. Subtraction of unwanted scattering background is achieved by chopping \mathbf{k}_1 and \mathbf{k}_2 with $R/2$

and $R/4$, respectively, where R is the repetition rate of the laser, and calculating a background-free signal as $I = (I_1 - I_2 + I_3)/I_4$. I_1 through I_4 are four consecutive acquisitions, where, in order, no beams are blocked (I_1), either \mathbf{k}_1 or \mathbf{k}_2 are blocked (I_2 and I_3), and both \mathbf{k}_1 and \mathbf{k}_2 are blocked. For details see Section 4.6.2. Three to five population time scans of the recorded data $I(\tau, T, \omega_t)$ can be averaged to improve the data quality and I is then treated according to Section 4.8 and the literature [44, 99, 167, and others].

6.5 Results

Figure 6.3 shows the population time evolution of the 2D spectrum of nb during the first 200 fs and at 2 ps. At 2 ps it is dominated by a broad positive (GSB/SE) feature with a maximum at $15800 \text{ cm}^{-1} / 15330 \text{ cm}^{-1}$ (convention: ω_τ / ω_t), in very close agreement with the absorption maximum at $\omega_\tau = 15900 \text{ cm}^{-1}$ and the transient absorption maximum at $\omega_t \approx 15400 \text{ cm}^{-1}$. In ω_τ the 2D spectrum extends from 15000 cm^{-1} to 17500 cm^{-1} and in ω_t from 14000 cm^{-1} to 17500 cm^{-1} , comparable to the width of the absorption spectrum (red line, x-axis), and the TA spectrum (black line, y-axis). We note that the shape of the 2D spectrum reveals a few inaccuracies in the data, mainly the negative signal on the diagonal at 17500 cm^{-1} and below the main feature at $15500 \text{ cm}^{-1} / 14000 \text{ cm}^{-1}$. These are likely due to phase twists from an inaccurate τ_0 calibration or an inaccurate spectral calibration, or both (cf. discussion in Section 4.7 and background on lineshapes in Section 2.3.7). During the first 2 ps the 2D spectrum shows a complex behavior, reflecting the system kinetics and coherences. The temporal evolution in Figure 6.3 qualitatively reveals the broadening of the 2D lineshape, accompanied by a change in the center line slope (CLS), indicated by the signal maximum in the ω_τ dimension (yellow dots). Measurements at negative population times and during the first 30 fs are distorted by double-quantum coherence pathways for the wrong time ordering $\mathbf{k}_2 - \mathbf{k}_3 - \mathbf{k}_1$ [189] and non-resonant interactions with the solvent and the cuvette.

An exemplary time trace at $15850 \text{ cm}^{-1} / 15000 \text{ cm}^{-1}$ is shown in Figure 6.4. The non-oscillatory contributions of each time trace are fitted by a convolution of $N = 1, 2, 3, \dots$ exponential functions¹ with an instrument response function (IRF), approximated by a linear

¹This is the basis for implementation of a global fit routine, which can add vital information to the analysis of molecular- or reaction kinetics.

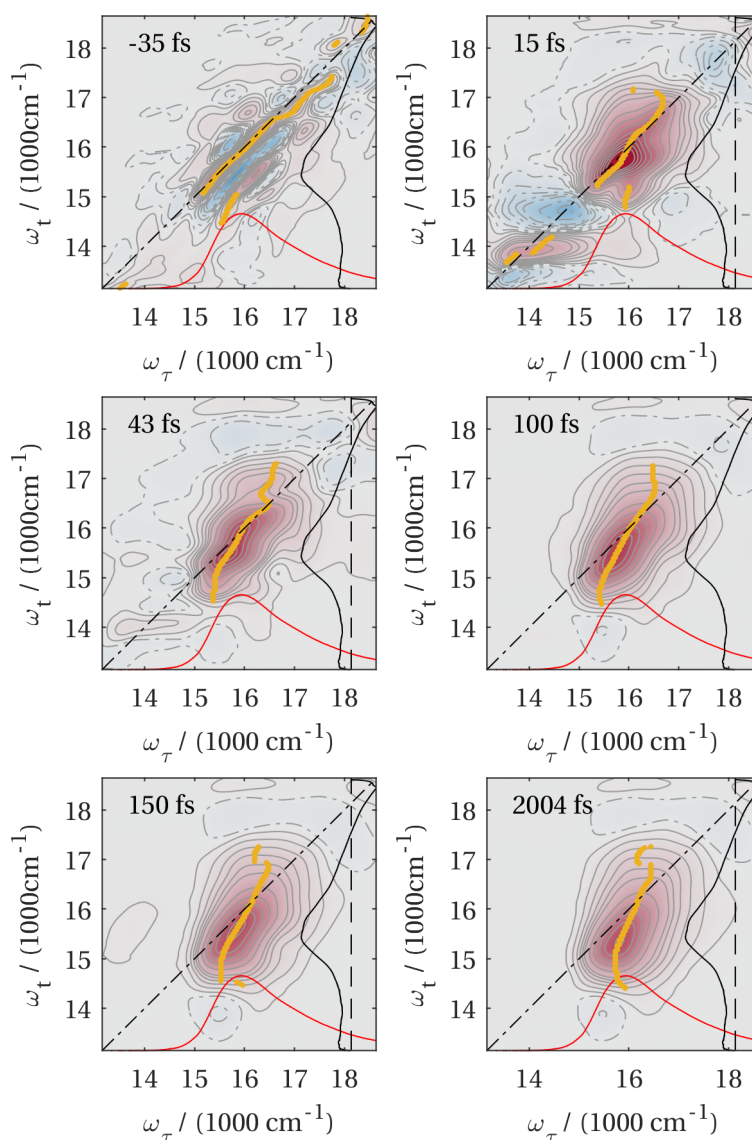


Figure 6.3 – Evolution of the 2D spectrum during the first 200 fs. The absorption- (red line) and TA spectrum (black line) are shown for comparison and the maximum of the signal along ω_t is shown as yellow dots.

combination of a Gaussian and its 1st and 2nd derivatives [153]. Subtraction of the IRF and the exponential kinetics isolates the system coherences as the residual, oscillatory components of the signal. Within the temporal window of a few picoseconds we observe strong coherences, but only negligible contributions from exponential kinetics. Figure 6.5 shows the evolution of the peak position in the ω_t -dimension (blue) and of the peak amplitude in the 2D spectrum (red) – a more global description of the 2D spectrum compared to a single time trace. The

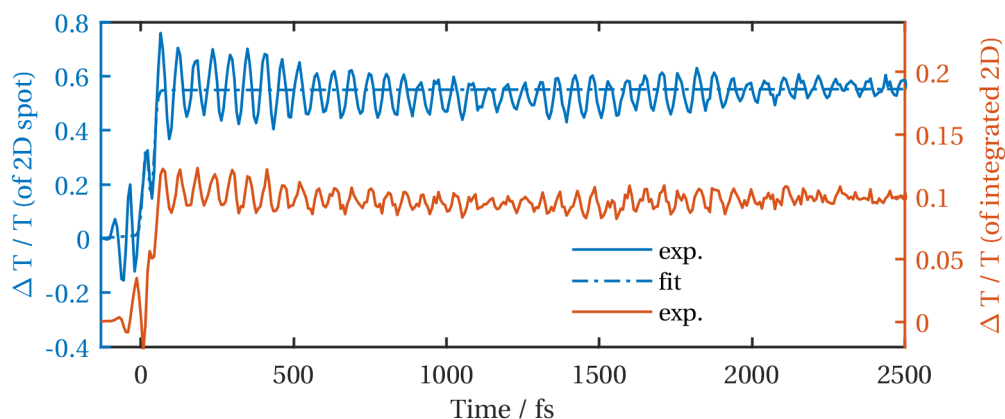


Figure 6.4 – Time traces of $15000\text{ cm}^{-1} / 15850\text{ cm}^{-1}$ spot (blue) and of the integrated signal (red). Oscillations around $T = 0$ are due to pulse overlap and time ordering effects.

peak position along ω_t initially oscillates by $\pm 150\text{ cm}^{-1}$. Over the course of 2 ps it shifts from $\sim 15600\text{ cm}^{-1}$ to 15330 cm^{-1} and the oscillation is damped. In ω_τ the peak position is constant at 15800 cm^{-1} (not shown). The peak amplitude exhibits an initial drop from 1.5 to 0.9 (Figure 6.5, inset), which can be attributed to additional signal strength due to the pulse overlap during the first 20 fs, followed by a slower decrease and oscillations until ~ 2 ps.

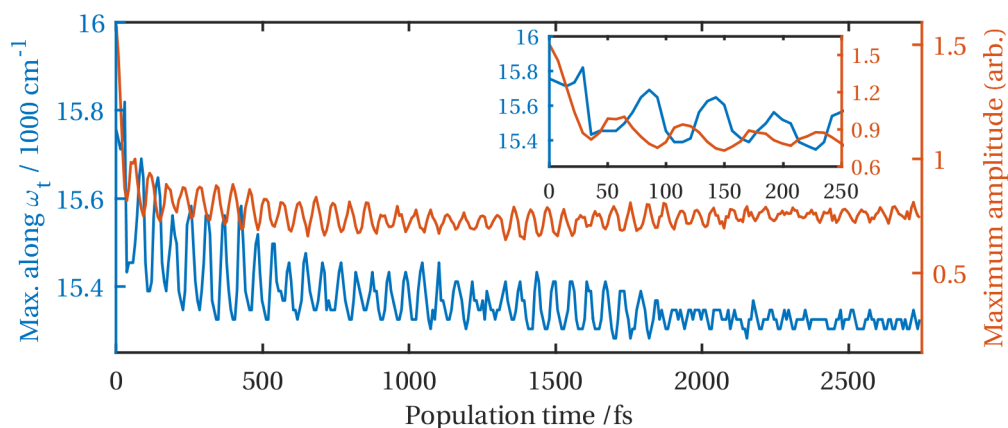


Figure 6.5 – (left, blue) Evolution of the maximum of the 2D spectrum in the ω_t dimension and (right, red) of the maximum amplitude.

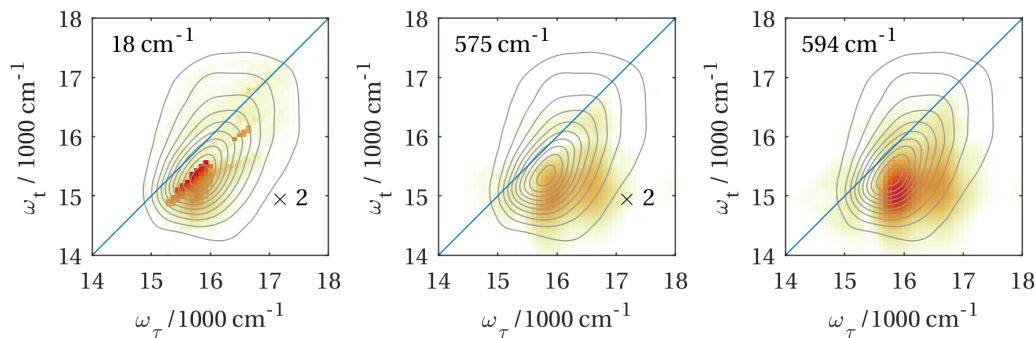


Figure 6.6 – Beating maps at $\Omega_T = 18 \text{ cm}^{-1}$, 575 cm^{-1} , and 594 cm^{-1} . Population time before 20 fs were neglected to avoid artifacts from improper fitting of the IRE. The similarity between the 575 cm^{-1} and 594 cm^{-1} spectra are due to the fact that the 575 cm^{-1} spectrum is in the edge of the 594 cm^{-1} coherence. See Figure 6.7 and text for more details.

All observable spectral features show strong coherent oscillations with a dominant period of 55 to 60 fs ($\tilde{\nu} \approx 550 - 600 \text{ cm}^{-1}$) and reveal *beat nodes*. Fourier transformation of the coherences in the population time dimension ($T \rightarrow \Omega_T$) yields a three-dimensional dataset of the form $I(\omega_\tau, \Omega_T, \omega_t)$, linking the frequency spectrum of the system's Ω_T coherences to the excitation- and detection frequencies. Plotting $I(\omega_\tau, \Omega_T, \omega_t)$ for a coherence frequency of interest thus reveals the excitation- and detection frequency dependence of said coherence. These *beating maps* are shown in Figure 6.6 for the most prominent coherences at 18 cm^{-1} , 575 cm^{-1} , and 594 cm^{-1} . Note that 18 cm^{-1} is the difference between the 575 cm^{-1} and 594 cm^{-1} mode. The width of each frequency peak is $\Delta\Omega_T \approx 10\text{-}20 \text{ cm}^{-1}$ (experimental resolution: $R_{\Omega_T} \approx 6 \text{ cm}^{-1}$), reflecting the dephasing time of approx. 1.5 ps. The observed coherences are located predominantly below the diagonal, i.e. they appear at energies lower than the excitation energy. The 18 cm^{-1} beating map shows a diagonal feature slightly below the diagonal between 15000 and 16000 cm^{-1} that extends to higher ω_τ and lower ω_t . The two strongest coherences with $\Omega_T = 575 \text{ cm}^{-1}$ and 594 cm^{-1} , are centered at $\omega_\tau \approx 15900 \text{ cm}^{-1}$ and 16600 cm^{-1} , respectively, and extend in ω_t from 14500 to 15500 cm^{-1} .

Summing over all excitation and detection frequencies yields a survey frequency spectrum of the coherences, shown in Figure 6.7 (left). Also shown (right) is the Ω_T spectrum at $15850 \text{ cm}^{-1} / 15000 \text{ cm}^{-1}$, the same spot in the 2D spectrum as the time trace in Figure 6.4. Upon closer inspection (Figure 6.7, insets) additional frequencies can be discerned. Generally, the coherence frequency spectrum at a specific combination of ω_τ and ω_t has a better signal-

6.6. Phasing, benchmarking and comparison to the literature

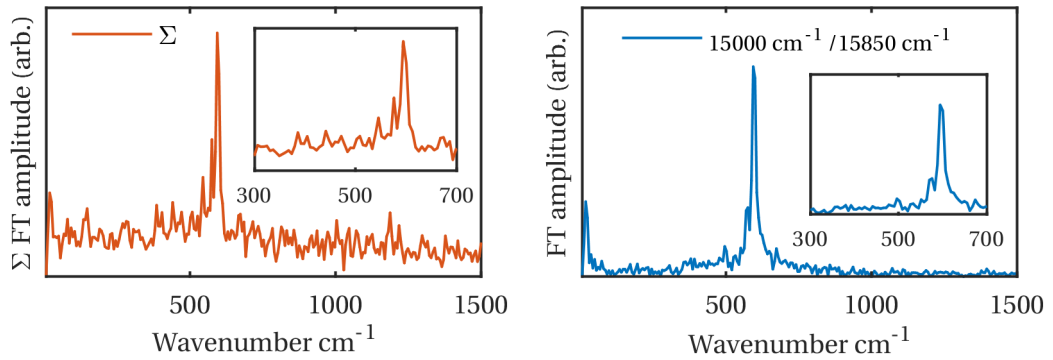


Figure 6.7 – (left) Survey beating spectrum from summing $I(\Omega_T)$ over ω_τ and ω_t and (right) coherence frequency spectrum at $15850 \text{ cm}^{-1} / 15000 \text{ cm}^{-1}$ (ω_τ / ω_t). The beating frequencies of the most prominent coherences are 18 cm^{-1} , 572 cm^{-1} and 596 cm^{-1} , but additional frequencies can be discerned (insets).

to-noise ratio (S/N), since much of the noise is due the summation over signal-free regions and care should be taken when trying to determine whether or not a specific frequency is due to a coherence of the system or due to noise or artifacts from the data treatment.

6.6 Phasing, benchmarking and comparison to the literature

The absorptive 2D spectrum is recovered from the complex² data by multiplication with a phase correction factor and a subsequent Fourier transform $\tau \rightarrow \omega_\tau$. The phase correction accounts for the linear phase difference due to the temporal delay between the signal and the LO pulse, as well as any other phase differences between the signal phase and the LO phase. The phase correction function is found iteratively, by comparing the integrated 2D spectrum (onto the ω_t axis) to an auxiliary transient spectrum at the same population time delay. This procedure is known as ‘phasing’ [44]. To phase our data we minimize the difference between the integrated 2D spectrum and the transient spectrum by adjusting a linear and a constant phase parameter of the phase correction function. We find that in some cases adding a small quadratic phase term improves the quality of the phasing, especially at the extremes of a 2D band, but typically it does not make a significant difference.

²after a first Fourier transform to extract the amplitude and phase information of the measured, real data [190]

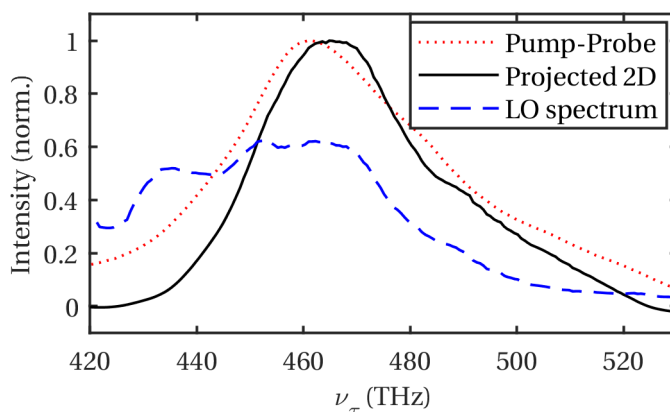


Figure 6.8 – Phasing of the complex 2D data shows a tolerable agreement between the integrated 2D spectrum (black line) and the transient spectrum (red, dotted line) at the same population time delay. The LO spectrum (blue, dashed line) is shown for reference.

Figure 6.8 compares the integrated 2D spectrum (black line) to the transient spectrum (red, dotted line). The LO spectrum (blue, dashed line) is shown for reference. Although the data does not agree perfectly, the integrated 2D spectrum reproduces the overall shape of the transient. We have observed better agreement during the commissioning phase of the experiment, but in those cases we noted other issues, e.g. missing off-diagonal intensity or insufficient temporal resolution, and work is underway to improve this issue.

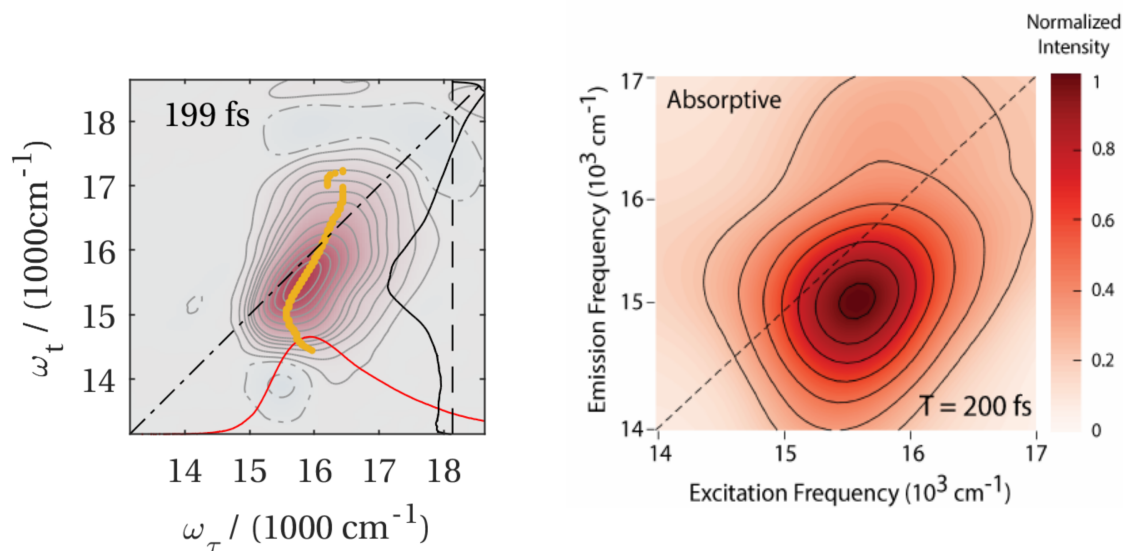


Figure 6.9 – Comparison of (left) our experimental data with (right) Son et al. [47].

To further assess the accuracy of the experiment we compare the 2D spectrum of nb to published data by Schlau-Cohen and co-workers [47, 168], shown in Figure 6.9. We correctly observe the maximum of the 2D signal below the diagonal, corresponding to the spectral position of the linear absorption- and TA spectrum, respectively, similar to ref. [168] (Figure 6.8, bottom).

6.7 Preliminary discussion

The transient 2D signal of nb in Figure 6.3 is a convolution of the GSB and SE signals only, since the ESA is only observed as a weak contribution at $\omega_t \geq 17500 \text{ cm}^{-1}$. While the GSB resembles the steady state absorption spectrum, the SE is redshifted from the absorption maximum by 795 cm^{-1} . The initial elongation of the 2D band shape is attributed to the inhomogeneity due to the varying solvent environment, as well as the fact that energy redistribution between the different vibrational modes has not yet taken place. Within 200 fs the band shape becomes increasingly homogeneous, reflecting the solvent dynamics and the redistribution of vibrational energy.

Inspection of the time trace in Figure 6.4 shows that the molecule exhibits few and strong vibrational coherences interfering destructively at 1.25 ps, and a Fourier transformation reveals three main frequencies at 18 cm^{-1} , 575 cm^{-1} , and 594 cm^{-1} . Raman spectroscopy [101, 102], as well as TA- [100, 164] and 2D spectroscopy [47, 168] previously observed a single strong vibrational coherence with a frequency of 596 cm^{-1} (593 cm^{-1} in ethanol) that is commonly assigned to a ring-breathing mode of the molecule [102]. Kukura and co-workers show that in their broadband impulsive vibrational spectroscopy experiment a decrease of the coherence frequency of rhodamine 101 under on-resonant excitation (w.r.t. off-resonance excitation) is due to the fact that the vibrational coherence is in the excited state, while under off-resonant excitation it is in the ground state [166]. The fact that the excited state vibrational coherence is at lower frequency corresponds to a 'softening' of the bonds of the vibrational mode in the excited state. In our experiments we observe a coherence with a frequency of 575 cm^{-1} in addition to the coherence with 594 cm^{-1} that is commonly reported [47, 72, 101, 168, 179].

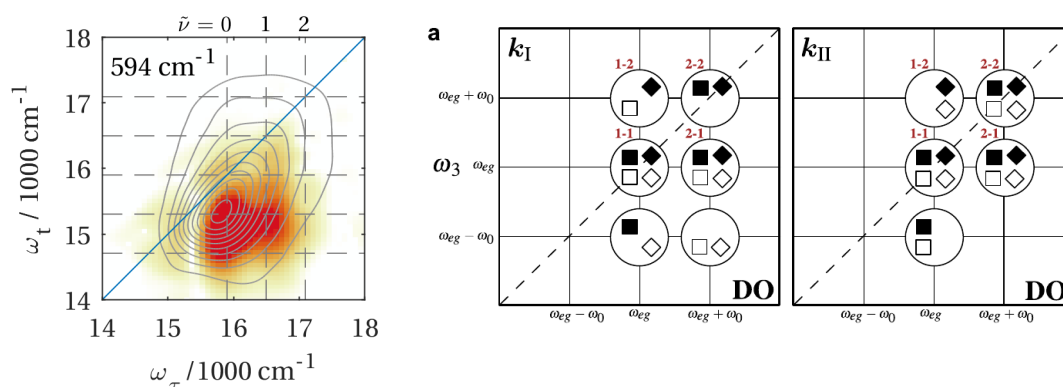


Figure 6.10 – (left) Beating map of the 594 cm^{-1} coherence, derived from an absorptive (R + NR pathway) 2D measurement, with lines (gray, dashed) indicating the 0,1, and 2 vibrational band of the electronic transition. (right) Different regions of the 2D spectrum can be assigned to specific Liouville pathways, and thus transient components, of a displaced oscillator (DO). k_I : rephasing and k_{II} : non-rephasing contribution to the 2D signal. \square : SE, \diamond : GSB; filled symbols: non-oscillating, open symbols: oscillating contribution.

A simple model, in which we add two cosine functions with $f_1 = 575\text{ cm}^{-1}$ and $f_2 = 594\text{ cm}^{-1}$ with a $\pi/2$ phase difference, elegantly reproduces the oscillations and the beat node at approx. 1.2 ps, while without the phase shift the beat node appears at 850 ps. Notably this model is very simplistic and can at best give an idea of the microscopic dynamics in nb. A more thorough analysis is on-going and involves the separate treatment of the R and NR contributions to the beating spectra, as discussed in [63, 65, 76]. Figure 6.10 preliminarily compares the 595 cm^{-1} beating map of the absorptive 2D spectrum of nb to the coherence patterns predicted for the R (k_I) and NR (k_{II}) contributions of a displaced oscillator model [63].

6.8 Outlook

The preliminary discussion above shows the potential of 2D spectroscopy to extract information about coherences in molecular systems, however additional steps are required to make use of the measured signal. These can be summarized as follows: Splitting of the absorptive 2D data into (i) R and NR components and comparison of the emerging beating patterns according to ref. [63] and (ii) using a complex Fourier transformation to extract positive and negative frequencies of the vibrational coherences [74]. The same analysis will be applied to range of molecular dyes to assess the information content that can be gained, with regards to the non-equilibrium dynamics of small molecules.

7 Conclusion and outlook

This thesis presents the application and development of time-resolved optical techniques to study the non-equilibrium dynamics of di-platinum complexes, as well as dye molecules in solution. The main goal of the research is to understand the interplay between electronic and vibrational degrees of freedom, and how these interactions govern molecular dynamics.

Using transient absorption spectroscopy in combination with transient absorption anisotropy and fluorescence up-conversion techniques, we gain new insights into the vibrational dynamics of di-platinum complexes. Initially, we disentangle the various contributions to the transient absorption signal of $[\text{Pt}(\text{ppy})(\mu\text{-tBu}_2\text{pz})_2]$ by their time-dependent absorption anisotropy. Time-resolved fluorescence up-conversion experiments verify our tentative assignment of a stimulated emission signal, which originates from a singlet state, and the presence of this singlet feature that disappears within 0.6 to 0.9 ps allows us to correct a previously assigned time constant for the intersystem crossing process. Based on the assignment of all spectral signatures, we tentatively attribute the observed oscillations with 100 cm^{-1} and 130 cm^{-1} to ground- and excited state vibrational coherences, where the higher frequency reflects the increased bonding character in the excited state. The damping of the coherences is accompanied by intersystem crossing, linking electronic relaxation to the structural motion of the molecule. Or vice versa! Time-dependent density functional theory calculations are currently underway, to shed additional light onto the intersystem crossing process and the structural dynamics of $[\text{Pt}(\text{ppy})(\mu\text{-tBu}_2\text{pz})_2]$.

Chapter 7. Conclusion and outlook

In addition, we present the first experiments on our revised two-dimensional Fourier transform spectroscopy setup based on a hollow-core fiber white light source. Improvements during the time of this thesis include the implementation of shot-to-shot detection, recovery of the absorptive spectral components from the complex data, increase of the data acquisition speed, and the achievement of 10 to 15 fs temporal resolution. The accessible spectral window ranges from 500 to 750 nm, allowing us to capture the complete spectral evolution of visible transient absorption bands, which typically span 50 nm or more. Future updates of the setup will extend the detection region to even higher energies, as we are particularly interested in the 300 to 500 nm region. Preliminary measurements of dye molecules prove the versatility of the setup and pave the way to more complex systems, such as porphyrins and porphyrin dyads, transition metal complexes, perovskites, as well as photo-switches. We firmly believe that two-dimensional spectroscopy has the potential to answer long-standing questions about the non-equilibrium dynamics of these systems and we hope to address them in the future.

The recent development of multidimensional spectroscopy in general tends towards new and exciting techniques, such as 5th or even higher order spectroscopy, coherent UV spectroscopy, or coherent X-ray experiments; but also towards making the existing techniques more accessible to scientists. The latter involves simplifying experimental schemes and providing infrastructure for collaborations, but also designing and sharing software for data treatment and analysis. A particularly interesting development concerns the detected signals. While traditionally the observable is a change in 'absorption', recently it has become possible to detect fluorescence; photoelectrons, photoions or photofragments; or even photocurrents. In addition, 2D pulse schemes are coupled to microscopes, adding a spatial component to the experimental degrees of freedom.

Finally, with such a remarkable range of state-of-the-art techniques the stage is set for researchers across all fields, to address questions of fundamental scientific interest – from quantum electrodynamics to biological functionality!

A Software

As part of my thesis I wrote a series of software packages to acquire, treat and analyze the data, and this appendix will provide a brief overview of the individual programs.

LSUCCD (LabView) acquires data from the FPGA CCD detector, displays a live preview, controls both delays stages and saves the background subtracted data.

D2D (Matlab, version 10: D2Dv10.m) performs the data treatment, displaying various intermediate steps, and iteratively search for a phase correction function. It loads the raw data from LSUCCD and a wavelength calibration file, and outputs the complex valued 2D spectrum together with the excitation- and detection frequency axis.

A2D (Matlab, version 5 (A2Dv5.m) is a data analysis program that loads and displays 2D spectra for a range of population times. The program extracts single time traces, as well as maximum amplitude and center frequency of the 2D spectrum, and the center line slope for every population time. In addition, it fits the entire dataset, subtracts the exponential kinetics and Fourier transforms the dataset, $T \rightarrow \Omega_T$.

Bibliography

- [1] T. Kane and M. Scher, “A Dynamical Explanation of the Falling Cat Phenomenon”, *International Journal of Solids and Structures* 5.7 (1969), pp. 663–670, DOI: 10.1016/0020-7683(69)90086-9.
- [2] C. H. Townes, “The First Laser”, *Century of Nature: Twenty-One Discoveries That Changed Science and the World*, 2003, pp. 107–12.
- [3] “The Nobel Prize in Physics 2018”, *NobelPrize.org* (2018).
- [4] “The Nobel Prize in Physics 2005”, *NobelPrize.org* (2005).
- [5] A. Apolonski, A. Poppe, G. Tempea, C. Spielmann, T. Udem, R. Holzwarth, T. W. Hänsch, and F. Krausz, “Controlling the Phase Evolution of Few-Cycle Light Pulses”, *Physical Review Letters* 85.4 (2000), pp. 740–743, DOI: 10.1103/PhysRevLett.85.740.
- [6] A. Baltuška, T. Udem, M. Uiberacker, M. Hentschel, E. Goulielmakis, C. Gohle, R. Holzwarth, V. S. Yakovlev, A. Scrinzi, T. W. Hänsch, and F. Krausz, “Attosecond Control of Electronic Processes by Intense Light Fields”, *Nature* 421.6923 (2003), pp. 611–615, DOI: 10.1038/nature01414.
- [7] U. Keller, “Recent Developments in Compact Ultrafast Lasers”, *Nature* 424.6950 (2003), pp. 831–838, DOI: 10.1038/nature01938.
- [8] “The Nobel Prize in Chemistry 1999”, *NobelPrize.org* (1999).
- [9] A. W. Castleman, “Femtochemistry 97 Lund, Sweden August 31-September 4, 1997”, *Journal of Physical Chemistry A* 102.23 (1998), p. 1.
- [10] V. Sundström, “The Third Femtochemistry Conference: An Introduction”, *The Journal of Physical Chemistry A* 102.23 (1998), pp. 4030–4030, DOI: 10.1021/jp981169q.
- [11] PSI, *Chemical Time Scales* (accessed 13.2.2019), <https://www.psi.ch/swissfel/chemical-time-scales>.
- [12] A. Borzsonyi, A. Kovacs, and K. Osvay, “What We Can Learn about Ultrashort Pulses by Linear Optical Methods”, *Applied Sciences* 3.2 (2013), pp. 515–544, DOI: 10.3390/app3020515.
- [13] J. N. Sweetser, D. N. Fittinghoff, and R. Trebino, “Transient-Grating Frequency-Resolved Optical Gating.”, *Optics letters* 22.8 (1997), pp. 519–521, DOI: 10.1364/OL.22.000519.

Bibliography

- [14] R. Trebino, K. W. DeLong, D. N. Fittinghoff, J. N. Sweetser, M. A. Krumbügel, B. A. Richman, and D. J. Kane, “Measuring Ultrashort Laser Pulses in the Time-Frequency Domain Using Frequency-Resolved Optical Gating”, *Review of Scientific Instruments* 68.9 (1997), pp. 3277–3295, DOI: 10.1063/1.1148286.
- [15] E. Träger, ed., *Handbook of Lasers and Optics*, Springer, 2007.
- [16] J. Ratner, G. Steinmeyer, T. C. Wong, R. Bartels, and R. Trebino, “Coherent Artifact in Modern Pulse Measurements”, *Optics Letters* 37.14 (2012), p. 2874, DOI: 10.1364/OL.37.002874.
- [17] M. Rhodes, Z. Guang, and R. Trebino, “Unstable and Multiple Pulsing Can Be Invisible to Ultrashort Pulse Measurement Techniques”, *Applied Sciences* 7.1 (2016), p. 40, DOI: 10.3390/app7010040.
- [18] S. Mukamel, *Principles of Nonlinear Optical Spectroscopy*, Oxford University Press, 1995.
- [19] M. Cho, *Two-Dimensional Optical Spectroscopy*, CRC Press, 2009.
- [20] L. Valkunas, D. Abramavicius, and T. Mančal, *Molecular Excitation Dynamics and Relaxation*, Weinheim: Wiley-VCH, 2013.
- [21] P. Hamm and M. T. Zanni, *Concepts and Methods of 2D Infrared Spectroscopy*, 1st ed., Cambridge University Press, 2011.
- [22] P. Hamm, “Principles of Nonlinear Optical Spectroscopy: A Practical Approach”, Lecture Notes, 2005.
- [23] R. P. Feynman, R. B. Leighton, and M. Sands, *The Feynman Lectures on Physics, Volume III*, online, California Institute of Technology, 1964.
- [24] A. Tokmakoff, “Lecture Notes: Density Matrix”, 2009.
- [25] M. Khalil, N. Demirdöven, and A. Tokmakoff, “Coherent 2D IR Spectroscopy: Molecular Structure and Dynamics in Solution”, *The Journal of Physical Chemistry A* 107.27 (2003), pp. 5258–5279, DOI: 10.1021/jp0219247.
- [26] A. Stolow, “Applications of Wavepacket Methodology”, *Philosophical Transactions of the Royal Society of London. Series A: Mathematical, Physical and Engineering Sciences* 356.1736 (1998), ed. by J. P. Simons, pp. 345–362, DOI: 10.1098/rsta.1998.0169.
- [27] W. Gawelda, A. Cannizzo, V.-T. Pham, F. van Mourik, C. Bressler, and M. Chergui, “Ultrafast Nonadiabatic Dynamics of $[\text{Fe}^{\text{II}}(\text{Bpy})_3]^{2+}$ in Solution”, *Journal of the American Chemical Society* 129.26 (2007), pp. 8199–8206, DOI: 10.1021/ja070454x.
- [28] G. Auböck and M. Chergui, “Sub-50-fs Photoinduced Spin Crossover in $[\text{Fe}(\text{Bpy})_3]^{2+}$ ”, *Nature Chemistry* 7.8 (2015), pp. 629–633, DOI: 10.1038/nchem.2305.
- [29] M. van Veenendaal, “Ultrafast Intersystem Crossings in Fe-Co Prussian Blue Analogues”, *Scientific Reports* 7.1 (2017), DOI: 10.1038/s41598-017-06664-4.

- [30] R. M. van der Veen, A. Cannizzo, F. van Mourik, A. Vlček, and M. Chergui, “Vibrational Relaxation and Intersystem Crossing of Binuclear Metal Complexes in Solution”, *Journal of the American Chemical Society* 133.2 (2011), pp. 305–315, DOI: 10.1021/ja106769w.
- [31] R. Monni, G. Auböck, D. Kinschel, K. M. Aziz-Lange, H. B. Gray, A. Vlček, and M. Chergui, “Conservation of Vibrational Coherence in Ultrafast Electronic Relaxation: The Case of Diplatinum Complexes in Solution”, *Chemical Physics Letters* 683 (2017), pp. 112–120, DOI: 10.1016/j.cplett.2017.02.071.
- [32] R. Monni, G. Capano, G. Auböck, H. B. Gray, A. Vlček, I. Tavernelli, and M. Chergui, “Vibrational Coherence Transfer in the Ultrafast Intersystem Crossing of a Diplatinum Complex in Solution”, *Proceedings of the National Academy of Sciences* 115.28 (2018), E6396–E6403, DOI: 10.1073/pnas.1719899115.
- [33] A. K. Dioumaev, “Evaluation of Intrinsic Chemical Kinetics and Transient Product Spectra from Time-Resolved Spectroscopic Data”, *Biophysical Chemistry* 67.1-3 (1997), pp. 1–25, DOI: 10.1016/S0301-4622(96)02268-5.
- [34] J. Dostál, B. Benešová, and T. Brixner, “Two-Dimensional Electronic Spectroscopy Can Fully Characterize the Population Transfer in Molecular Systems”, *The Journal of Chemical Physics* 145.12 (2016), p. 124312, DOI: 10.1063/1.4962577.
- [35] J. R. Lakowicz, *Principles of Fluorescence Spectroscopy*, 3rd ed., Springer New York, 2006.
- [36] P. Kapusta, “Time-Resolved Fluorescence Anisotropy Measurements Made Simple”, Technical Note, 2002.
- [37] S. Wallin, J. Davidsson, J. Modin, and L. Hammarström, “Femtosecond Transient Absorption Anisotropy Study on $[\text{Ru}(\text{Bpy})_3]^{2+}$ and $[\text{Ru}(\text{Bpy})(\text{Py})_4]^{2+}$: Ultrafast Interligand Randomization of the MLCT State”, *Journal of Physical Chemistry A* 109.21 (2005), pp. 4697–4704, DOI: 10.1021/jp0509212.
- [38] D. A. Farrow, E. R. Smith, W. Qian, and D. M. Jonas, “The Polarization Anisotropy of Vibrational Quantum Beats in Resonant Pump-Probe Experiments: Diagrammatic Calculations for Square Symmetric Molecules”, *Journal of Chemical Physics* 129.17 (2008), DOI: 10.1063/1.2982160.
- [39] O. Schalk and A. N. Unterreiner, “Transient Anisotropy in Degenerate Systems: A Semi-Classical Approach”, *Zeitschrift für Physikalische Chemie* 225.9-10 (2011), pp. 927–938, DOI: 10.1524/zpch.2011.0133.
- [40] M. Ameloot, M. Van de Ven, A. Acuña, and B. Valeur, “Fluorescence Anisotropy Measurements in Solution: Methods and Reference Materials (IUPAC Technical Report).”, *Pure Applied Chemistry* 85.3 (2013), pp. 589–608, DOI: 10.1351/PAC-REP-11-11-12.

Bibliography

- [41] H. B. Lee, A. Cong, H. Leopold, M. Currie, A. J. Boersma, E. D. Sheets, and A. A. Heikal, "Rotational and Translational Diffusion of Size-Dependent Fluorescent Probes in Homogeneous and Heterogeneous Environments", *Physical Chemistry Chemical Physics* 20.37 (2018), pp. 24045–24057, DOI: 10.1039/C8CP03873B.
- [42] T. Takaya, H.-o. Hamaguchi, and K. Iwata, "Femtosecond Time-Resolved Absorption Anisotropy Spectroscopy on 9,9'-Bianthryl: Detection of Partial Intramolecular Charge Transfer in Polar and Nonpolar Solvents", *The Journal of Chemical Physics* 130.1 (2009), p. 014501, DOI: 10.1063/1.3043368.
- [43] L. Lepetit, G. Chériaux, and M. Joffre, "Linear Techniques of Phase Measurement by Femtosecond Spectral Interferometry for Applications in Spectroscopy", *Journal of the Optical Society of America B* 12.12 (1995), p. 2467, DOI: 10.1364/JOSAB.12.002467.
- [44] D. M. Jonas, "TWO-DIMENSIONAL FEMTOSECOND SPECTROSCOPY", *Annual Review of Physical Chemistry* 54.1 (2003), pp. 425–463, DOI: 10.1146/annurev.physchem.54.011002.103907.
- [45] R. Mersereau and A. Oppenheim, "Digital Reconstruction of Multidimensional Signals from Their Projections", *Proceedings of the IEEE* 62.10 (1974), pp. 1319–1338, DOI: 10.1109/PROC.1974.9625.
- [46] T. Brixner, T. Mančal, I. V. Stiopkin, and G. R. Fleming, "Phase-Stabilized Two-Dimensional Electronic Spectroscopy", *The Journal of Chemical Physics* 121.9 (2004), pp. 4221–4236, DOI: 10.1063/1.1776112.
- [47] M. Son, S. Mosquera-Vázquez, and G. S. Schlau-Cohen, "Ultrabroadband 2D Electronic Spectroscopy with High-Speed, Shot-to-Shot Detection", *Optics Express* 25.16 (2017), p. 18950, DOI: 10.1364/OE.25.018950.
- [48] R. Augulis and D. Zigmantas, "Detector and Dispersive Delay Calibration Issues in Broadband 2D Electronic Spectroscopy", *Journal of the Optical Society of America B* 30.6 (2013), p. 1770, DOI: 10.1364/JOSAB.30.001770.
- [49] T. Mančal, N. Christensson, V. Lukeš, F. Milota, O. Bixner, H. F. Kauffmann, and J. Hauer, "System-Dependent Signatures of Electronic and Vibrational Coherences in Electronic Two-Dimensional Spectra", *The Journal of Physical Chemistry Letters* 3.11 (2012), pp. 1497–1502, DOI: 10.1021/jz300362k.
- [50] L. Zhu, A. Widom, and P. M. Champion, "A Multidimensional Landau-Zener Description of Chemical Reaction Dynamics and Vibrational Coherence", *The Journal of Chemical Physics* 107.8 (1997), pp. 2859–2871, DOI: 10.1063/1.474645.
- [51] A. T. N. Kumar, F. Rosca, A. Widom, and P. M. Champion, "Investigations of Amplitude and Phase Excitation Profiles in Femtosecond Coherence Spectroscopy", *The Journal of Chemical Physics* 114.2 (2001), p. 701, DOI: 10.1063/1.1329640.
- [52] J. M. Womick, B. A. West, N. F. Scherer, and A. M. Moran, "Vibronic Effects in the Spectroscopy and Dynamics of C -Phycocyanin", *Journal of Physics B: Atomic, Molecular and Optical Physics* 45.15 (2012), p. 154016, DOI: 10.1088/0953-4075/45/15/154016.

- [53] S. Polyutov, O. Kühn, and T. Pullerits, “Exciton-Vibrational Coupling in Molecular Aggregates: Electronic versus Vibronic Dimer”, *Chemical Physics* 394.1 (2012), pp. 21–28, DOI: 10.1016/j.chemphys.2011.12.006.
- [54] V. Butkus, J. Alster, E. Bašinskaitė, R. Augulis, P. Neuhaus, L. Valkunas, H. L. Anderson, D. Abramavicius, and D. Zigmantas, “Diversity of Coherences and Origin of Electronic Transitions of Supermolecular Nanoring”, *arXiv* (2015), arXiv: 1503.00870.
- [55] A. A. Bakulin, S. E. Morgan, T. B. Kehoe, M. W. B. Wilson, A. W. Chin, D. Zigmantas, D. Egorova, and A. Rao, “Real-Time Observation of Multiexcitonic States in Ultrafast Singlet Fission Using Coherent 2D Electronic Spectroscopy”, *Nature Chemistry* 8.1 (2016), pp. 16–23, DOI: 10.1038/nchem.2371.
- [56] R. Tempelaar and D. R. Reichman, “Vibronic Exciton Theory of Singlet Fission. I. Linear Absorption and the Anatomy of the Correlated Triplet Pair State”, *The Journal of Chemical Physics* 146.17 (2017), p. 174703, DOI: 10.1063/1.4982362.
- [57] R. Tempelaar and D. R. Reichman, “Vibronic Exciton Theory of Singlet Fission. II. Two-Dimensional Spectroscopic Detection of the Correlated Triplet Pair State”, *The Journal of Chemical Physics* 146.17 (2017), p. 174704, DOI: 10.1063/1.4982359.
- [58] A. De Sio and C. Lienau, “Vibronic Coupling in Organic Semiconductors for Photovoltaics”, *Physical Chemistry Chemical Physics* 19.29 (2017), pp. 18813–18830, DOI: 10.1039/C7CP03007J.
- [59] E. Thyryhaug, R. Tempelaar, M. Alcocer, K. Židek, D. Bína, J. Knoester, T. L. C. Jansen, and D. Zigmantas, “Unravelling Coherences in the FMO Complex”, *arXiv* (2017), arXiv: 1709.00318.
- [60] W. P. Carbery, A. Verma, and D. B. Turner, “Spin–Orbit Coupling Drives Femtosecond Nonadiabatic Dynamics in a Transition Metal Compound”, *The Journal of Physical Chemistry Letters* 8.6 (2017), pp. 1315–1322, DOI: 10.1021/acs.jpcllett.7b00130.
- [61] T. J. Penfold, E. Gindensperger, C. Daniel, and C. M. Marian, “Spin-Vibronic Mechanism for Intersystem Crossing”, *Chemical Reviews* 118.15 (2018), pp. 6975–7025, DOI: 10.1021/acs.chemrev.7b00617.
- [62] V. Butkus, L. Valkunas, and D. Abramavicius, “Molecular Vibrations-Induced Quantum Beats in Two-Dimensional Electronic Spectroscopy”, *The Journal of Chemical Physics* 137.4 (2012), p. 044513, DOI: 10.1063/1.4737843.
- [63] V. Butkus, D. Zigmantas, L. Valkunas, and D. Abramavicius, “Vibrational vs. Electronic Coherences in 2D Spectrum of Molecular Systems”, *Chemical Physics Letters* 545 (2012), pp. 40–43, DOI: 10.1016/j.cplett.2012.07.014.
- [64] V. Butkus, D. Zigmantas, D. Abramavicius, and L. Valkunas, “Distinctive Character of Electronic and Vibrational Coherences in Disordered Molecular Aggregates”, *Chemical Physics Letters* 587 (2013), pp. 93–98, DOI: 10.1016/j.cplett.2013.09.043.

Bibliography

- [65] L. Z. Sharp and D. Egorova, "Towards Microscopic Assignment of Oscillative Signatures in Two-Dimensional Electronic Photon-Echo Signals of Vibronic Oligomers: A Vibronic Dimer Model", *The Journal of Chemical Physics* 139.14 (2013), p. 144304, DOI: 10.1063/1.4822425.
- [66] K. Kwak, S. Park, I. J. Finkelstein, and M. D. Fayer, "Frequency-Frequency Correlation Functions and Apodization in Two-Dimensional Infrared Vibrational Echo Spectroscopy: A New Approach", *The Journal of Chemical Physics* 127.12 (2007), p. 124503, DOI: 10.1063/1.2772269.
- [67] K.-W. Kwak, "Extracting Frequency-Frequency Correlation Function from Two-Dimensional Infrared Spectroscopy: Peak Shift Measurement", *Bulletin of the Korean Chemical Society* 33.10 (2012), pp. 3391–3396, DOI: 10.5012/bkcs.2012.33.10.3391.
- [68] K. L. Wells, Z. Zhang, J. R. Rouxel, and H.-S. Tan, "Measuring the Spectral Diffusion of Chlorophyll *a* Using Two-Dimensional Electronic Spectroscopy", *The Journal of Physical Chemistry B* 117.8 (2013), pp. 2294–2299, DOI: 10.1021/jp310154y.
- [69] F. Šanda, V. Perlík, C. N. Lincoln, and J. Hauer, "Center Line Slope Analysis in Two-Dimensional Electronic Spectroscopy", *The Journal of Physical Chemistry A* 119.44 (2015), pp. 10893–10909, DOI: 10.1021/acs.jpca.5b08909.
- [70] D. Egorova, M. F. Gelin, and W. Domcke, "Analysis of Cross Peaks in Two-Dimensional Electronic Photon-Echo Spectroscopy for Simple Models with Vibrations and Dissipation", *The Journal of Chemical Physics* 126.7 (2007), p. 074314, DOI: 10.1063/1.2435353.
- [71] D. Egorova, "Detection of Electronic and Vibrational Coherences in Molecular Systems by 2D Electronic Photon Echo Spectroscopy", *Chemical Physics* 347.1-3 (2008), pp. 166–176, DOI: 10.1016/j.chemphys.2007.12.019.
- [72] D. Egorova, M. F. Gelin, and W. Domcke, "Analysis of Vibrational Coherences in Homodyne and Two-Dimensional Heterodyne Photon-Echo Spectra of Nile Blue", *Chemical Physics* 341.1-3 (2007), pp. 113–122, DOI: 10.1016/j.chemphys.2007.07.010.
- [73] J. Dostál, T. Mančal, R.-n. Augulis, F. Vácha, J. Pšenčík, and D. Zigmantas, "Two-Dimensional Electronic Spectroscopy Reveals Ultrafast Energy Diffusion in Chlorosomes", *Journal of the American Chemical Society* 134.28 (2012), pp. 11611–11617, DOI: 10.1021/ja3025627.
- [74] J. Seibt and T. Pullerits, "Beating Signals in 2D Spectroscopy: Electronic or Nuclear Coherences? Application to a Quantum Dot Model System", *The Journal of Physical Chemistry C* 117.36 (2013), pp. 18728–18737, DOI: 10.1021/jp406103m.
- [75] J. Dostál, T. Mančal, F. Vácha, J. Pšenčík, and D. Zigmantas, "Unraveling the Nature of Coherent Beatings in Chlorosomes", *The Journal of Chemical Physics* 140.11 (2014), p. 115103, DOI: 10.1063/1.4868557.
- [76] D. Egorova, "Self-Analysis of Coherent Oscillations in Time-Resolved Optical Signals", *The Journal of Physical Chemistry A* 118.44 (2014), pp. 10259–10267, DOI: 10.1021/jp509657u.

- [77] E. Riedle, M. Beutter, S. Lochbrunner, J. Piel, S. Schenkl, S. Spörlein, and W. Zinth, “Generation of 10 to 50 fs Pulses Tunable through All of the Visible and the NIR”, *Applied Physics B* 71.3 (2000), pp. 457–465, DOI: 10.1007/s003400000351.
- [78] C. Manzoni and G. Cerullo, “Design Criteria for Ultrafast Optical Parametric Amplifiers”, *Journal of Optics* 18.10 (2016), p. 103501, DOI: 10.1088/2040-8978/18/10/103501.
- [79] P. Baum, S. Lochbrunner, P. Krok, M. Breuer, and E. Riedle, *NOPA - Overview and Principles*, http://www.bmo.physik.uni-muenchen.de/~wwwriedle/projects/NOPA_overview/NOPA_overview.php.
- [80] O. E. Martinez, R. L. Fork, and J. P. Gordon, “Theory of Passively Mode-Locked Lasers Including Self-Phase Modulation and Group-Velocity Dispersion”, *Optics Letters* 9.5 (1984), p. 156, DOI: 10.1364/OL.9.000156.
- [81] J. P. Gordon and R. L. Fork, “Optical Resonator with Negative Dispersion”, *Optics Letters* 9.5 (1984), p. 153, DOI: 10.1364/OL.9.000153.
- [82] O. E. Martinez, J. P. Gordon, and R. L. Fork, “Negative Group-Velocity Dispersion Using Refraction”, *Journal of the Optical Society of America A* 1.10 (1984), p. 1003, DOI: 10.1364/JOSAA.1.001003.
- [83] R. L. Fork, O. E. Martinez, and J. P. Gordon, “Negative Dispersion Using Pairs of Prisms”, *Optics Letters* 9.5 (1984), p. 150, DOI: 10.1364/OL.9.000150.
- [84] B. Schmidt, M. Hacker, and T. Feurer, *LAB2-A Virtual Femtosecond Laser Lab*, Institute of Applied Physics in Bern, 1998.
- [85] S. Akturk, X. Gu, M. Kimmel, and R. Trebino, “Extremely Simple Single-Prism Ultrashort-Pulse Compressor”, *Optics Express* 14.21 (2006), p. 10101, DOI: 10.1364/OE.14.010101.
- [86] A. Al Haddad, A. Chauvet, J. Ojeda, C. Arrell, F. van Mourik, G. Auböck, and M. Chergui, “Set-up for Broadband Fourier-Transform Multidimensional Electronic Spectroscopy”, *Optics Letters* 40.3 (2015), p. 312, DOI: 10.1364/OL.40.000312.
- [87] M. K. Yetzbacher, N. Belabas, K. A. Kitney, and D. M. Jonas, “Propagation, Beam Geometry, and Detection Distortions of Peak Shapes in Two-Dimensional Fourier Transform Spectra”, *The Journal of Chemical Physics* 126.4 (2007), p. 044511, DOI: 10.1063/1.2426337.
- [88] M. Nisoli, S. De Silvestri, and O. Svelto, “Generation of High Energy 10 fs Pulses by a New Pulse Compression Technique”, *Applied Physics Letters* 68.20 (1996), pp. 2793–2795, DOI: 10.1063/1.116609.
- [89] M. Nisoli, S. Stagira, S. De Silvestri, O. Svelto, S. Sartania, Z. Cheng, M. Lenzner, C. Spielmann, and F. Krausz, “A Novel-High Energy Pulse Compression System: Generation of Multigigawatt Sub-5-fs Pulses”, *Applied Physics B: Lasers and Optics* 65.2 (1997), pp. 189–196, DOI: 10.1007/s003400050263.
- [90] T. Witting, F. Frank, C. A. Arrell, W. A. Okell, J. P. Marangos, and J. W. G. Tisch, “Characterization of High-Intensity Sub-4-fs Laser Pulses Using Spatially Encoded Spectral Shearing Interferometry”, *Optics Letters* 36.9 (2011), p. 1680, DOI: 10.1364/OL.36.001680.

Bibliography

- [91] F. Frank, C. Arrell, T. Witting, W. A. Okell, J. McKenna, J. S. Robinson, C. A. Haworth, D. Austin, H. Teng, I. A. Walmsley, J. P. Marangos, and J. W. G. Tisch, "Invited Review Article: Technology for Attosecond Science", *Review of Scientific Instruments* 83.7 (2012), DOI: 10.1063/1.4731658.
- [92] W. A. Okell, T. Witting, D. Fabris, D. Austin, M. Bocoum, F. Frank, A. Ricci, A. Jullien, D. Walke, J. P. Marangos, R. Lopez-Martens, and J. W. G. Tisch, "Carrier-Envelope Phase Stability of Hollow Fibers Used for High-Energy Few-Cycle Pulse Generation", *Optics Letters* 38.19 (2013), p. 3918, DOI: 10.1364/OL.38.003918.
- [93] E. A. J. Marcatili and R. A. Schmeltzer, "Hollow Metallic and Dielectric Waveguides for Long Distance Optical Transmission and Lasers", *Bell System Technical Journal* 43.4 (1964), pp. 1783–1809, DOI: 10.1002/j.1538-7305.1964.tb04108.x.
- [94] J. Robinson, C. Haworth, H. Teng, R. Smith, J. Marangos, and J. Tisch, "The Generation of Intense, Transform-Limited Laser Pulses with Tunable Duration from 6 to 30 fs in a Differentially Pumped Hollow Fibre", *Applied Physics B* 85.4 (2006), pp. 525–529, DOI: 10.1007/s00340-006-2390-z.
- [95] N. Matuschek, F. Kartner, and U. Keller, "Theory of Double-Chirped Mirrors", *IEEE Journal of Selected Topics in Quantum Electronics* 4.2 (1998), pp. 197–208, DOI: 10.1109/2944.686724.
- [96] T. J. Butenhoff and E. A. Rohlfing, "Laser-induced Gratings in Free Jets. I. Spectroscopy of Predissociating NO₂", *The Journal of Chemical Physics* 98.7 (1993), pp. 5460–5468, DOI: 10.1063/1.464895.
- [97] J. D. Hybl, A. Albrecht Ferro, and D. M. Jonas, "Two-Dimensional Fourier Transform Electronic Spectroscopy", *The Journal of Chemical Physics* 115.14 (2001), pp. 6606–6622, DOI: 10.1063/1.1398579.
- [98] M. Cowan, J. Ogilvie, and R. Miller, "Two-Dimensional Spectroscopy Using Diffractive Optics Based Phased-Locked Photon Echoes", *Chemical Physics Letters* 386.1-3 (2004), pp. 184–189, DOI: 10.1016/j.cplett.2004.01.027.
- [99] V. I. Prokhorenko, A. Halpin, and R. D. Miller, "Coherently-Controlled Two-Dimensional Photon Echo Electronic Spectroscopy", *Optics Express* 17.12 (2009), p. 9764, DOI: 10.1364/OE.17.009764.
- [100] W. Pollard, H. Fragnito, J.-Y. Bigot, C. Shank, and R. Mathies, "Quantum-Mechanical Theory for 6 fs Dynamic Absorption Spectroscopy and Its Application to Nile Blue", *Chemical Physics Letters* 168.3-4 (1990), pp. 239–245, DOI: 10.1016/0009-2614(90)85603-A.
- [101] M. K. Lawless and R. A. Mathies, "Excited-state Structure and Electronic Dephasing Time of Nile Blue from Absolute Resonance Raman Intensities", *The Journal of Chemical Physics* 96.11 (1992), pp. 8037–8045, DOI: 10.1063/1.462355.

- [102] A. Reigue, B. Augu  , P. G. Etchegoin, and E. C. Le Ru, "CW Measurements of Resonance Raman Profiles, Line-Widths, and Cross-Sections of Fluorescent Dyes: Application to Nile Blue A in Water and Ethanol: Measuring Resonance Raman Spectra of Fluorophores", *Journal of Raman Spectroscopy* 44.4 (2013), pp. 573–581, DOI: 10.1002/jrs.4233.
- [103] B. Ma, J. Li, P. I. Djurovich, M. Yousufuddin, R. Bau, and M. E. Thompson, "Synthetic Control of Pt–Pt Separation and Photophysics of Binuclear Platinum Complexes", *Journal of the American Chemical Society* 127.1 (2005), pp. 28–29, DOI: 10.1021/ja044313w.
- [104] B. Ma, P. I. Djurovich, S. Garon, B. Alleyne, and M. E. Thompson, "Platinum Binuclear Complexes as Phosphorescent Dopants for Monochromatic and White Organic Light-Emitting Diodes", *Advanced Functional Materials* 16.18 (2006), pp. 2438–2446, DOI: 10.1002/adfm.200600614.
- [105] A. A. Rachford and F. N. Castellano, "Thermochromic Absorption and Photoluminescence in [Pt(Ppy)(μ -Ph₂pz)]₂", *Inorganic Chemistry* 48.23 (2009), pp. 10865–10867, DOI: 10.1021/ic901156z.
- [106] R. C. Evans, P. Douglas, and C. J. Winscom, "Coordination Complexes Exhibiting Room-Temperature Phosphorescence: Evaluation of Their Suitability as Triplet Emitters in Organic Light Emitting Diodes", *Coordination Chemistry Reviews* 250.15–16 (2006), pp. 2093–2126, DOI: 10.1016/j.ccr.2006.02.007.
- [107] J. A. G. Williams, "Optimising the Luminescence of Platinum(II) Complexes and Their Application in Organic Light Emitting Devices (OLEDs)", *Coordination Chemistry Reviews* (2008), p. 16.
- [108] C.-L. Ho, W.-Y. Wong, B. Yao, Z. Xie, L. Wang, and Z. Lin, "Synthesis, Characterization, Photophysics and Electrophosphorescent Applications of Phosphorescent Platinum Cyclometalated Complexes with 9-Arylcarbazole Moieties", *Journal of Organometallic Chemistry* 694.17 (2009), pp. 2735–2749, DOI: 10.1016/j.jorganchem.2009.03.002.
- [109] A. F. Heyduk, "Hydrogen Produced from Hydrohalic Acid Solutions by a Two-Electron Mixed-Valence Photocatalyst", *Science* 293.5535 (2001), pp. 1639–1641, DOI: 10.1126/science.1062965.
- [110] A. O. Dohn, K. S. Kj  r, T. B. Harlang, S. E. Canton, M. M. Nielsen, and K. B. M  ller, "Electron Transfer and Solvent-Mediated Electronic Localization in Molecular Photocatalysis", *Inorganic Chemistry* 55.20 (2016), pp. 10637–10644, DOI: 10.1021/acs.inorgchem.6b01840.
- [111] R. M. van der Veen, C. J. Milne, V.-T. Pham, A. El Nahhas, J. A. Weinstein, J. Best, C. N. Borca, C. Bressler, and M. Chergui, "EXAFS Structural Determination of the Pt₂(P₂O₅H₂)₄⁴⁻ Anion in Solution", *CHIMIA International Journal for Chemistry* 62.4 (2008), pp. 287–290, DOI: 10.2533/chimia.2008.287.

Bibliography

- [112] A. O. Dohn, E. O. Jónsson, K. S. Kjær, T. B. van Driel, M. M. Nielsen, K. W. Jacobsen, N. E. Henriksen, and K. B. Møller, “Direct Dynamics Studies of a Binuclear Metal Complex in Solution: The Interplay Between Vibrational Relaxation, Coherence, and Solvent Effects”, *The Journal of Physical Chemistry Letters* 5.14 (2014), pp. 2414–2418, DOI: 10.1021/jz500850s.
- [113] C. Zhou, Y. Tian, Z. Yuan, M. Han, J. Wang, L. Zhu, M. S. Tameh, C. Huang, and B. Ma, “Precise Design of Phosphorescent Molecular Butterflies with Tunable Photoinduced Structural Change and Dual Emission”, *Angewandte Chemie International Edition* 54.33 (2015), pp. 9591–9595, DOI: 10.1002/anie.201505185.
- [114] M. Iwamura, R. Wakabayashi, J. Maeba, K. Nozaki, S. Takeuchi, and T. Tahara, “Coherent Vibration and Ultrafast Dynamics upon Bond Formation in Excited Dimers of an Au(I) Complex”, *Physical Chemistry Chemical Physics* 18.7 (2016), pp. 5103–5107, DOI: 10.1039/C5CP06651D.
- [115] G. Levi, M. Pápai, N. E. Henriksen, A. O. Dohn, and K. B. Møller, “Solution Structure and Ultrafast Vibrational Relaxation of the PtPOP Complex Revealed by Δ SCF-QM/MM Direct Dynamics Simulations”, *The Journal of Physical Chemistry C* 122.13 (2018), pp. 7100–7119, DOI: 10.1021/acs.jpcc.8b00301.
- [116] E. Biasin, T. B. van Driel, G. Levi, M. G. Laursen, A. O. Dohn, A. Molkte, P. Vester, F. B. K. Hansen, K. S. Kjaer, T. Harlang, R. Hartsock, M. Christensen, K. J. Gaffney, N. E. Henriksen, K. B. Møller, K. Haldrup, and M. M. Nielsen, “Anisotropy Enhanced X-Ray Scattering from Solvated Transition Metal Complexes”, *Journal of Synchrotron Radiation* 25.2 (2018), pp. 306–315, DOI: 10.1107/S1600577517016964, arXiv: 1801.06615.
- [117] M. Iwamura, K. Nozaki, S. Takeuchi, and T. Tahara, “Real-Time Observation of Tight Au–Au Bond Formation and Relevant Coherent Motion upon Photoexcitation of $[\text{Au}(\text{CN})_2]^-$ Oligomers”, *Journal of the American Chemical Society* 135.2 (2013), pp. 538–541, DOI: 10.1021/ja310004z.
- [118] S. Cho, M. W. Mara, X. Wang, J. V. Lockard, A. A. Rachford, F. N. Castellano, and L. X. Chen, “Coherence in Metal - Metal-to-Ligand-Charge-Transfer Excited States of a Dimetallic Complex Investigated by Ultrafast Transient Absorption Anisotropy”, *Journal of Physical Chemistry A* 115.16 (2011), pp. 3990–3996, DOI: 10.1021/jp109174f.
- [119] S. E. Brown-Xu, M. S. J. Kelley, K. A. Fransted, A. Chakraborty, G. C. Schatz, F. N. Castellano, and L. X. Chen, “Tunable Excited-State Properties and Dynamics as a Function of Pt–Pt Distance in Pyrazolate-Bridged Pt(II) Dimers”, *The Journal of Physical Chemistry A* 120.4 (2016), pp. 543–550, DOI: 10.1021/acs.jpca.5b11233.
- [120] D. B. Lingerfelt, P. J. Lestrangle, J. J. Radler, S. E. Brown-Xu, P. Kim, F. N. Castellano, L. X. Chen, and X. Li, “Can Excited State Electronic Coherence Be Tuned via Molecular Structural Modification? A First-Principles Quantum Electronic Dynamics Study of Pyrazolate-Bridged Pt(II) Dimers”, *Journal of Physical Chemistry A* 121.9 (2017), pp. 1932–1939, DOI: 10.1021/acs.jpca.6b12099.

- [121] J. J. Radler, D. B. Lingerfelt, F. N. Castellano, L. X. Chen, and X. Li, "Role of Vibrational Dynamics on Excited-State Electronic Coherence in a Binuclear Platinum Complex", *Journal of Physical Chemistry A* 122.23 (2018), pp. 5071–5077, DOI: 10.1021/acs.jpca.8b01352.
- [122] P. Kim, M. S. Kelley, A. Chakraborty, N. L. Wong, R. P. Van Duyne, G. C. Schatz, F. N. Castellano, and L. X. Chen, "Coherent Vibrational Wavepacket Dynamics in Platinum(II) Dimers and Their Implications", *The Journal of Physical Chemistry C* 122.25 (2018), pp. 14195–14204, DOI: 10.1021/acs.jpcc.8b01636.
- [123] S. Ruhman, A. G. Joly, and K. A. Nelson, "Time-resolved Observations of Coherent Molecular Vibrational Motion and the General Occurrence of Impulsive Stimulated Scattering", *The Journal of Chemical Physics* 86.11 (1987), pp. 6563–6565, DOI: 10.1063/1.452400.
- [124] M. Dantus, R. M. Bowman, and A. H. Zewail, "Femtosecond Laser Observations of Molecular Vibration and Rotation", *Nature* 343 (1990), p. 737.
- [125] A. H. Zewail, "Femtochemistry: Atomic-Scale Dynamics of the Chemical Bond", *The Journal of Physical Chemistry A* 104.24 (2000), pp. 5660–5694, DOI: 10.1021/jp001460h.
- [126] C. H. Kim and T. Joo, "Coherent Excited State Intramolecular Proton Transfer Probed by Time-Resolved Fluorescence", *Physical Chemistry Chemical Physics* 11.44 (2009), p. 10266, DOI: 10.1039/b915768a.
- [127] S. Maiti, G. C. Walker, B. R. Cowen, R. Pippenger, C. C. Moser, P. L. Dutton, and R. M. Hochstrasser, "Femtosecond Coherent Transient Infrared Spectroscopy of Reaction Centers from Rhodospirillum rubrum", *Proceedings of the National Academy of Sciences* 91.22 (1994), pp. 10360–10364, DOI: 10.1073/pnas.91.22.10360.
- [128] U. Hofer, "Time-Resolved Coherent Photoelectron Spectroscopy of Quantized Electronic States on Metal Surfaces", *Science* 277.5331 (1997), pp. 1480–1482, DOI: 10.1126/science.277.5331.1480.
- [129] A. T. Krummel, P. Mukherjee, and M. T. Zanni, "Inter and Intrastrand Vibrational Coupling in DNA Studied with Heterodyned 2D-IR Spectroscopy", *The Journal of Physical Chemistry B* 107.35 (2003), pp. 9165–9169, DOI: 10.1021/jp035473h.
- [130] C. Kübler, H. Ehrke, R. Huber, R. Lopez, A. Halabica, R. F. Haglund, and A. Leitenstorfer, "Coherent Structural Dynamics and Electronic Correlations during an Ultrafast Insulator-to-Metal Phase Transition in VO₂", *Physical Review Letters* 99.11 (2007), DOI: 10.1103/PhysRevLett.99.116401.
- [131] J. A. Yeazell, M. Mallalieu, and C. R. Stroud, "Observation of the Collapse and Revival of a Rydberg Electronic Wave Packet", *Physical Review Letters* 64.17 (1990), pp. 2007–2010, DOI: 10.1103/PhysRevLett.64.2007.
- [132] G. Alber and P. Zoller, "Laser Excitation of Electronic Wave Packets in Rydberg Atoms", *Physics Reports* 199.5 (1991), pp. 231–280, DOI: 10.1016/0370-1573(91)90058-T.

Bibliography

- [133] D. W. Oxtoby, "Dephasing of Molecular Vibrations in Liquids", *Advances in Chemical Physics*, ed. by I. Prigogine and S. A. Rice, Hoboken, NJ, USA: John Wiley & Sons, Inc., 1979, pp. 1–48, DOI: 10.1002/9780470142592.ch1.
- [134] W. Bosma, S. Mukamel, B. Greene, and S. Schmitt-Rink, "Brownian Oscillator Analysis of Femtosecond Pump-Probe Spectroscopy of Polydiacetylene", *Synthetic Metals* 49.1-3 (1992), pp. 71–76, DOI: 10.1016/0379-6779(92)90074-S.
- [135] B. Li, A. E. Johnson, S. Mukamel, and A. B. Myers, "The Brownian Oscillator Model for Solvation Effects in Spontaneous Light Emission and Their Relationship to Electron Transfer", *Journal of the American Chemical Society* 116.24 (1994), pp. 11039–11047, DOI: 10.1021/ja00103a020.
- [136] V. Chernyak and S. Mukamel, "Quadratic Brownian-Oscillator Model for Solvation Dynamics in Optical Response", *The Journal of Chemical Physics* 114.23 (2001), pp. 10430–10435, DOI: 10.1063/1.1371263.
- [137] M. A. Filatov, F. Etzold, D. Gehrig, F. Laquai, D. Busko, K. Landfester, and S. Baluschev, "Interplay between Singlet and Triplet Excited States in a Conformationally Locked Donor–Acceptor Dyad", *Dalton Transactions* 44.44 (2015), pp. 19207–19217, DOI: 10.1039/C5DT03784K.
- [138] K. J. Lee, J. H. Woo, E. Kim, Y. Xiao, X. Su, L. M. Mazur, A.-J. Attias, F. Fages, O. Cregut, A. Barsella, F. Mathevet, L. Mager, J. W. Wu, A. D'Aléo, and J.-C. Ribierre, "Electronic Energy and Electron Transfer Processes in Photoexcited Donor–Acceptor Dyad and Triad Molecular Systems Based on Triphenylene and Perylene Diimide Units", *Physical Chemistry Chemical Physics* 18.11 (2016), pp. 7875–7887, DOI: 10.1039/C5CP06279A.
- [139] S. M. Falke, C. A. Rozzi, D. Brida, M. Maiuri, M. Amato, E. Sommer, G. Cerullo, E. Molinari, and C. Lienau, "Coherent Ultrafast Charge Transfer in an Organic Photovoltaic Blend", *Science* 344.6187 (2014), p. 1001.
- [140] A. De Sio, F. Troiani, M. Maiuri, J. Réhault, E. Sommer, J. Lim, S. F. Huelga, M. B. Plenio, C. A. Rozzi, G. Cerullo, E. Molinari, and C. Lienau, "Tracking the Coherent Generation of Polaron Pairs in Conjugated Polymers", *Nature Communications* 7.1 (2016), DOI: 10.1038/ncomms13742.
- [141] Z. Arsov, I. Urbančič, and J. Štrancar, "Aggregation-Induced Emission Spectral Shift as a Measure of Local Concentration of a pH-Activatable Rhodamine-Based Smart Probe", *Spectrochimica Acta Part A: Molecular and Biomolecular Spectroscopy* 190 (2018), pp. 486–493, DOI: 10.1016/j.saa.2017.09.067.
- [142] J. W. Hofstraat and M. J. Latuhihin, "Correction of Fluorescence Spectra", *Applied Spectroscopy* 48.4 (1994), pp. 436–447, DOI: 10.1366/000370294775269027.
- [143] N. K. Schwalb, T. Michalak, and F. Temps, "Ultrashort Fluorescence Lifetimes of Hydrogen-Bonded Base Pairs of Guanosine and Cytidine in Solution", *The Journal of Physical Chemistry B* 113.51 (2009), pp. 16365–16376, DOI: 10.1021/jp904883n.

- [144] K. Ekvall, P. van der Meulen, C. Dhollande, L.-E. Berg, S. Pommeret, R. Naskrecki, and J.-C. Mialocq, "Cross Phase Modulation Artifact in Liquid Phase Transient Absorption Spectroscopy", *Journal of Applied Physics* 87.5 (2000), pp. 2340–2352, DOI: 10.1063/1.372185.
- [145] M. Lorenc, M. Ziolk, R. Naskrecki, J. Karolczak, J. Kubicki, and A. Maciejewski, "Artifacts in Femtosecond Transient Absorption Spectroscopy", *Applied Physics B: Lasers and Optics* 74.1 (2002), pp. 19–27, DOI: 10.1007/s003400100750.
- [146] M. V. Lebedev, O. V. Misochko, T. Dekorsy, and N. Georgiev, "On the Nature of "Coherent Artifact"", *Journal of Experimental and Theoretical Physics* 100.2 (2005), pp. 272–282, DOI: 10.1134/1.1884668.
- [147] B. Dietzek, T. Pascher, V. Sundström, and A. Yartsev, "Appearance of Coherent Artifact Signals in Femtosecond Transient Absorption Spectroscopy in Dependence on Detector Design", *Laser Physics Letters* 4.1 (2007), pp. 38–43, DOI: 10.1002/lapl.200610070.
- [148] J. K. Wilmhurst and H. J. Bernstein, "The Infrared and Raman Spectra of Toluene, Toluene- α -D₃, m-Xylene, and m-Xylene- $\alpha\alpha'$ -D₆", *Canadian Journal of Chemistry* 35 (1957), p. 911.
- [149] T. H. S. Bican, H. W. Schrötter, and V. M. Grošev, "The Raman Spectrum of Toluene Vapour", *Journal of Raman Spectroscopy* 26.8-9 (1995), pp. 787–790, DOI: 10.1002/jrs.1250260828.
- [150] M. Cho, M. Du, N. F. Scherer, G. R. Fleming, and S. Mukamel, "Off-Resonant Transient Birefringence in Liquids", *J. Chem. Phys.* 99.4 (1993), p. 19.
- [151] P. Fita, E. Luzina, T. Dziembowska, C. Radzewicz, and A. Grabowska, "Chemistry, Photophysics, and Ultrafast Kinetics of Two Structurally Related Schiff Bases Containing the Naphthalene or Quinoline Ring", *The Journal of Chemical Physics* 125.18 (2006), p. 184508, DOI: 10.1063/1.2371058.
- [152] J. V. Lockard, A. A. Rachford, G. Smolentsev, A. B. Stickrath, X. Wang, X. Zhang, K. Atenkoff, G. Jennings, A. Soldatov, A. L. Rheingold, F. N. Castellano, and L. X. Chen, "Triplet Excited State Distortions in a Pyrazolate Bridged Platinum Dimer Measured by X-Ray Transient Absorption Spectroscopy", *The Journal of Physical Chemistry A* 114.48 (2010), pp. 12780–12787, DOI: 10.1021/jp1088299.
- [153] C. Slavov, H. Hartmann, and J. Wachtveitl, "Implementation and Evaluation of Data Analysis Strategies for Time-Resolved Optical Spectroscopy", *Analytical Chemistry* 87.4 (2015), pp. 2328–2336, DOI: 10.1021/ac504348h.
- [154] M. P. Grubb, A. J. Orr-Ewing, and M. N. R. Ashfold, "KOALA: A Program for the Processing and Decomposition of Transient Spectra", *Review of Scientific Instruments* 85.6 (2014), p. 064104, DOI: 10.1063/1.4884516.
- [155] H. Zipse, *Vibrational Frequencies - Technical Considerations (accessed 21.2.2019)*, <https://www.cup.uni-muenchen.de/ch/compchem/vib/vib1.html>, 2004.

Bibliography

- [156] S. Ito, T. Nagami, and M. Nakano, "Density Analysis of Intra- and Intermolecular Vibronic Couplings toward Bath Engineering for Singlet Fission", *The Journal of Physical Chemistry Letters* 6.24 (2015), pp. 4972–4977, DOI: 10.1021/acs.jpcclett.5b02249.
- [157] D. Polli, P. Altoè, O. Weingart, K. M. Spillane, C. Manzoni, D. Brida, G. Tomasello, G. Orlandi, P. Kukura, R. A. Mathies, M. Garavelli, and G. Cerullo, "Conical Intersection Dynamics of the Primary Photoisomerization Event in Vision", *Nature* 467.7314 (2010), pp. 440–443, DOI: 10.1038/nature09346.
- [158] I. Rivalta, A. Nenov, O. Weingart, G. Cerullo, M. Garavelli, and S. Mukamel, "Modelling Time-Resolved Two-Dimensional Electronic Spectroscopy of the Primary Photoisomerization Event in Rhodopsin", *The Journal of Physical Chemistry B* 118.28 (2014), pp. 8396–8405, DOI: 10.1021/jp502538m.
- [159] C. Schnedermann, M. Liebel, and P. Kukura, "Mode-Specificity of Vibrationally Coherent Internal Conversion in Rhodopsin during the Primary Visual Event", *Journal of the American Chemical Society* 137.8 (2015), pp. 2886–2891, DOI: 10.1021/ja508941k.
- [160] G. D. Scholes, "Quantum-Coherent Electronic Energy Transfer: Did Nature Think of It First?", *The Journal of Physical Chemistry Letters* 1.1 (2010), pp. 2–8, DOI: 10.1021/jz900062f.
- [161] D. B. Turner, R. Dinshaw, K.-K. Lee, M. S. Belsley, K. E. Wilk, P. M. G. Curmi, and G. D. Scholes, "Quantitative Investigations of Quantum Coherence for a Light-Harvesting Protein at Conditions Simulating Photosynthesis", *Physical Chemistry Chemical Physics* 14.14 (2012), p. 4857, DOI: 10.1039/c2cp23670b.
- [162] D. Abramavicius and L. Valkunas, "Role of Coherent Vibrations in Energy Transfer and Conversion in Photosynthetic Pigment–Protein Complexes", *Photosynthesis Research* 127.1 (2016), pp. 33–47, DOI: 10.1007/s11120-015-0080-6.
- [163] P. Ball, "Is Photosynthesis Quantum-Ish?", *Physics World* (2018).
- [164] H. L. Fragnito, J.-Y. Bigot, P. Becker, and C. Shank, "Evolution of the Vibronic Absorption Spectrum in a Molecule Following Impulsive Excitation with a 6 fs Optical Pulse", *Chemical Physics Letters* 160.2 (1989), p. 4.
- [165] P. C. Becker, H. L. Fragnito, J. Y. Bigot, C. H. Brito Cruz, R. L. Fork, and C. V. Shank, "Femtosecond Photon Echoes from Molecules in Solution", *Physical Review Letters* 63.5 (1989), pp. 505–507, DOI: 10.1103/PhysRevLett.63.505.
- [166] M. Liebel, C. Schnedermann, T. Wende, and P. Kukura, "Principles and Applications of Broadband Impulsive Vibrational Spectroscopy", *The Journal of Physical Chemistry A* 119.36 (2015), pp. 9506–9517, DOI: 10.1021/acs.jpca.5b05948.
- [167] T. Brixner, I. V. Stiopkin, and G. R. Fleming, "Tunable Two-Dimensional Femtosecond Spectroscopy", *Optics Letters* 29.8 (2004), p. 884, DOI: 10.1364/OL.29.000884.

- [168] M. Son and G. S. Schlau-Cohen, "Ultrabroadband 2D Electronic Spectroscopy as a Tool for Direct Visualization of Pathways of Energy Flow", *Physical Chemistry of Semiconductor Materials and Interfaces XVI*, ed. by H. A. Bronstein and F. Deschler, San Diego, United States: SPIE, 2017, p. 42, DOI: 10.1117/12.2273417.
- [169] M. H. Stockett, J. Houmøller, and S. Brøndsted Nielsen, "Nile Blue Shows Its True Colors in Gas-Phase Absorption and Luminescence Ion Spectroscopy", *The Journal of Chemical Physics* 145.10 (2016), p. 104303, DOI: 10.1063/1.4962364.
- [170] M. Marazzi, H. Gattuso, and A. Monari, "Nile Blue and Nile Red Optical Properties Predicted by TD-DFT and CASPT2 Methods: Static and Dynamic Solvent Effects", *Theoretical Chemistry Accounts* 135.3 (2016), DOI: 10.1007/s00214-016-1814-z.
- [171] Q.-y. Chen, D.-h. Li, H.-h. Yang, Q.-z. Zhu, J.-g. Xu, and Y. Zhao, "Interaction of a Novel Red-Region Fluorescent Probe, Nile Blue, with DNA and Its Application to Nucleic Acids Assay", *The Analyst* 124.6 (1999), pp. 901–906, DOI: 10.1039/a901174i.
- [172] J. Madsen, I. Canton, N. J. Warren, E. Themistou, A. Blanazs, B. Ustbas, X. Tian, R. Pearson, G. Battaglia, A. L. Lewis, and S. P. Armes, "Nile Blue-Based Nanosized pH Sensors for Simultaneous Far-Red and Near-Infrared Live Bioimaging", *Journal of the American Chemical Society* 135.39 (2013), pp. 14863–14870, DOI: 10.1021/ja407380t.
- [173] B. Wang, J. Fan, X. Wang, H. Zhu, J. Wang, H. Mu, and X. Peng, "A Nile Blue Based Infrared Fluorescent Probe: Imaging Tumors That over-Express Cyclooxygenase-2", *Chemical Communications* 51.4 (2015), pp. 792–795, DOI: 10.1039/C4CC08915D.
- [174] A. Ahmad, K. Kern, and K. Balasubramanian, "Selective Enhancement of Carbon Nanotube Photoluminescence by Resonant Energy Transfer", *ChemPhysChem* 10.6 (2009), pp. 905–909, DOI: 10.1002/cphc.200800796.
- [175] J. Vogelsang, C. Steinhauer, C. Forthmann, I. H. Stein, B. Person-Skegro, T. Cordes, and P. Tinnefeld, "Make Them Blink: Probes for Super-Resolution Microscopy", *ChemPhysChem* 11.12 (2010), pp. 2475–2490, DOI: 10.1002/cphc.201000189.
- [176] y. Rhee, M. R. Valentine, and J. Termini, "Oxidative Base Damage in RNA Detected by Reverse Transcriptase", *Nucleic Acids Research* 23.16 (1995), pp. 3275–3282, DOI: 10.1093/nar/23.16.3275.
- [177] K. Hirakawa, K. Ota, J. Hirayama, S. Oikawa, and S. Kawanishi, "Nile Blue Can Photosensitize DNA Damage through Electron Transfer", *Chemical Research in Toxicology* 27.4 (2014), pp. 649–655, DOI: 10.1021/tx400475c.
- [178] H. Gattuso, V. Besancenot, S. Grandemange, M. Marazzi, and A. Monari, "From Non-Covalent Binding to Irreversible DNA Lesions: Nile Blue and Nile Red as Photosensitizing Agents", *Scientific Reports* 6.1 (2016), DOI: 10.1038/srep28480.
- [179] J. Hauer, T. Buckup, and M. Motzkus, "Enhancement of Molecular Modes by Electronically Resonant Multipulse Excitation: Further Progress towards Mode Selective Chemistry", *The Journal of Chemical Physics* 125.6 (2006), p. 061101, DOI: 10.1063/1.2243273.

Bibliography

- [180] M. Dantus, "COHERENT NONLINEAR SPECTROSCOPY : From Femtosecond Dynamics to Control", *Annual Review of Physical Chemistry* 52.1 (2001), pp. 639–679, DOI: 10.1146/annurev.physchem.52.1.639.
- [181] K. Ohmori, "Wave-Packet and Coherent Control Dynamics", *Annual Review of Physical Chemistry* 60.1 (2009), pp. 487–511, DOI: 10.1146/annurev.physchem.59.032607.093818.
- [182] Y. Silberberg, "Quantum Coherent Control for Nonlinear Spectroscopy and Microscopy", *Annual Review of Physical Chemistry* 60.1 (2009), pp. 277–292, DOI: 10.1146/annurev.physchem.040808.090427.
- [183] G. Cerullo and C. Vozzi, "Coherent Control of Chemical Reactions on the Attosecond Time Scale", *Physics* 5 (2012), DOI: 10.1103/Physics.5.138.
- [184] J. C. Dean and G. D. Scholes, "Coherence Spectroscopy in the Condensed Phase: Insights into Molecular Structure, Environment, and Interactions", *Accounts of Chemical Research* 50.11 (2017), pp. 2746–2755, DOI: 10.1021/acs.accounts.7b00369.
- [185] G. D. Scholes, G. R. Fleming, L. X. Chen, A. Aspuru-Guzik, A. Buchleitner, D. F. Coker, G. S. Engel, R. van Grondelle, A. Ishizaki, D. M. Jonas, J. S. Lundeen, J. K. McCusker, S. Mukamel, J. P. Ogilvie, A. Olaya-Castro, M. A. Ratner, F. C. Spano, K. B. Whaley, and X. Zhu, "Using Coherence to Enhance Function in Chemical and Biophysical Systems", *Nature* 543.7647 (2017), pp. 647–656, DOI: 10.1038/nature21425.
- [186] O. Kühn, T. Renger, and V. May, "Theory of Exciton-Vibrational Dynamics in Molecular Dimers", *Chemical Physics* 204.1 (1996), pp. 99–114, DOI: 10.1016/0301-0104(95)00448-3.
- [187] D. Egorova, "Oscillations in Two-Dimensional Photon-Echo Signals of Excitonic and Vibronic Systems: Stick-Spectrum Analysis and Its Computational Verification", *The Journal of Chemical Physics* 140.3 (2014), p. 034314, DOI: 10.1063/1.4861634.
- [188] S. Murov, *Properties of Organic Solvents*, 2010.
- [189] N. Christensson, F. Milota, A. Nemeth, I. Pugliesi, E. Riedle, J. Sperling, T. Pullerits, H. F. Kauffmann, and J. Hauer, "Electronic Double-Quantum Coherences and Their Impact on Ultrafast Spectroscopy: The Example of β -Carotene", *The Journal of Physical Chemistry Letters* 1.23 (2010), pp. 3366–3370, DOI: 10.1021/jz101409r.
- [190] A. W. Albrecht, J. D. Hybl, S. M. Gallagher Faeder, and D. M. Jonas, "Experimental Distinction between Phase Shifts and Time Delays: Implications for Femtosecond Spectroscopy and Coherent Control of Chemical Reactions", *The Journal of Chemical Physics* 111.24 (1999), pp. 10934–10956, DOI: 10.1063/1.480457.

CURRICULUM VITAE

Lars-Hendrik Mewes
Avenue Montgibert 18,
CH-1005 Lausanne

Phone : +41 78 961 11 84
+49 178 6985 201
Website : <https://lsu.epfl.ch/>
<https://people.epfl.ch/lars.mewes>
E-mail : lars.h.mewes@gmail.com

Education

2014 – 2019	PhD in Physics École polytechnique fédérale de Lausanne, Switzerland
2014	Masterthesis Friedrich-Alexander Universität Erlangen-Nürnberg, Germany <i>Towards Ultrafast Time Resolved Photoelectron Spectroscopy of Solutes Using Liquid Microjets</i> Thesis supervisor : Prof. Dirk M. Guldi (FAU) Co-supervisor : Prof. Majed Chergui (EPFL)
2009 – 2014	BSc & MSc in Molecular Nano Science FAU ERASMUS semester at EPFL

Publications

Papers in international journal

M. Oppermann, N. S. Nagornova, A. Oriana, E. Baldini, L. Mewes, B. Bauer, T. Palmieri, T. Rossi, F. Van Mourik, M. Chergui. The LOUVRE Laboratory: *State-of-the-Art Ultrafast Ultraviolet Spectroscopies for Molecular and Materials Science*, *Chimia*, vol. 71(5), p. 288 - 294, 2017. <http://dx.doi.org/10.2533/chimia.2017.288>

F. G. Santomauro, J. Grilj, L. Mewes, G. Nedelcu, S. Yakunin, T. Rossi, G. Capano, A. Al Haddad, J. Budarz, D. Kinschel, D.S. Ferreira, G. Rossi, M. Gutierrez Tovar, D. Grolimund, V. Samson, M. Nachtegaal, G. Smolentsev, M.V. Kovalenko, M. Chergui, *Localized holes and delocalized electrons in photoexcited inorganic perovskites: Watching each atomic actor by picosecond X-ray absorption spectroscopy*, *Structural Dynamics*, vol. 4(4), p. 044002, 2017. <http://dx.doi.org/10.1063/1.4971999>

C. Arrell, J. Ojeda, L. Mewes, J. Grilj, F. Frassetto, L. Poletto, F. Van Mourik, M. Chergui, *Laser-Assisted Photoelectric Effect from Liquids*, *Physical Review Letters*, vol. 117(14), p. 143001, 2016. <http://dx.doi.org/10.1103/PhysRevLett.117.143001>

J. Ojeda, C. A. Arrell, J. Grilj, F. Frassetto, L. Mewes, H. Zhang, F. Van Mourik, L. Poletto, M. Chergui, *Harmonium: A pulse preserving source of monochromatic extreme ultraviolet (30-110 eV) radiation for ultrafast photoelectron spectroscopy of liquids*, *Structural Dynamics*, vol. 3(2), p. 023602, 2016. <https://dx.doi.org/10.1063/1.4933008>

C. Schubert, M. Wielopolski, L.-H. Mewes, G. de Miguel Rojas, C. van der Pol, K.C. Moss, M.R. Bryce, J.E. Moser, T. Clark, D.M. Guldi, *Precise Control of Intramolecular Charge-Transport:*

The Interplay of Distance and Conformational Effects, Chemistry - A European Journal, vol. 19, p. 7575 - 7586, 2013. <https://doi.org/10.1002/chem.201204055>

Seminars (selection)

Singlet fission in pentacene + 2DES of rhodamine 800, LACUS: Madison-Lausanne workshop, July 13, 2018, EPFL.

2D visible spectroscopy, MUMOS group meeting, May 23, 2018, TU Munich.

Population and coherence in di-Platinum complexes, LSU colloquium, July 4, 2017, EPFL.

Posters (selection)

2D and transient spectroscopy @ LSU, International Symposium on Ultrafast Science, November 28-30, 2018, Lausanne, Switzerland.

Understanding vibronic coherences using broadband transient absorption anisotropy, Quantum Dynamics and Spectroscopy of Functional Molecular Materials and Biological Photosystems, May 21-26, 2017, Les Houches, France.

Coherent 2D spectroscopy of pentacene thin films, The 8th International Conference on Coherent Multidimensional Spectroscopy, June 29 - July 1, 2016, Groningen, Netherlands.

A broadband visible 2D Fourier transform setup to investigate the photo physics of photovoltaic materials, The 2nd International Symposium on Singlet Fission and Photon Fusion, April 16-19, 2018, Gothenburg, Sweden.

Teaching

Teaching assistant for courses

- Ultrafast Phenomena

Course for EPFL doctoral students in physics and photonics. The course covers fundamental concepts and recent developments in the field of ultrafast spectroscopy and introduces the basic theory to understand ultrafast (10^{-16} – 10^{-9} s) phenomena in chemistry, biology and condensed matter physics. Exercises involve the mathematical description of laser pulses and their interaction with matter à la Mukamel.

- Atoms and radiation
- Physique générale II

Supervisor for Master theses

- *Stability improvement of white light generation for ultrafast visible spectroscopy*, Master thesis, Stéphane Carlessi (Chemistry and Chemical Engineering), 2018.

Supervisor for semester projects

- *Transient absorption and anisotropy of the Metal-Metal-to-Ligand-Charge-Transfer transition in $[Pt(ppy)(\mu\text{-}^tBu_2pz)]_2$* , Stéphane Carlessi (Chemistry and Chem. Eng.), 2017.

Awards and distinctions

- Honours of the “Gesellschaft Deutscher Chemiker (GDCh)” in chemistry (2008). *Award for the best Abitur in Chemistry.*

